Photonic Quantum Information Processing in the Frequency Domain

Von der Fakultät für Mathematik und Physik

der Gottfried Wilhelm Leibniz Universität Hannover zur Erlangung des Grades

Doktorin der Naturwissenschaften

Dr. rer. nat.

genehmigte Dissertation von

Anahita Khodadad Kashi M.Sc.

2025

Referent	Prof. Dr. Michael Kues
Koreferenten	Prof. Dr. Tanja Mehlstäubler
	Prof. Dr. Lucia Caspani
	Prof. Dr. Antonio Calà Lesina
Tag der Promotion	18.02.2025

Abstract

The realization of the quantum internet, as the future generation of communications technology, requires overcoming the existing scalability hurdles in distribution and processing of quantum information in large-scale quantum networks. In this thesis, experimental solutions based on the photonic frequency degree-of-freedom are revealed for the scalable implementation of quantum information processing. To this end, the compatibility of the photonic frequency domain with off-the-shelf telecommunication components is leveraged and the frequency's intrinsic properties such as stability and multi-mode nature are deployed. The second-order degree of coherence of photons from parametric processes is for the first-time measured as function of frequency correlations, using a novel, convenient and time-efficient scheme. Moreover, a versatile and scalable approach is deployed for the first-time experimental implementation of the spectral Hong-Ou-Mandel effect between independent single-photons, as a widely deployed quantum phenomenon in quantum information processing applications. Importantly, a previously unexplored interferometric effect is revealed experimentally and verified theoretically, giving prominence to the contributive role of multiphoton components in heralded states to the visibility of the Hong-Ou-Mandel effect, with potential applications for addressing the security loopholes in remote secret key sharing schemes. Additionally, using a novel scalable approach, the first-time experimental implementation of the frequency-bin-encoded entanglement-based quantum key distribution protocol and a reconfigurable transmission of frequency-bin entangled states is demonstrated, allowing for a dynamic network architecture, a growing network size with a preserved security, and a linear increase in hardware overhead in contrast to quadratic increase observed in previous implementation schemes.

Zussamenfassung

Die Verwirklichung des Quanteninternets als künftige Generation der Kommunikationstechnologie erfordert die Überwindung der bestehenden Skalierungshürden bei der Verteilung und Verarbeitung von Quanteninformationen in groß angelegten Quantennetzwerken. In dieser Dissertation werden neuartige photonische experimentelle Lösungen basierend auf dem Frequenzfreiheitsgrad für die skalierbare Implementierung der Quanteninformationsverarbeitung vorgestellt. Zu diesem Zweck wird die Kompatibilität des photonischen Frequenzbereichs mit handelsüblichen Telekommunikationskomponenten genutzt, und die intrinsischen Eigenschaften der Frequenz, wie Stabilität und multimodale Natur, werden eingesetzt.

Der Kohärenzgrad zweiter Ordnung von Photonen aus parametrischen Prozessen wird erstmals als Funktion der Frequenzkorrelationen mit einem neuartigen, praktischen und zeiteffizienten Verfahren gemessen. Darüber hinaus wird ein vielseitiger und skalierbarer Ansatz für die erstmalige experimentelle Implementierung des spektralen Hong-Ou-Mandel-Effekts zwischen unabhängigen Einzelphotonen eingesetzt, ein weit verbreitetes quantenphysikalisches Phänomen in Anwendungen der Quanteninformationsverarbeitung. Wichtig ist, dass ein zuvor unerforschter interferometrischer Effekt experimentell nachgewiesen und theoretisch verifiziert wird, wobei die beitragende Rolle der Mehrphotonenkomponenten in angekündigten Zuständen für die Sichtbarkeit hervorgehoben wird, mit potenziellen Anwendungen zur Schließung von Sicherheitslücken in Verfahren zum geheimen Schlüsselaustausch über große Entfernungen. Zudem wird unter Einsatz eines neuartigen skalierbaren Ansatzes die erstmalige experimentelle Implementierung eines auf Frequenz-Bin-kodierten, verschränkungsbasierten Quanten-Schlüsselaustauschprotokolls sowie die rekonfigurierbare Übertragung von Frequenz-Bin-verschränkten Zuständen demonstriert, was eine dynamische Netzwerkarchitektur, ein wachsendes Netzwerk mit gewahrter Sicherheit und einen linearen Anstieg des Hardwareaufwands im Gegensatz zu dem in früheren Implementierungsschemata beobachteten quadratischen Anstieg ermöglicht.

Abbreviations

SPDC	Spontaneous Parametric Down-conversion
SFWM	Spontaneous Four-wave Mixing
PPLN	Periodically-poled Lithium Niobate
FTM	Frequency-to-time Mapping
QIP	Quantum Information Processing
JSI	Joint Spectral Intensity
CAR	Coincidence to Accidental Ratio
HOM	Hong-Ou-Mandel
FWHM	Full-width at Half-maximum
SNSPD	Superconducting Nanowire Single-photon Detector
TDC	Time-to-digital Convertor
DCF	Dispersion Compensating Fiber
GDD	Group Delay Dispersion
HBT	Hanbury Brown and Twiss
QKD	Quantum Key Distribution
EBQKD	Entanglement-based Quantum Key Distribution
QBER	Quantum Bit Error Ratio
BB84	Bennett Brassard 1984
BBM92	Bennett Brassard Mermin 1992

Table of Contents

Table of Figures

List of Tables

1. Introduction

The following introduction outlines the background, objectives, and the significance of the current study, setting the stage for the research questions and methodology presented in this thesis.

1.1. The Quantum Internet

The quantum internet is the next generation of global communication infrastructure that aims at harnessing the principles of quantum mechanics, such as superposition and entanglement, to enable the storage, transmission, and processing of quantum information, enabling ultra-high security, precision, and unprecedented computational capabilities [1]. The quantum internet is envisioned to outperform the classical internet by revolutionizing a wide range of applications, such as providing unhackable security via quantum key distribution (QKD) protocols [2], facilitating ultra-precise measurements through quantum-enhanced sensing and metrology [3], and enabling distributed quantum computing [4] for solving complex optimization problems such as in finance [5] and quantum machine learning [6]. The future technology of the quantum internet is envisaged to be based on large-scale implementation of photonic quantum networks.

1.2. Scalability Hurdles of Quantum Networks

The lack of scalable implementation schemes has impeded the realization of the quantum internet as a global quantum network. A scalable implementation scheme allows for an efficient expansion of the number of concurrent quantum operations across multiple users spanning distant locations, and at the same time provides a reliable and secure performance [7–9]. Such an approach ensures that physical resources scale at a linear rather than exponential rate, and facilitates high data-throughput. Additionally, it is crucial to ensure that with the growing size of the network, noise remains at low rates, and the processing and transmission of quantum information maintains secure and without significant loss of fidelity [10].

In this regard, the scalable implementation of quantum information processing (QIP) tools is essential to the ultimate scalability of quantum networks. Importantly, the non-classical Hong-Ou-Mandel (HOM) effect [11] lies at the heart of quantum networks which involves

destructive quantum interference at a balanced beam splitter of two-photon reflected and two-photon transmitted amplitudes. The HOM effect is widely deployed in quantum computation [12], quantum-enhanced metrology [3,13], quantum random walks [14,15], boson sampling [16], linear optical quantum gates [17–19], quantum super dense coding [20], and non-classical communications [21–24].

An additional resource in quantum networks is entanglement – the irreproducible non-classical and non-local correlations among, say two photons [25–27] – based on which a myriad of applications are functional. For instance, the entanglement-based quantum key distribution (EBQKD), as a highly secure method for exchanging cryptographic keys [28–30], and required for the future development of quantum repeaters [31,32].

To date, entanglement-based quantum networking schemes and the HOM effect have been mainly implemented in the spatial domain [33–36], which in a large-scale implementation involves a control over several different static arrangements of waveguides and conventional spatial-domain beam splitters, hence an exponential increase in the hardware overhead. Noteworthy, different photonic information encoding schemes using polarization [37–39], time-bin [40–42], and orbital-angular momentum [43–45] degrees-of-freedom often involve static, complex, and resource-intensive optimization and stabilization setups that are challenging to scale up. This highlights the significance of developing an information encoding scheme that could facilitate a dynamic network architecture, adaptable to the growing network demands without requiring massive infrastructure upgrade. Additionally, an information encoding scheme is requried to play an interfacing role among different photonic degrees-of-freedom and various physical platforms within the quantum network architecture.

1.3. Frequency-domain QIP to Enable Scalability

In this thesis, photonic frequency degree-of-freedom is considered for encoding and processing of information to address the scalability issues in quantum networks. This is realized by relying on the inherent properties of frequency domain such as its multimode nature which supports high-dimensional encoding of quantum information, hence an intrinsic robustness to noise [46] and an enhanced data throughput [47–49]. Additionally, compared to time-bin and polarization encoding, frequency is less vulnerable to environmental factors such as temperature fluctuations and mechanical vibrations which allows to preserve the coherence of quantum states in optical fibers over extended

geographical areas. Importantly, the compatibility of frequency with mature fiber-optic telecommunication components would facilitate its deployment in large-scale quantum networks [50–54]. The standard single-spatial-mode of operation of omnipresent telecommunication components preserves its phase stability, and the reconfigurability of devices with fine frequency resolution allows for a dynamic network architecture to realize an adaptive QIP platform. Importantly, parallel transmission of signals at different frequencies would be possible via available frequency de/multiplexing techniques, which allows for increased data-throughput in the network, supports multi-user operations, and enables full-bandwidth utilization of optical fibers. Moreover, the frequency conversion techniques could be exploited to convert quantum states between different quantum channels and nodes operating at different frequencies, which contributes to the scalability of quantum networks [55,56].

Noteworthy, an efficient and scalable implementation of frequency-encoded QIP underscores the significance of exploring a spectral characterization scheme for biphoton states [57,58], such as spontaneous parametric down-conversion (SPDC) [59] and spontaneous four-wave mixing (SFWM) [60], as two widely used photon pair source in quantum information processing applications.

1.4. Objectives of the Research

In this thesis, novel scalable approaches based on the photonic frequency-domain processing are demonstrated and deployed for the experimental proof-of-concept implementation of essential QIP applications, aiming at the future time realization of scalable, meaningful, and real-world quantum networks. In the following, the state-of-the-art of the research areas in this thesis is reviewed and an introduction to the novelties and contributions of this thesis is presented.

1.4.1. An Efficient Spectral Characterization Technique for Biphoton States

Characterization of spectral properties of biphoton states generated from nonlinear optical parametric processes, is a fundamental tool for designing, optimizing, and scaling of QIP systems. Via spectral characterization, the quality and coherence of quantum states can be assessed to ensure the compatibility with other quantum systems and in turn to facilitate a high-performance quantum network [61–64]. To date, characterization techniques have

been primarily based on successive and time-consuming frequency scans over the biphoton state spectrum [65–67]. However, spectral filtering of photon pairs yields inefficient detection rates, degrades the signal-to-noise ratio, and restricts the accessible spectral resolution. Low spectral resolution and frequency sampling rate, measurement instability, long integration time, and increased noise, are the main limitations of charcaterization techniques that are based on position-to-frequency mapping [68], Fourier spectroscopy [69,70], and stimulated SPDC or SFWM [71,72].

In this thesis, the first-time direct measurement of the second-order degree of coherence as function of frequency correlations is revealed which allows for a precise determination of the single frequency mode bandwidth of pulsed-driven biphoton states from parametric processes with an unrecedented spectral resolution. The presented approach is based on the well-established frequency-to-time mapping (FTM) technique [70,73–80], realizing a time-resolved replica of the spectrum.

1.4.2. Scalable Implementation of the HOM Effect in Frequency

The spectral implementation of the HOM effect can significantly contribute to the scalability of quantum networks. Previously, the frequency-domain HOM effect between a single-photon and a coherent state was realized using optical nonlinear parametric effects as a means for frequency mixing [81], which however required complex and bulky optical setups and suffered from degraded quantum interference as a result of higher order emissions. The frequency-domain HOM effect has been demonstrated between two photons created from a continuous-wave-excited SPDC process where an electro-optic phase modulator was utilized as a frequency mixer [82]. However, this implementation was not scalable to higher number of photons due to the photons' inherent spectral impurity.

In this thesis, the first-time experimental implementation of the frequency-domain bosonic and fermionic-like HOM effects between two independently generated single-photon states from pulsed-driven SPDC process is demonstrated. To this end, a novel and scalable experimental approach based on the employment of reconfigurable telecommunication components, such as electro-optic phase modulator and programmable filters, is demonstrated.

Additionally, the first-time frequency-domain HOM effect between a thermal field and a heralded state is experimentally demonstrated, revealing a contributive role to the HOM visibility from the multiphoton components intrinsic to the heralded states, which can have

potential applications to e.g., measurement-device-independent QKD protocols. In addition, the experimental observations regarding the contribution from the multiphoton components to the HOM visibility are verified theoretically by deriving a novel formulation showing the compound dependency of the HOM visibility on the average photon number of the interacting fields.

1.4.3. Scalable Implementation of EBQKD in Frequency

Compared to prepare-and-measure schemes such as the BB84 protocol [83], the EBQKD protocols offer an enhanced security against coherent attacks and a greater tolerance to channel loss [28,84,85]. However, issues arising from distance limitations, degraded security in face of advanced attacks, resource overhead, and growing hardware complexity and cost emerging from static implementations, hinder a scalable realization of EBQKD networks [86].

The frequency degree-of-freedom paired with time-bin encoding has been exploited in some QKD protocols, such as the prepare-and-measure schemes, measurement-device-independent QKD, twin-field QKD, and for the development of quantum network architectures [87–95]. In these implementations, the frequency degree was deployed as part of a hybrid encoding scheme requiring non-scalable bulky interferometric setups with passive or active phase stabilization requirements.

In this thesis, the first-time experimental implementation of the frequency-bin-encoded EBQKD, namely the BBM92 protocol [84], is presented. Additionally, entanglement distribution over long fiber links is demonstrated using a flexible implementation scheme. Importantly, by utilizing the frequency-bin encoding approach, a novel scalable frequency-bin-basis analyzer module is developed that considerably reduces system complexity and hardware overhead, and at the same time allows for simultaneous multi-user EBQKD operations in a dynamic quantum network architecture with the capability to adapt to the required amount of key exchange rate, remarkably, at a maintained security level.

1.5. Structure of the Thesis

This thesis is organized in seven chapters and follows a hierarchical structure starting from the theoretical backgrounds and preliminaries to the main experimental implementations, summary, conclusion, and the future outlook.

Chapter two is concerned with the fundamentals and theoretical backgrounds required for a comprehensive understanding of the experimental implementations in the chapters that follow. Theoretical description of the SPDC process and the HOM effect, the significance of spectral purity to obtaining high interferometric visibility, photon statistics of different states of light, second-order (auto)correlation function, the Hanbury Brown & Twiss (HBT) interferometry, theoretical description of electro-optic phase modulation, and the spectral broadening induced by chromatic dispersion, are among the topics covered in this chapter. Chapter three presents the novel scalable experimental approach developed and implemented for the spectral characterization of biphoton states from parametric down conversion process. Chapter four contains the first-time scalable experimental implementation of the HOM effect in the frequency domain between two independent single-photon states. In chapter five, the first-time spectral implementation of the HOM effect between a heralded state and a thermal field is presented. In chapter six, the first-time experimental implementation of the frequency-bin-encoded EBQKD between two users is demonstrated. Chapter seven contains a summary and conclusive remarks on the key contributions of this thesis to addressing the scalability challenges of the state-of-the-art quantum networks. Additionally, an outlook and potential direction for the future research based on the results of this thesis is provided.

2. Preliminaries and the Theoretical Fundamentals

In this chapter, the theoretical fundamentals supporting the research and novelties in this thesis are presented. The theory of quantization of radiation field is reviewed as the basis of the calculations in this thesis, providing a framework for understanding the quantum nature of light and the interaction between photons. Pulsed-driven SPDC process is reviewed as a source of highly time-energy correlated photon pairs in the experiments of this thesis. The important quality metrics exploited to assess the biphoton states from the SPDC process are covered such as the joint spectral intensity (JSI) and the coincidence to accidental ratio (CAR). Schmidt decomposition is explained as a mathematical tool to quantify the spectral purity of biphoton states from parametric processes. The HOM effect is described theoretically, and the photon statistics and density matrix representation of different states of light are reviewed, including a single-photon state, a heralded state from parametric process, and a thermal distribution of photons. The theory of optical coherence and the HBT interferometry as a means to quantify the second-order correlation function, are among the topics covered in this chapter. Moreover, an overview of the operational framework of electro-optic phase modulator is presented as the primary building block utilized in the experiments. The theory of second-order chromatic dispersion is additionally reviewed providing a basis for the FTM technique deployed in the experiments of this thesis.

2.1. Quantization of the Radiation Field

The quantization of the radiation field allows for the quantum mechanical treatment of the electromagnetic field. Consider a one-dimensional quantum mechanical harmonic oscillator that can excite an infinite number *n* of equally-spaced energy levels, denoted by $\mathrm{E_n}$ ($n = 0, 1, 2, ...$). The quantum of energy between consecutive energy levels is $\mathrm{E}_{n+1} - \mathrm{E}_n = \hbar\omega$, where ω is the angular frequency of oscillation and $\hbar$ is half the Planck constant. The Hamiltonian of the quantum harmonic oscillator is written [96]

$$\hat{\mathrm{H}} = \frac{\hat{\mathrm{p}}^2}{2\mathrm{m}} + \frac{1}{2}m\omega^2\hat{\mathrm{q}}^2 \tag{2.1}$$

where $\hat{p}$ and $\hat{q}$ are the position and momentum operators, respectively, for which the commutation relation $[\hat{q}, \hat{p}] = i\hbar$ holds, and m is the mass of the oscillator. In quantum mechanics, the following two dimensionless operators $\hat{a} = (2m\hbar\omega)^{-\frac{1}{2}}(m\omega\hat{q} + i\hat{p})$ and $\hat{a}^\dagger = (2m\hbar\omega)^{-\frac{1}{2}}(m\omega\hat{q} - i\hat{p})$ are defined as the destruction and creation operators, respectively, used to describe the transitions between different quantized energy states of the oscillator. It can be verified that the creation and destruction operators obey the following specific commutation relationship $[\hat{a}, \hat{a}^\dagger] = \hat{a}\hat{a}^\dagger - \hat{a}^\dagger\hat{a} = 1$. Although $\hat{a}$ and $\hat{a}^\dagger$ do not represent any physical measurable observable, they are used to model the photon emission and absorption processes. The creation operator applied to a vacuum state creates a single-photon state: $\hat{a}^\dagger|0\rangle = |1\rangle$, and the destruction operator applied to a single-photon state returns the vacuum state: $\hat{a}\,|1\rangle = |0\rangle$. The generalized equation formulating the successive transitions between different quantized energy levels are governed by the following relationships $\hat{a}^\dagger|n\rangle = \sqrt{n+1}\,|n+1\rangle$ and $\hat{a}|n\rangle = \sqrt{n}\,|n-1\rangle$, which are used in chapter five to derive the visibility equation of the HOM effect between a thermal field and a heralded state.

The Hamiltonian in Eq. 2.1 can be rewritten in terms of the creation and destruction operators, such that $\hat{H}|n\rangle = \hbar\omega\,(\hat{n} + 1/2)\,|n\rangle$, where $\hat{n} = \hat{a}^\dagger\hat{a}$ is the photon number-state operator, and $E_n = \hbar\omega\,(n + 1/2)$ is the energy eigen value corresponding to the eigen state $|n\rangle$. It is thus followed that the lowest permissible energy level for the harmonic oscillator is $E_0 = \hbar\omega/2$ corresponding to the vacuum state denoted by $|0\rangle$.

2.2. Pulsed-driven SPDC Process

In the experiments of this thesis, a pulsed-driven SPDC process has been used as the source of highly time-energy correlated photon-pair emission. In this process which takes place in a non-centrosymmetric material exhibiting second-order $\chi^{(2)}$ nonlinearity (such as Lithium Niobate), a pump photon of an angular frequency ω_p is down-converted into a pair of '*signal'* and '*idler*' photons with angular frequencies ω_{si} and ω_{id}, respectively (see **Figure. 1**). By convention, *signal* is considered as the higher energy photon and *idler* as the lower energy photon of the process [97]. The biphoton state from the SPDC process can be expressed in terms of independent two-mode squeezers m such that $|\Psi\rangle = \bigotimes_m \hat{S}^m_{si,id}(\xi_m)|0\rangle_{si}|0\rangle_{id}$, where $\hat{S}^m_{si,id}(\xi_m)$ is a squeezing operator defined as function of the

squeezing parameter ξ_m. The value of ξ_m depends on the pump power intensity, the crystal length, and the second-order nonlinearity of the crystal.

Photon pair generation in SPDC is governed by the conservation laws of energy ($\omega_p = \omega_{si} + \omega_{id}$) and momentum ($\beta_p = \beta_{si} + \beta_{id}$), where $\beta_i = \omega_i n_{eff}$ is the propagation constant and n_{eff} is the effective refractive index of the pump, signal, and idler photons within a waveguide. The conservation of energy specifies the frequency correlations between the signal and idler photons, whereas the conservation of momentum determines the bandwidth over which the photon pair generation takes place. To compensate for the phase mismatch $\Delta\beta(\omega_{si}, \omega_{id}) = \beta_p(\omega_{si} + \omega_{id}) - \beta_{si}(\omega_{si}) - \beta_{id}(\omega_{id})$ between the interacting photons, the periodic poling of lithium niobate (PPLN) waveguides is implemented [98].

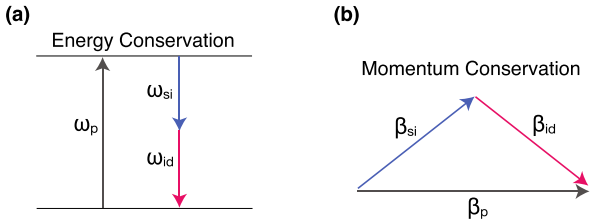

Figure. 1 Conservation of **(a)** energy ($\omega_p = \omega_{si} + \omega_{id}$) and **(b)** momentum ($\beta_p = \beta_{si} + \beta_{id}$) in SPDC process.

Depending on the polarization of the pump, signal, and idler photons, the SPDC process can be classified into three groups of type-0, type-I, and type-II. In type-0 SPDC, the polarization of the pump, signal and idler photons are identical and aligned with the crystal axis. This is achieved when all photons involved in the process experience identical effective refractive index. Due to better phase matching conditions, the type-0 SPDC offers higher generation efficiency compared to type-I & II. Throughout this thesis, two PPLN waveguides, manufactured by *Covesion* and *AdvR*, are utilized in the experiments, offering type-0 SPDC process with different phase matching bandwidths.

The signal-idler biphoton states generated from SPDC process can be written as

$$|\Psi\rangle_{si,id} = \int d\omega_{si} \int d\omega_{id}\, f(\omega_{si}, \omega_{id})\, \hat{a}^{\dagger}(\omega_{si})\, \hat{b}^{\dagger}(\omega_{id})|0,0\rangle_{si,id} \tag{2.2}$$

where $\hat{a}^{\dagger}$ and $\hat{b}^{\dagger}$ are the photon creation operators corresponding to the signal and idler frequency modes, respectively. In Eq. 2.2, $f(\omega_{si}, \omega_{id})$ is the joint spectral amplitude (JSA) function of the signal and idler photon pairs.

2.3. The JSI of Photons in SPDC Process

The joint spectral intensity (JSI) is defined as the two-dimensional joint spectral probability distribution of the signal and idler photons generated from the SPDC process [61]. The JSI provides useful information about the spectral properties of the signal-idler biphoton states. For instance, a pure biphoton state with a circular spectral profile corresponds to a product state, whereas highly entangled signal and idler photons, forming an inseparable biphoton state, exhibit a JSI characterized by a diagonal spectral profile shape. The JSI is the square modulus of the JSA, $|f(\omega_{si}, \omega_{id})|^2$, expressed as

$$|f(\omega_{si}, \omega_{id})|^2 \propto |\Phi(\omega_{si}, \omega_{id})|^2 |\alpha(\omega_{si} + \omega_{id})|^2 \tag{2.3}$$

where $\Phi(\omega_{si}, \omega_{id})$ is the phase matching function of the PPLN waveguide and $\alpha(\omega_{si} + \omega_{id})$ is the pump spectral profile function.

Consider a SPDC process with a degeneracy frequency of ω_0 in a PPLN waveguide with a Gaussian phase matching function and pumped by a pulsed laser source of a Gaussian spectral profile ($2\omega_0$ is the central frequency of the pump source). By redefining the signal and idler frequencies as $\upsilon_{si} = \omega_{si} - \omega_0$ and $\upsilon_{id} = \omega_{id} - \omega_0$, respectively, the JSI can be written as [61]

$$|f(\upsilon_{si}, \upsilon_{id})|^2 = M \exp\left(-\frac{2(\upsilon_{si}^2 + \upsilon_{id}^2)}{2\sigma^2} - \frac{4\,\upsilon_{si}\upsilon_{id}}{2\sigma^2}\right) \tag{2.4}$$

where M is the normalization coefficient, and σ is the spectral bandwidth of the pump source. Following Eq. 2.4, the JSI of a pulsed-driven SPDC process with a degeneracy angular frequency of ω_0 = 194 THz is simulated and shown in **Figure. 2a**. The anti-correlations observed between the signal and idler frequencies is an indication of an inseparable JSI. In experiments, it is often necessary to achieve quantum interference of high visibility for which a separable JSI is required. This can be realized by applying spectral filtration on the signal and idler spectrum, however, at the cost of reduced photon

flux. Applying a Gaussian spectral filter with an identical bandwidth σ_f to the signal and idler spectrum, transforms the JSI in Eq. 2.4 into the following expression

$$|f(\upsilon_{si}, \upsilon_{id})|^2 = A \exp\left[-2\left(\upsilon_{si}^2 + \upsilon_{id}^2\right)/2\sigma^2 - 2\upsilon_{si}\upsilon_{id}/2\sigma^2\right] \times \exp\left[-\upsilon_{si}^2/2\sigma_f^2\right] \times \exp\left[-\upsilon_{id}^2/2\sigma_f^2\right] \quad (2.5)$$

where A is the normalization coefficient. Spectral filtration of the JSI removes the frequency correlations and results in a factorizable JSI function as shown in **Figure. 2b**, which is implemented in the experiments of this thesis. In **Figure. 2c** & **2d**, the JSI corresponding to the *Covesion* and *AdvR* PPLN waveguides are displayed under 200 GHz spectral bandwidth of the excitation field. As illustrated, the *AdvR* PPLN features a wider phase matching bandwidth (~100 GHz) than the *Covesion* PPLN (~50 GHz).

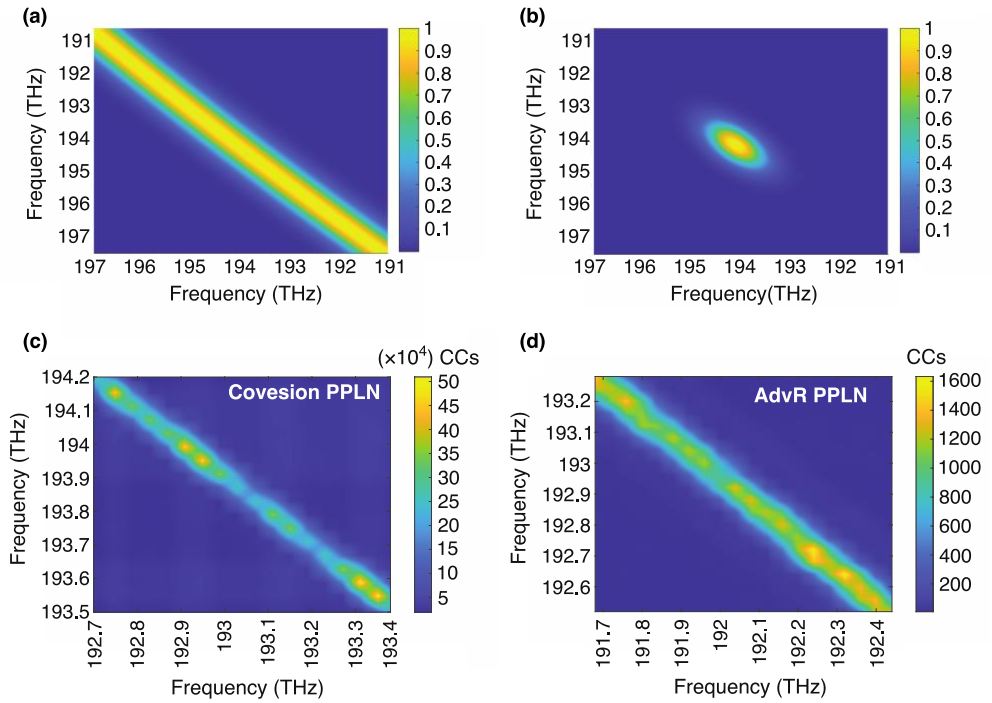

Figure. 2 The simulated joint spectral intensity (JSI) of the signal and idler photon pairs from pulsed-driven SPDC process with a degeneracy angular frequency of ω_0 = 194 THz **a)** without and **b)** with a Gaussian spectral filtration applied on the signal and idler spectrum. The experimentally reconstructed JSI of the **c)** *Covesion* and the **d)** *AdvR* PPLN waveguides obtained from frequency scanning of the signal and idler spectrum under three-hour integration time. (CCs: coincidence counts)

2.4. Schmidt Decomposition of the JSI

Schmidt decomposition is a mathematical tool that allows to quantify the multimode nature of biphoton states from a parametric process and in turn the degree of correlations between the down-converted signal and idler photons [99]. The Schmidt decomposition of any biphoton state composed of two subsystems A and B is written $|\Psi\rangle = \sum_m \sqrt{\lambda_m}\,|u_m\rangle_{\mathrm{A}} \otimes |v_m\rangle_{\mathrm{B}}$ where $\{|u_m\rangle\}_{\mathrm{A}}$ and $\{|v_m\rangle\}_{\mathrm{B}}$ are orthonormal basis states, termed as Schmidt eigenstates, and $\sqrt{\lambda_m}$ is the Schmidt coefficient which takes non-negative real numbers and satisfies the normalization condition $\sum_m \lambda_m = 1$. A useful parameter which can be extracted from this formulation is the Schmidt number defined as $\mathrm{K} = 1/\sum_m \lambda_m$ which quantifies the effective number of populated eigen modes.

For a pure bipartite state where only a single two-mode squeezer is involved, the individual signal and idler beams are a coherent superposition of photon number states characterized by thermal statistics. The Schmidt number for a pure biphoton state is $\mathrm{K} = 1$ and the JSI is a separable function expressed as the product of the squared modulus of the signal and idler amplitude functions. In contrast, for an entangled biphoton state composed of an infinite number of squeezers (infinite number of excited modes), the Schmidt number is characterized by $\mathrm{K} > 1$ and the JSI becomes unfactorizable. For an entangled state, the individual signal and idler beams are characterized by Poissonian photon statistics (a convolution over an infinite number of thermal distributions yields a Poissonian distribution). The degree of spectral purity for a biphoton state is defined as the inverse of the Schmidt number K and is related to the pump bandwidth σ and the spectral filter bandwidth σ_{f} through the following relationship [61,100]

$$\text{Purity} = \frac{1}{\mathrm{K}} = \sqrt{1 - 1/(1 + (\frac{\sigma}{\sigma_{\mathrm{f}}})^2)^2} \tag{2.6}$$

The variation of purity versus the ratio of the spectral filter bandwidth to the pump bandwidth is simulated in **Figure. 3.** In this thesis, the formulation in Eq. 2.6 combined with the experimental results from the HBT interferometer (see Sec. 2.10) are used to measure the single frequency mode bandwidth of the biphoton states from the SPDC process which is required to define the spectral configuration of the experiments.

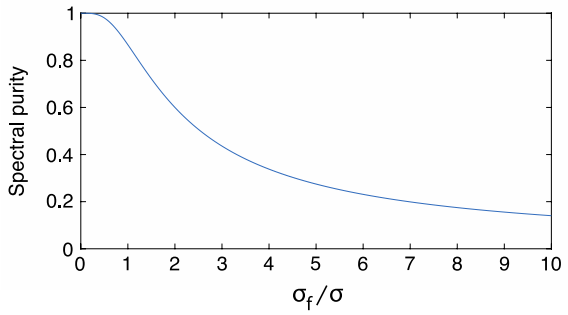

Figure. 3 Spectral purity of the biphoton state versus the ratio between the filter bandwidth σ_f, applied on the signal and idler spectrum, and the pump bandwidth σ.

2.5. The HOM Interference Effect

The Hong-Ou-Mandel (HOM) effect is a quantum phenomenon with no classical counterpart. This effect was first discovered in the seminal work by C. K. Hong, Z. Y. Ou, and L. Mandel, where the time intervals between two photons from a parametric down-conversion process were measured with sub-picosecond precision [11]. Here, the theoretical foundation of the HOM effect is presented, providing the reader with an insight into the experimental requirements for the implementation of this effect. The theoretical description is provided for the spatial domain which can be readily adapted to the frequency-analogue realization of the HOM effect, demonstrated in the experiments of the proceeding chapters.

Consider two photons that impinge on a 2-by-2 balanced beam splitter through its two input ports A and B (see **Figure 4**). The biphoton input state is written $|\Psi_{\text{in}}\rangle_{\text{AB}} = \hat{a}_j^\dagger \hat{b}_k^\dagger |0,0\rangle_{\text{AB}} = |1,1\rangle_{\text{AB}}$ where $\hat{a}_j^\dagger$ and $\hat{b}_k^\dagger$ are the bosonic creation operators acting on the vacuum state $|0,0\rangle_{\text{AB}}$ at the input ports of the beam splitter. The indices *j* and *k* identify any degree-of-freedom in which the interacting photons may be distinguishable, such as temporal, polarization, spectral or transverse spatial modes. Under loss-less conditions, the evolution of the input state upon mixing on the beam splitter is modelled by a unitary operator $\hat{\text{U}}_{\text{BS}}$ whose eigen values are taken from the reflection η and transmission $1-\eta$ coefficients of the beam splitter such that [101]

$$\hat{a}_j^\dagger \xrightarrow{\hat{\text{U}}_{\text{BS}}} \sqrt{1-\eta}\,\hat{a}_j^\dagger + \sqrt{\eta}\,\hat{b}_j^\dagger \qquad (2.7)$$

$$\hat{b}_k^\dagger \xrightarrow{\hat{\text{U}}_{\text{BS}}} \sqrt{\eta}\,\hat{a}_k^\dagger - \sqrt{1-\eta}\,\hat{b}_k^\dagger$$

The state after mixing on the beam splitter is written

$$|\Psi_{\text{out}}\rangle_{\text{AB}} = \hat{\text{U}}_{\text{BS}}\,|\Psi_{\text{in}}\rangle_{\text{AB}} \tag{2.8}$$
$$= \hat{\text{U}}_{\text{BS}}\left(\hat{a}_j^{\dagger}\hat{b}_k^{\dagger}|0,0\rangle_{\text{AB}}\right)$$
$$= (\sqrt{1-\eta}\,\hat{a}_{\text{j}}^{\dagger} + \sqrt{\eta}\,\hat{\text{b}}_{\text{j}}^{\dagger})(\sqrt{\eta}\,\hat{a}_{\text{k}}^{\dagger} - \sqrt{1-\eta}\,\hat{\text{b}}_{\text{k}}^{\dagger})|0,0\rangle_{\text{AB}}$$

For a balanced beam splitter where $\eta = 1/2$, the output state thus reads

$$|\Psi_{\text{out}}\rangle_{\text{AB}} = \frac{1}{2}\left(\hat{a}_j^{\dagger}\hat{a}_k^{\dagger} + \hat{a}_k^{\dagger}\,\hat{b}_j^{\dagger} - \hat{a}_j^{\dagger}\,\hat{b}_k^{\dagger} - \hat{b}_j^{\dagger}\,\hat{b}_k^{\dagger}\right)|0,0\rangle_{\text{AB}} \tag{2.9}$$

The HOM effect concerns with the coincidence probability as function of the degree of in/distinguishability between the interacting photons on the beam splitter. For the case where the photons are perfectly indistinguishable in all degrees of freedom, i.e., $j = k$, the terms associated with both photons reflected ($\hat{a}_k^{\dagger}\,\hat{b}_j^{\dagger}$) and both photons transmitted ($\hat{a}_j^{\dagger}\,\hat{b}_k^{\dagger}$) cancel out, resulting in the following N00N state [102]

$$|\Psi_{\text{out}}\rangle_{\text{AB}} = \frac{1}{2}\,((\hat{a}_{j=k}^{\dagger})^2 - (\hat{b}_{j=k}^{\dagger})^2)|0,0\rangle_{\text{AB}} \tag{2.10}$$
$$= \frac{1}{\sqrt{2}}\left(|2,0\rangle_{\text{AB}} - |0,2\rangle_{\text{AB}}\right)$$

which corresponds to zero coincidence count at zero delay (the HOM dip). The interference pattern of the HOM effect is illustrated in **Figure. 5**.

Under the condition of having distinguishable photons, i.e., for j≠k, the following terms $\hat{a}_{\text{k}}^{\dagger}\hat{b}_j^{\dagger}$ and $\hat{a}_{\text{j}}^{\dagger}\hat{b}_k^{\dagger}$ in Eq. 2.9 remain intact, which yields a coincidence event in the output port of the beam splitter. In a coincidence measurement, gradual exertion of distinguishability between the photons can be realized by, e.g., adjusting the photons' relative arrival time at the detectors. The time delay τ between the photons can be introduced by assigning a longer optical path length to one of the photon paths before arriving at the beam splitter. Under full temporal distinguishability, that is zero temporal overlap between the photons, the number of coincidence events registered at the detectors reaches its maximum (CC_{max}; creating the wings of the HOM effect) whereas at zero-time delay $\tau = 0$, that is under full

indistinguishability, the coincidence count rate lies at its minimum value (CC_{min}; ideally zero), see **Figure. 5**.

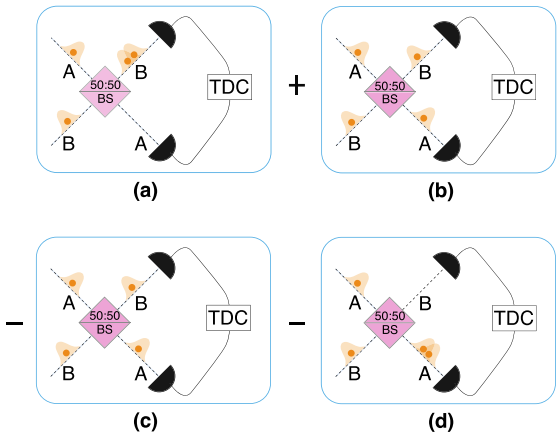

Figure. 4 Schematic illustration of the four output distribution possibilities for two photons impinging on a balanced beam splitter. **a)** Photon from port A reflected and photon from port B transmitted, **b)** both photons transmitted, **c)** both photons reflected, **d)** photon from port A transmitted and photon from port B reflected. (BS: beam splitter; TDC: time-to-digital convertor)

The visibility of the HOM interference effect can be calculated from the following relation $\mathrm{Vis} = (CC_{max} - CC_{min})/CC_{max}$.

2.6. The HOM Visibility and the Spectral Purity of Photons

The spectral purity of biphoton states from SPDC process is indispensable to obtain a high visibility in the HOM interference effect. Here, the impact of the spectral purity of the interacting photons on the visibility of the HOM effect is demonstrated, a concept which has been considered in the experimental implementations of the following chapters. Consider two independent pulsed-driven SPDC processes generating the following two frequency entangled states

$$|\Psi\rangle_{ab} = \int d\omega_{si} \int d\omega_{id}\ f(\omega_{si}, \omega_{id})\ \hat{a}^{\dagger}(\omega_{si})\ \hat{b}^{\dagger}(\omega_{id})|0,0\rangle_{ab} \tag{2.11}$$

$$|\Psi\rangle_{cd} = \int d\omega_{si} \int d\omega_{id}\ h(\omega_{si}, \omega_{id})\ \hat{c}^{\dagger}(\omega_{si})\ \hat{d}^{\dagger}(\omega_{id})|0,0\rangle_{cd}$$

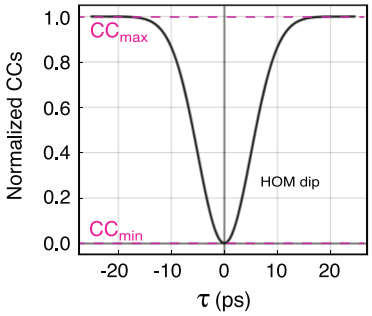

Figure. 5 Schematic illustration of the interference pattern of the HOM effect obtained from coincidence counts as function of the relative time delay (τ) between the interacting photons arriving at the beam splitter. (CC_{max}: maximum coincidence counts; CC_{min}: minimum coincidence counts)

The indices *a*, *b*, *c*, and *d* in the states $|\Psi\rangle_{ab}$ and $|\Psi\rangle_{cd}$ refer to the distinct emission paths (spatial modes) assumed for the signal and idler photons in each state. Here, $f(\omega_{si}, \omega_{id})$ and $h(\omega_{si}, \omega_{id})$ are the JSA functions for the biphoton state from each SPDC process, assumed to be normalized as follows $\iint d\omega_{si}\, d\omega_{id}\, |h(\omega_{si}, \omega_{id})|^2 = 1$ and $\iint d\omega_{si}\, d\omega_{id}\, |f(\omega_{si}, \omega_{id})|^2 = 1$. The creation operators $\hat{a}^\dagger(\omega_{si})$, $\hat{b}^\dagger(\omega_{id})$, $\hat{c}^\dagger(\omega_{si})$, and $\hat{d}^\dagger(\omega_{id})$ act on the signal and idler frequency modes.

Here, it is useful to consider the Schmidt decomposition of the JSA functions $f(\omega_{si}, \omega_{id}) = \sum_m \sqrt{u_m}\ \phi_m(\omega_{si})\phi'_m(\omega_{id})$ and $h(\omega_{si}, \omega_{id}) = \sum_{m'} \sqrt{v_{m'}}\ \varphi_{m'}(\omega_{si})\varphi'_{m'}(\omega_{id})$, where $\sqrt{u_m}$ and $\sqrt{v_{m'}}$ are the Schmidt coefficients such that $\sum_m u_m = \sum_{m'} v_{m'} = 1$, and $\phi_m(\omega)$ and $\varphi_{m'}(\omega)$ are the normalized spectral amplitude functions such that $\int d\omega\, |\phi_m(\omega)|^2 = \int d\omega\, |\varphi_{m'}(\omega)|^2 = 1$ corresponding to two distinct two-mode squeezers m and m', respectively.

Assume two signal photons from the biphoton states in Eq. 2.11, impinging on a balanced beam splitter from its two input ports monitoring *a* and *c* photon path directions. The coincidence probability between the detectors monitoring the output ports of the beam splitter is written $P_{coin} = \mathrm{Tr}[\rho^{out}\ \hat{P}_a \otimes \hat{P}_c]$, where ρ^{out} is the density matrix of the output state, and $\hat{P}_a$ and $\hat{P}_c$ are the projectors corresponding to a single detection on the detectors monitoring the output modes *a* and *c* of the beam splitter, respectively, defined as

$$\hat{P}_a = \int d\omega\ \hat{a}^\dagger(\omega)\, |0\rangle_a \langle 0|\, \hat{a}(\omega) \tag{2.12}$$

$$\hat{P}_c = \int d\omega\ \hat{c}^\dagger(\omega)\, |0\rangle_c \langle 0|\, \hat{c}(\omega)$$

The density matrix ρ^{out} is obtained under unitary transformation introduced by the beam splitter and under gradual exertion of different delay values τ. Here, ρ_ϕ and ρ_φ are the reduced density matrix in modes *a* and *c*, respectively, of the states in Eq. 2.11, written as

$$\rho_\phi = tr_b\left[|\Psi\rangle_{ab}\langle\Psi|\right] = \sum_m u_m\,|1;\phi_m\rangle_a\langle 1;\phi_m| \qquad (2.13)$$

$$\rho_\varphi = tr_d\left[|\Psi\rangle_{cd}\langle\Psi|\right] = \sum_{m'} v_{m'}\,|1;\varphi_{m'}\rangle_c\langle 1;\varphi_{m'}|$$

indicating a mixture of different spectral modes. Here, $|1;\phi_m\rangle_a = \int d\omega\;\phi_m(\omega)\;\hat{a}^\dagger(\omega)|0\rangle_a$ and $|1;\varphi_{m'}\rangle_c = \int d\omega\;\varphi_{m'}(\omega)\;\hat{c}^\dagger(\omega)|0\rangle_c$ are the superposition of single-photon states with spectral amplitude functions $\phi_m(\omega)$ and $\varphi_{m'}(\omega)$, respectively, corresponding to two distinct two-mode squeezers m and m'. The above single-photon states are mutually independent as a result of originating from different SPDC processes. The input state to the beam splitter can be written as $\left|\psi^{\text{in}}_{mm'}\right\rangle_{ac} = |1;\phi_m\rangle_a|1;\varphi_{m'}\rangle_c$ and the density matrix of the input state $\rho_{in} = \sum_{mm'} u_m v_{m'}(|1;\phi_m\rangle_a|1;\varphi_{m'}\rangle_c) \otimes (\langle 1;\phi_m|_a\langle 1;\varphi_{m'}|_c)$. The HOM effect can be probed by introducing a gradual time delay τ in one of the photon paths, say *c*, transforming $\left|\psi^{\text{in}}_{mm'}\right\rangle_{ac}$ to a time-delayed state as follows

$$\left|\psi^{td,\text{in}}_{mm'}\right\rangle_{ac} = \frac{1}{2}\int d\omega_1\phi_m(\omega_1)\hat{a}^\dagger(\omega_1)\int d\omega_2\;\varphi_{m'}(\omega_2)\;\hat{c}^\dagger(\omega_2)e^{-i\omega_2\tau}|0,0\rangle_{ac} \qquad (2.14)$$

Following the unitary transformation introduced by the beam splitter (see Eq. 2.7), the time-delayed input state in Eq. 2.14 evolves into the following output state

$$\left|\psi^{\text{out}}_{mm'}\right\rangle_{ac} = \frac{1}{2}\int d\omega_1\phi_m(\omega_1)\int d\omega_2\;\varphi_{m'}(\omega_2)e^{-i\omega_2\tau} \qquad (2.15)$$
$$\times\,(\hat{a}^\dagger(\omega_1)\;\hat{a}^\dagger(\omega_2) + \hat{a}^\dagger(\omega_2)\;\hat{c}^\dagger(\omega_1)$$
$$-\hat{a}^\dagger(\omega_1)\;\hat{c}^\dagger(\omega_2) - \;\hat{c}^\dagger(\omega_1)\;\hat{c}^\dagger(\omega_2))|0,0\rangle_{ac}$$

where the action of the beams plitter has been assumed frequency-independent. The density matrix of the output state is thus written as $\rho^{out} = \sum_{mm'} u_m v_{m'}\left|\psi^{\text{out}}_{mm'}\right\rangle_{ac}\left\langle\psi^{out}_{mm'}\right|$, and the probability of coincidence detection P_{coin} is expressed as follows

$$P_{coin} = \mathrm{Tr}\left[\rho^{out}\,\hat{P}_a \otimes \hat{P}_c\right] \qquad (2.16)$$
$$= \sum_{mm'} u_m v_{m'} \left\langle \psi^{out}_{mm'} \middle| \hat{P}_a \otimes \hat{P}_c \middle| \psi^{out}_{mm'} \right\rangle_{ac}$$

From Eq. 2.14 – 2.16, the probability of coincidence detections for two independent single photons generated from two independent pulsed-driven SPDC processes is derived as follows

$$P_{coin} = \frac{1}{2} - \frac{1}{2}\sum_{mm'} u_m v_{m'} \int d\omega_1 \phi^*_m(\omega_1)\,\varphi_{m'}(\omega_1) e^{-i\omega_1\tau} \qquad (2.17)$$
$$\times \int d\omega_2\, \varphi^*_{m'}(\omega_2)\phi_m(\omega_2) e^{-i\omega_2\tau}$$

where * denotes the transpose conjugate of the spectral amplitude functions. The HOM visibility can be defined in terms of the maximum and minimum coincidence probabilities such that

$$\mathrm{Vis} = \frac{P^{max}_{coin} - P^{min}_{coin}}{P^{max}_{coin}} \qquad (2.18)$$

The maximum coincidence probability is obtained at large delay values where photons are temporally fully distinguishable, resulting in $P^{max}_{coin} = \lim_{\tau\to\infty} P_{coin} = 1/2$. The minimum coincidence probability $\mathrm{P}^{\mathrm{min}}_{\mathrm{coin}}$ corresponds to the full indistinguishability in all degrees of freedom. This would mean an identical density matrix for the interacting photons, i.e., $\varphi_{m'} = \phi_m$ and $u_m = v_{m'}$ in Eq. 2.13. The minimum coincidence probability is calculated as follows

$$P^{min}_{coin} = \lim_{\tau\to 0} P_{coin} \qquad (2.19)$$
$$= \frac{1}{2} - \frac{1}{2}\sum_m u_m^2$$

The HOM visibility is thus obtained as $\mathrm{Vis} = \sum_m u_m^2$, which is equivalent to the definition of the spectral purity for each photon. Given the reduced density matrix of photon in Eq. 2.13, it follows that

$$\text{Purity} = \text{tr}\left[\rho_{\phi}^{2}\right] = \sum_{m} u_{m}^{2} \,. \tag{2.20}$$

It is thus concluded that for a pure biphoton state (*purity* = 1), the total number of terms in Eq. 2.20 reduces to one, that is the system would be composed of one dominant spectral mode, which is equivalent to the definition of spectral purity allowing for a 100% visibility in the HOM effect. The equivalence between the spectral purity of the interacting photons and the HOM visibility demonstrates the significance of spectral purity to achieving high visibility in the HOM effect. This fact is taken into account for the experimental implementation of the HOM effect in chapters four and five, and to obtain quantum interference of high visibility in chapter six.

2.7. Theory of Second-order Optical Coherence

The theory of optical coherence of light explores the statistical properties of electromagnetic waves in degrees-of-freedom such as time and space [103,104]. This theory has enabled the development of important experimental interferometry which has contributed to the understanding of light at the quantum level. In this thesis, the focus is in particular on the second-order coherence, enabling us to ascertain the spectral purity and photon statistical properties. Here, the generalized theory of second-order optical coherence is explained to provide the reader with an understanding of this theory deployed in the calculations and experiments of this thesis. Specifically, the theory of second-order optical coherence is deployed in combination with the HBT interferometry (see Sec. 2.10) to measure the single frequency mode bandwidth of the biphoton states and to ensure high spectral purity of the photons, and in turn to facilitate quantum interference of high visibility.

Consider two light sources A and B placed in locations $\mathbf{R}_A$ and $\mathbf{R}_B$, and spatially distanced by **d** (see **Figure. 6**). The light sources emit independent photons with an arbitrary classical, quantum, or semi-quantum photon statistics. Two detectors are placed at spatial positions $\mathbf{r}_1$ and $\mathbf{r}_2$ and record the incidence of photons. We assume $\left|\mathbf{r}_i - \mathbf{R}_j\right| \gg \boldsymbol{d}$ (i =1, 2 and j = A, B) so that the far-field condition is met. The coincidence detections are recorded as function of the time-difference between the clicks on each detector using a timing electronics module. According to the Glauber notation [103], the second-order correlation

function $G^2(\mathbf{r}_1, t_1; \mathbf{r}_2, t_2)$ associated with the interaction of two photons from the two independent light sources A and B is written as follows

$$G^{(2)}(\mathbf{r}_1, t_1; \mathbf{r}_2, t_2) = \langle : \hat{\mathbf{E}}^{(-)}_{A+B}(\mathbf{r}_1, t_1)\, \hat{\mathbf{E}}^{(-)}_{A+B}(\mathbf{r}_1, t_1)\, \hat{\mathbf{E}}^{(+)}_{A+B}(\mathbf{r}_2, t_2)\, \hat{\mathbf{E}}^{(+)}_{A+B}(\mathbf{r}_2, t_2) : \rangle \qquad (2.21)$$

where the terms on the right-hand side are the positive- and negative-frequency electric-filed operators, $(\hat{\mathbf{E}}^{-}_{A+B})^{\dagger} = \hat{\mathbf{E}}^{+}_{A+B}$, and the notation $\langle :: \rangle$ indicates ensemble averaging under the assumption to have stationary light sources. The colons :: represent the normal ordering of the operators [96], which specifies the standard arrangement of the creation and destruction operators.

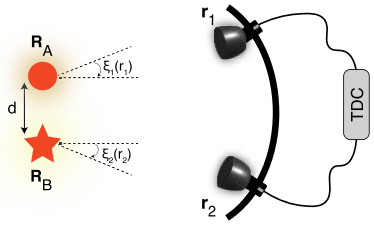

Figure. 6 Schematic illustration of measuring the second-order correlation function $G^{(2)}(r_1, t_1; r_2, t_2)$ for the emission from two light sources A and B. (TDC: Time-to-digital convertor)

In Eq. 2.21, the positive-frequency electric-field operator is defined as

$$\hat{\mathbf{E}}^{+}_{A+B}(\mathbf{r}_I, t_i) = \hat{\mathbf{A}}^{+}_i + \hat{\mathbf{B}}^{+}_i \propto e^{-i(k_A\, \hat{\mathbf{r}}_I\, R_A + \phi_A)}\, \hat{\boldsymbol{a}} + e^{-i(k_B\, \hat{\mathbf{r}}_I\, R_B + \phi_B)}\, \hat{\boldsymbol{b}} \qquad (2.22)$$

which indicates the superposition of fields at the location of the detectors. In Eq. 2.22, $\hat{\boldsymbol{a}}$ and $\hat{\boldsymbol{b}}$ denote the photon annihilation operators for sources A and B, respectively, $k = {}^{\omega}/_{c}$ is the wave number of the light source, $\hat{\mathbf{r}}_i = \mathbf{r}_i/|\mathbf{r}_i|$ is the unit vector corresponding to the direction of detectors, and ϕ_A and ϕ_B are the initial phase values of the photons emitted from the sources A and B. The generalized second-order correlation function in Eq. 2.21 is thus rewritten as it follows

$$\begin{aligned} G^{(2)}(\mathbf{r}_1, t_1; \mathbf{r}_2, t_2) &= \langle (\hat{\mathbf{A}}^{-}_1 + \hat{\mathbf{B}}^{-}_1)(\hat{\mathbf{A}}^{-}_2 + \hat{\mathbf{B}}^{-}_2)(\hat{\mathbf{A}}^{+}_2 + \hat{\mathbf{B}}^{+}_2)(\hat{\mathbf{A}}^{+}_1 + \hat{\mathbf{B}}^{+}_1) \rangle \qquad (2.23) \\ &= \langle \hat{\mathbf{A}}^{-}_1 \hat{\mathbf{A}}^{-}_2 \hat{\mathbf{A}}^{+}_2 \hat{\mathbf{A}}^{+}_1 \rangle + \langle \hat{\mathbf{B}}^{-}_1 \hat{\mathbf{B}}^{-}_2 \hat{\mathbf{B}}^{+}_2 \hat{\mathbf{B}}^{+}_1 \rangle + \langle \hat{\mathbf{B}}^{-}_1 \hat{\mathbf{A}}^{-}_2 \hat{\mathbf{A}}^{+}_2 \hat{\mathbf{B}}^{+}_1 \rangle \\ &\quad + \langle \hat{\mathbf{A}}^{-}_1 \hat{\mathbf{B}}^{-}_2 \hat{\mathbf{B}}^{+}_2 \hat{\mathbf{A}}^{+}_1 \rangle + \langle \hat{\mathbf{A}}^{-}_1 \hat{\mathbf{B}}^{-}_2 \hat{\mathbf{A}}^{+}_2 \hat{\mathbf{B}}^{+}_1 \rangle + \langle \hat{\mathbf{B}}^{-}_1 \hat{\mathbf{A}}^{-}_2 \hat{\mathbf{B}}^{+}_2 \hat{\mathbf{A}}^{+}_1 \rangle \end{aligned}$$

In Eq. 2.23, depending on the photon-statistical properties of the light sources, different terms can take different values. For example, for two single-photon states, the terms $\langle \hat{\mathbf{A}}_1^- \hat{\mathbf{A}}_2^- \hat{\mathbf{A}}_2^+ \hat{\mathbf{A}}_1^+ \rangle$, $\langle \hat{\mathbf{B}}_1^- \hat{\mathbf{B}}_2^- \hat{\mathbf{B}}_2^+ \hat{\mathbf{B}}_1^+ \rangle$, $\langle \hat{\mathbf{B}}_1^- \hat{\mathbf{A}}_2^- \hat{\mathbf{A}}_2^+ \hat{\mathbf{B}}_1^+ \rangle$, $\langle \hat{\mathbf{A}}_1^- \hat{\mathbf{B}}_2^- \hat{\mathbf{B}}_2^+ \hat{\mathbf{A}}_1^+ \rangle$ will be excluded owing to their neutral effect in creation and annihilation of single photons. Noteworthy, the terms $\langle \hat{\mathbf{A}}_1^- \hat{\mathbf{B}}_2^- \hat{\mathbf{A}}_2^+ \hat{\mathbf{B}}_1^+ \rangle$ and $\langle \hat{\mathbf{B}}_1^- \hat{\mathbf{A}}_2^- \hat{\mathbf{B}}_2^+ \hat{\mathbf{A}}_1^+ \rangle$ lead to two-photon interference and their values depend on how perfectly the interacting photons are indistinguishable.

2.8. Second-order Optical Coherence and the HOM Visibility

Consider the interaction of two photons emitted from two independent photon sources with an arbitrary photon statistic, impinging on a balanced beam splitter from its two input ports 1 and 2. In this case – which is of interest in this thesis for the implementation of the HOM effect – the definition of the $\mathrm{G}^{(2)}$ function in Eq. 2.23 is reduced to be only dependent on the temporal degree-of-freedom. Assume that the output ports of the beam splitter are monitored by two detectors labelled D1 and D2. The electric field operators $\hat{E}_{D1}(t)$ and $\hat{E}_{D2}(t)$ at the detectors are written as

$$\hat{E}_{D1}(t) = \frac{1}{\sqrt{2}}(\hat{E}_1(t) + \hat{E}_2(t)) \tag{2.24}$$

$$\hat{E}_{D2}(t) = \frac{1}{\sqrt{2}}(\hat{E}_1(t) - \hat{E}_2(t))$$

where $\hat{E}_1(t)$ and $\hat{E}_2(t)$ are the field operators corresponding to the light in the input ports of the beam splitter. Following from Eq. 2.23, the second-order optical coherence is here defined by removing the dependency on the spatial degree of freedom, such that

$$\begin{aligned} \mathrm{G}^{(2)}(t;t') &= \langle : \hat{E}_{D1}^{(-)}(t)\, \hat{E}_{D2}^{(-)}(t')\, \hat{E}_{D2}^{(+)}(t')\, \hat{E}_{D1}^{(+)}(t) : \rangle \\ &= \langle \hat{a}_1^\dagger(t)\, \hat{a}_1^\dagger(t')\, \hat{a}_1(t')\, \hat{a}_1(t) \rangle + \langle \hat{a}_2^\dagger(t)\, \hat{a}_2^\dagger(t')\, \hat{a}_2(t')\, \hat{a}_2(t) \rangle \\ &\quad + \langle \hat{a}_1^\dagger(t)\, \hat{a}_2^\dagger(t')\, \hat{a}_2(t')\, \hat{a}_1(t) \rangle + \langle \hat{a}_2^\dagger(t)\, \hat{a}_1^\dagger(t')\, \hat{a}_1(t')\, \hat{a}_2(t) \rangle \\ &\quad - \langle \hat{a}_1^\dagger(t)\, \hat{a}_2^\dagger(t')\, \hat{a}_1(t')\, \hat{a}_2(t) \rangle - \langle \hat{a}_2^\dagger(t)\, \hat{a}_1^\dagger(t')\, \hat{a}_2(t')\, \hat{a}_1(t) \rangle \end{aligned} \tag{2.25}$$

where $\hat{a}_i^\dagger(t)$ and $\hat{a}_i(t)$ are the photon creation and annihilation operators acting on each input port (i = 1, 2), respectively. In this thesis, the formulation in Eq. 2.25 is used to calculate the first and second-order moments of states of light with different photon statistics, namely, imperfect single-photon states from SPDC process and thermal distribution of photons. In this formulation, the degree of temporal distinguishability between the interacting photons determines the value of the terms containing phase information, i.e., $\langle \hat{a}_1^\dagger(t)\hat{a}_2^\dagger(t')\hat{a}_1(t')\hat{a}_2(t)\rangle$ and $\langle \hat{a}_2^\dagger(t)\hat{a}_1^\dagger(t')\hat{a}_2(t')\hat{a}_1(t)\rangle$, in turn quantifying the maximum $\mathrm{G}^{(2)}(t;t')_{\max}$ and minimum $\mathrm{G}^{(2)}(t;t')_{\min}$ values of the optical coherence function. The visibility of the HOM effect can thus be expressed as follows

$$\mathrm{Vis} = \frac{\mathrm{G}^{(2)}(t;t')_{\max} - \mathrm{G}^{(2)}(t;t')_{\min}}{\mathrm{G}^{(2)}(t;t')_{\max}} \tag{2.26}$$

which is used in chapter five to obtain the HOM visibility between a thermal field and a heralded state.

2.9. Chaotic Light Source and the Thermal Photon Statistics

In this section, the photon statistics of a thermal distribution of photons is reviewed, providing a basis for the calculations and the experimental implementation of the HOM effect in chapter five of this thesis. A chaotic light source can be considered as a train of electromagnetic emissions from excited atoms radiating at a given frequency ω_0. In a chaotic light source with elastic collisions, random changes in the phase of radiation is introduced, whereas the radiation frequency is preserved.

The photon statistics in a chaotic light source is governed by a thermal probability distribution written as $\mathrm{P_{th}} = \exp(-\hbar\omega\hat{a}^\dagger\hat{a}/k_b\mathrm{T})/\mathrm{Tr}(\exp(-\hbar\omega\hat{a}^\dagger\hat{a}/k_b\mathrm{T}))$, where k_b is the Boltzmann constant and T is the temperature of the cavity, within the boundary of which the radiation is confined [105]. The normalization term $\mathrm{Tr}(\exp(-\hbar\omega\hat{a}^\dagger\hat{a}/k_b\mathrm{T}))$ can be simplified to $1/(1-\exp(-\hbar\omega/\mathrm{k_bT}))$, and the probability distribution is rewritten as

$$\mathrm{P_{th}} = (1-\exp(-\frac{\hbar\omega}{k_bT}))\exp(\frac{-\hbar\omega\hat{a}^\dagger\hat{a}}{k_bT}) \tag{2.27}$$

For the calculations in this thesis, it is useful to reformulate the probability distribution P_{th} in terms of the average photon number $\langle n\rangle_{\text{th}} = \text{Tr}(\hat{a}^{\dagger}\hat{a}\,\rho_{\text{th}})$. For a chaotic light source as an example of a statistical mixture, the density matrix ρ_{th} is written as

$$\hat{\rho}_{\text{th}} = \sum_{n=0}^{\infty} P_{\text{th}}\,|n\rangle\langle n| = (1-\exp(-\frac{\hbar\omega}{k_bT}))\sum_{n=0}^{\infty}\exp(-\frac{\hbar\omega\hat{n}}{k_bT})\,|n\rangle\langle n| \tag{2.28}$$

where $\{|n\rangle\}$ is the orthonormal photon-number basis space, and $\hat{n} = \hat{a}^{\dagger}\hat{a}$ is the photon-number operator. The average photon number in the thermal field $\langle n\rangle_{\text{th}}$ is obtained as follows

$$\begin{aligned}\langle n\rangle_{\text{th}} &= \text{Tr}(\hat{a}^{\dagger}\hat{a}\,\hat{\rho}_{\text{th}}) \\ &= (1-\exp(-\frac{\hbar\omega}{k_bT}))\sum_{n=0}^{\infty} n\,(\exp(-\frac{\hbar\omega}{k_bT}))^n \\ &= (1-\exp(-\frac{\hbar\omega}{k_bT}))\exp(-\frac{\hbar\omega}{k_bT})\Big/(1-\exp(-\frac{\hbar\omega}{k_bT}))^2 \\ &= \exp(-\frac{\hbar\omega}{k_bT})\Big/(1-\exp(-\frac{\hbar\omega}{k_bT}))\end{aligned} \tag{2.29}$$

By rearranging the terms in Eq. 2.29, the thermal probability distribution P_{th} in Eq. 2.27 can be expressed in terms of the average photon number in the thermal field $\langle n\rangle_{\text{th}}$ such that

$$P_{\text{th}}(n) = \frac{\langle n\rangle_{th}^{n}}{(1+\langle n\rangle_{th})^{1+n}} \tag{2.30}$$

The density matrix $\hat{\rho}_{th}$ of a thermal field in Eq. 2.28 can be reformulated as function of $\langle n\rangle_{\text{th}}$ such that

$$\hat{\rho}_{th} = (1-\frac{\langle n\rangle_{th}}{1+\langle n\rangle_{th}})\sum_{n=0}^{\infty}(\frac{\langle n\rangle_{th}}{1+\langle n\rangle_{th}})^n|n\rangle\langle n| \tag{2.31}$$

$$= \sum_{n=0}^{\infty} \frac{\langle n \rangle_{th}^{n}}{(1 + \langle n \rangle_{th})^{n+1}} |n\rangle\langle n|$$

The final relationship in Eq. 2.31 is used in the calculations of chapter five to obtain the first and second-order moments of the thermal distribution of photons, involved in the HOM effect with a heralded state.

2.10. The HBT Interferometry

The Hanbury Brown & Twiss (HBT) interferometry is a technique utilized in quantum optics to measure the statistical properties of photon distributions. This technique is named after Robert Hanbury Brown and Richard Q. Twiss, who originally developed the HBT interferometry to measure the diameter of discrete radio sources [67]. Ever since, the HBT interferometry is widely deployed in experiments as a tool to measure the second-order degree of correlation $g^{(2)}$ as function of temporal coherence of biphoton states from nonlinear parametric processes. The $g^{(2)}$ function takes specific values within certain boundaries which allows to infer the photon statistical properties and in turn the nature of the emission source [106,107]. The measurement of the $g^{(2)}$ function is crucial to the experiments in this thesis for determining the spectral purity of photons required to obtain high visibility of quantum interference.

In the original HBT interferometry (see **Figure. 7**), a balanced beam splitter is employed with an arbitrary input state $|\mathrm{arb}\rangle_1$ in its input port 1 and a vacuum state $|0\rangle_2$ in its input port 2. Gradual delay τ is introduced in one of the two input arms of the beam splitter. Two single-photon detectors are placed at the output ports 3 and 4, recording the incidence of photons. The time difference τ between the clicks on the detectors is recorded via a timing electronics module. A coincidence measurement between the detectors quantifies the cross-correlation function $g_{3,4}^{(2)}(\tau)$ between the output ports, such that

$$g_{3,4}^{(2)}(\tau) = \frac{\langle \hat{a}_3^{\dagger}(t)\hat{a}_4^{\dagger}(t+\tau)\hat{a}_4(t+\tau)\hat{a}_3(t)\rangle}{\langle \hat{a}_3^{\dagger}(t)\hat{a}_3(t)\rangle\langle \hat{a}_4^{\dagger}(t+\tau)\hat{a}_4(t+\tau)\rangle} \tag{2.32}$$

$$= \frac{\langle \hat{n}_3(t)\hat{n}_4(t+\tau)\rangle}{\langle \hat{n}_3(t)\rangle\langle \hat{n}_4(t+\tau)\rangle}$$

where $\hat{n}_3(t) = \hat{a}_3^\dagger(t)\hat{a}_3(t)$ and $\hat{n}_4(t+\tau) = \hat{a}_4^\dagger(t+\tau)\hat{a}_4(t+\tau)$ are the photon number operators for the output ports 3 and 4, respectively. Considering the unitary transformation of a balanced beam splitter (see Sec. 2.5), it can be proved that the normalized cross-correlation function in Eq. 2.32 is equivalent to the auto-correlation function of the arbitrary input state $|\mathrm{arb}\rangle_1$ as it follows (see **Appendix I**)

$$g_{3,4}^{(2)}(\tau) = \frac{\langle \hat{a}_1^\dagger(t)\hat{a}_1(t)\hat{a}_1^\dagger(t+\tau)\hat{a}_1(t+\tau) - \hat{a}_1^\dagger(t)\hat{a}_1(t)\rangle}{\langle \hat{a}_1^\dagger(t)\hat{a}_1(t)\rangle\langle \hat{a}_1^\dagger(t+\tau)\hat{a}_1(t+\tau)\rangle} \tag{2.33}$$

$$= \frac{\langle \hat{n}_1(t)(\hat{n}_1(t+\tau) - 1)\rangle}{\langle \hat{n}_1(t)\rangle\langle \hat{n}_1(t+\tau)\rangle}$$

$$= g_{1,1}^{(2)}(\tau)$$

The degree of second order coherence for a single-mode radiation is independent of the time variable and is rather dependent on the nature of the light beam [96]. Under single-mode assumption, the auto-correlation function $g_{1,1}^{(2)}(\tau)$ can thus be written

$$g_{1,1}^{(2)}(0) = \langle \hat{n}_1^2 - \hat{n}_1\rangle / \langle \hat{n}_1\rangle^2 \tag{2.34}$$

$$= 1 + \frac{(\Delta\hat{n}_1)^2 - \langle \hat{n}_1\rangle}{\langle \hat{n}_1\rangle^2}$$

where the variance $(\Delta\hat{n}_1)^2 = \langle \hat{n}_1{}^2\rangle - \langle \hat{n}_1\rangle^2$ quantifies the photon number fluctuations of the arbitrary input state.

As an example, consider photon-number states for which the photon number fluctuations are $(\Delta\hat{n})^2 = 0$. The final formulation in Eq. 2.34 is thus simplified to $g^{(2)}(0) = 1 - 1/\langle \hat{n}\rangle$. The degree of second-order coherence for the number states falls within the following range $1 - 1/\langle \hat{n}\rangle \leq g^{(2)}(0) < 1$. Noteworthy, a light source with $g^{(2)}(0) < 1$ is an anti-bunched light with a subpoissonian statistics, which is a characteristic of a non-classical light [108]. In the experiments of chapter five it is required to assess how perfect a heralded state from SPDC process can be approximated as a perfect single-photon state. Noteworthy, an auto-correlation function that falls below one $g^{(2)}(0) < 1$ does not necessarily imply a single-photon state. The necessary and sufficient condition to conclude that a state is a good approximation of a single-photon state is to measure $g^{(2)}(0) < 0.5$.

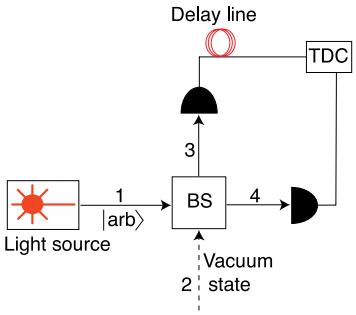

Figure. 7 Hanbury Brown and Twiss (HBT) interferometry. (TDC: Time-to-digital convertor; arb: arbitrary state)

For the calculations of chapter five, it is also useful to note that the r^{th} factorial moment (r as any positive integer number) for a thermal distribution of photons is governed by the following equation

$$P_{th}(n) = \langle n(n-1)(n-2)\dots(n-r+1)\rangle \qquad (2.35)$$
$$= \sum_n n(n-1)(n-2)\dots(n- \ r+1)$$
$$= \ r!\,\langle n\rangle^r$$

from which it follows that $\langle n(n-1)\rangle = 2\langle n\rangle^2$. The photon number variance in a thermal distribution can thus be written as $(\Delta n)^2 = \langle n\rangle^2 + \langle n\rangle$, from which the degree of second-order coherence for a thermal light is thus obtained $g^{(2)}(0) = 2$.

In experiments, alternative to gradual exertion of delay τ in one of the input arms of the beam splitter, the second-order degree of temporal coherence $g^{(2)}(\tau)$ can be measured by sweeping the spectral filter bandwidth, leading to gradual decrease of the $g^{(2)}$ function from 2 to 1. The spectral filter bandwidth at which $g^{(2)}(0) = 2$ is measured, is considered as the single frequency mode bandwidth of the biphoton state. The achievable spectral resolution in this method is however limited to the frequency resolving capability of the spectral filtering device. This will be discussed in detail in chapter three where the first time direct measurement of the second-order degree of coherence in the frequency domain $g^{(2)}(v)$, i.e., by probing the frequeny correlations, is demonstrated.

2.11. Measurement of the Single Frequency Mode Bandwidth

In this thesis, the HBT experiment was performed to measure the number of frequency modes as function of the spectral filter bandwidth. In **Figure. 8**, the measurement results are presented for the pulsed-driven SPDC process in the *Covesion* PPLN waveguide. According to Eq. 2.6, the spectral purity is inversely related to the number of effective frequency modes the photon contains, which can be controlled by the spectral filtering of the signal and idler spectrum. In this experiment, the PPLN waveguide was pumped by pulsed excitation with a spectrally filtered bandwidth of $\sigma_{\mathrm{p}} = 200$ GHz. The programmable filter was adjusted at its finest resolution $\sigma_{\mathrm{f}} = 10$ GHz and the power from the idler frequency mode was half split using the filter's split mode of operation. The coincidence detections were collected using two superconducting nanowire single-photon detectors (SNSPD) followed by a time-to-digital convertor (TDC) module. In this experiment, the spectral filter bandwidth was gradually increased to incorporate higher number of frequency modes (K) and the corresponding second-order auto-correlation function $g^{(2)}(0)$ was measured at $\tau = 0$ for each bandwidth. The value of $g^{(2)}(0) = 2 \pm 0.0645$ was obtained at 10 GHz corresponding to K $\approx$ 1, equivalent to a maximum spectral purity of p = 99.65% $\pm$ 6.5%, (see **Figure. 8**). Considering the standard deviation of 6.5% for the spectral purity (1/K) and the following relationship $\mathrm{g}^{(2)}(0) = 1 + 1/\mathrm{K}$, the single frequency mode bandwidth could thus be approximated at the full-width half-maximum (FWHM) of ~50-55 GHz, which is considered in defining the spectral configurations of the experiments in this thesis. Noteworthy, a narrow-band continuous-wave excited SPDC process would not allow to prepare single-frequency mode photons, since the single-mode bandwidth in such cases is of the order of kHz which is much narrower than the filtering capability offered by todays elaborated filtering techniques. This highlights the importance of using pulsed excitation.

2.12. The Degree of Second-order Coherence for Superimposed Beams

For the superposition of two independent stationary beams, denoted by *a* and *b*, that are distinct in some degrees of freedom such as polarization or the frequency mode, the degree of second-order coherence $g_s^{(2)}(\tau)$ is obtained from the following equation [96]

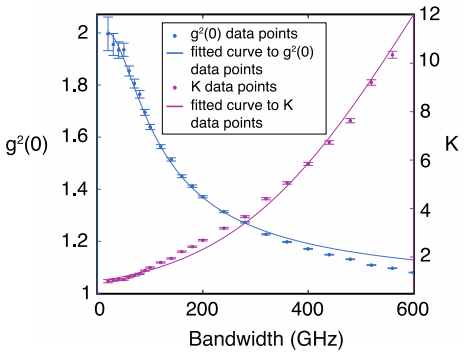

Figure. 8 The results from the Hanbury Brown and Twiss (HBT) experiment showing the second order correlation function $g^{(2)}(0)$ (left axis) and the number K of frequency modes (right axis) as function of the spectral filter bandwidth. The error bars are the standard deviation for 10 min integration time per measurement. The solid lines are the theoretical fit (see Eq. 2.6) to the experimental data with a Gaussian spectral filtering.

$$g_s^{(2)}(\tau) = \frac{\bar{n}_a^2\, g_{a,a}^{(2)}(\tau) + \bar{n}_b^2\, g_{b,b}^{(2)}(\tau) + 2\bar{n}_a\bar{n}_b}{(\bar{n}_a + \bar{n}_b)^2} \tag{2.36}$$

where τ is the delay between the arrival time at the beam splitter of the two interacting beams. For equal average photon number, $\bar{n}_a = \bar{n}_b$, and equal degree of second-order coherence for individual fields, $g_{a,a}^{(2)}(\tau) = g_{b,b}^{(2)}(\tau)$, the degree of second-order coherence for the superposition of the beams is simplified to the following

$$g_s^{(2)}(\tau) = \tfrac{1}{2}\left\{1 + g_{a,a}^{(2)}(\tau)\right\}, \tag{2.37}$$

suggesting a value of $g^{(2)}(0) = 1.5$ at $\tau = 0$, which is used in the thesis for the calculation of the HOM interference visibility between two thermal fields.

2.13. Heralded Single-photon States from SPDC Process

An ideal single-photon source emits deterministic single-photon states with a probability of unity. Heralding technique has been widely deployed to prepare probabilistic (thus imperfect) single-photon states from parametric processes such as SPDC and SFWM. The heralding technique relies on two fundamental properties of down-converted photon pairs, namely, high temporal correlations between the signal and idler photons, and identical

photon-number occupation probabilities for the signal and idler modes in each parametric process [100].

In this thesis, the experimental implementation of the HOM effect between a heralded state and a thermal field is demonstrated. To support the discussions in chapter five, a review over some essential properties of heralded states from SPDC process and the theoretical background required for the calculations of the HOM visibility between a heralded state and a thermal field is presented.

2.13.1. Density Matrix of SPDC Process

The parametric down-conversion process as a source of photon pair generation is involved in the heralding approach to prepare imperfect single-photon states. The joint state of *n* signal-idler photon pairs from an SPDC process is described as

$$|\Psi(r)\rangle_{si,id} = e^{r(\hat{a}^\dagger \hat{b}^\dagger - \hat{a}\hat{b})}|0\rangle_{si}|0\rangle_{id} \tag{2.38}$$

$$= \operatorname{sech} r \sum_{n=0}^{\infty} \tanh^n r |n\rangle_{si}|n\rangle_{id}$$

where the indices *si* and *id* refer to the signal and idler modes, respectively, r is the degree of squeezing which depends on the pump power amplitude, the second-order nonlinear susceptibility of the crystal, and the crystal length. Given the inherent random nature of photon pair generation in a parametric down-conversion source, the distribution of photon pairs follows a statistical mixture that is described by a thermal distribution. The density matrix corresponding to the generation of signal-idler photon pairs is written as

$$\rho_{th}^{\mathrm{SPDC}}(\xi) = |\Psi(r)\rangle_{si,id}\langle\Psi(r)| \tag{2.39}$$

$$= \operatorname{sech}^2 \mathrm{r} \sum_{n=0}^{\infty} \tanh^{2\mathrm{n}} \mathrm{r}\ |n;n\rangle_{si,id}\langle n,n|$$

$$= (1-\xi) \sum_{n=0}^{\infty} \xi^n |n;n\rangle_{si,id}\langle n,n|$$

where $\xi = tanh^2 r = \exp(-\hbar\omega/k_B T)$ is a parameter associated with the initial brightness of the SPDC source. From Eq. 2.29, it follows that ξ can be expressed in terms of thermal

average photon number as follows $\xi = \langle n \rangle_{th}/(1 + \langle n \rangle_{th})$. For values of $\xi \to 0$ corresponding to temperatures T → 0, the PDC process inclines to the spontaneous regime and the density matrix approaches to the definition of a vacuum state, i.e., $\rho_{th}^{\mathrm{SPDC}}(\xi \to 0) = |0;0\rangle\langle 0;0|$.

2.13.2. Density Matrix of a Heralded State from SPDC Process

In this section, the photon-number representation of the density matrix of a heralded state from an SPDC process is presented. Consider the generation of signal-idler photon pairs from an SPDC source illustrated in **Figure 9**. Here, it is assumed that the signal and idler channels are loss-free, which is equivalent to assuming a quantum efficiency of unity ($\eta = \mu = 1$) for these channels.

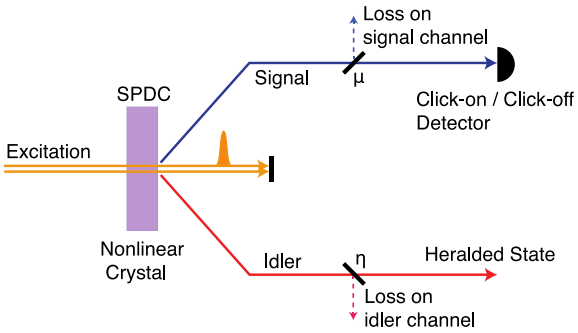

Figure. 9 Preparing a heralded state from SPDC process. The quantum efficiency of the signal and idler channels is represented with a beam splitter with transmission coefficients μ and η, respectively. A click on the detector heralds the presence of a photon in the idler mode.

A click-on click-off detector is employed for the detection of signal photons and every single detection on the signal mode heralds the presence of one photon in the idler mode, hence a heralded state. Under unitary transmission, the positive operator valued measurement associated with a single click on the detector monitoring the signal mode is defined as $\Pi_{\mathrm{si}}^{\mathrm{on}} = \mathbb{I}_{\mathrm{si}} - \Pi_{\mathrm{si}}^{\mathrm{off}}$ where $\Pi_{\mathrm{si}}^{\mathrm{off}} = |0\rangle_{si}\langle 0|$ corresponds to zero clicks on this detector and $\mathbb{I}_{\mathrm{si}}$ is the identity matrix. The conditional state prepared in the idler mode can be expressed as the reduced density matrix of the SPDC process on its signal mode, such that [109]

$$\rho_h^{\mathrm{id}} = \mathrm{Tr}_{\mathrm{si}}\{\Pi_{\mathrm{si}}^{\mathrm{on}} |\Psi(r)\rangle_{\mathrm{SPDC}}\langle\Psi(r)|\} \tag{2.40}$$

$$= \mathrm{Tr}_{\mathrm{si}}\left\{\rho_{th}^{\mathrm{SPDC}}(\xi)\right\} - \mathrm{Tr}_{\mathrm{si}}\left\{|\Psi(r)\rangle_{\mathrm{SPDC}}\langle\Psi(r)|\otimes|0\rangle_{\mathrm{si}}\langle 0|\right\}$$

$$= \rho_{th}^{\mathrm{id}}(\xi) - (1-\xi)|0\rangle_{\mathrm{id}}\langle 0|$$

where $\rho_{th}^{\mathrm{id}}(\xi)$ is the density matrix corresponding to the thermal distribution of photons in the idler frequency mode upon tracing out the signal mode. The normalized density operator $\tilde{\rho}_h^{\mathrm{id}}$ for the heralded state thus reads

$$\tilde{\rho}_h^{id} = \rho_h^{id} \,/\, \mathrm{Tr}\{\rho_h^{id}\} \tag{2.41}$$

$$= \rho_h^{id} \,/\, \xi$$

$$= \frac{(1-\xi)}{\xi}\left(\frac{\rho_{th}^{id}(\xi)}{1-\xi} - |0\rangle_{id}\langle 0|\right)$$

which can also be identified as a vacuum-removed state. Eq. 2.41 is used in chapter five to derive the first and second-order moments of the heralded state.

2.13.3. Heralded Auto-correlation Function

Higher-order emissions in SPDC process result in the generation of multiphoton components within the coherence time of one pulse. Multiphoton contamination in heralded states degrades the quantum interference visibility and leads to security loopholes in e.g. quantum key distribution, errors in the operation of quantum photonic gates, and degraded overall performance of quantum algorithms [110,111]. It is thus important to quantify the amount of multiphoton components in the heralded states. The heralded second-order auto-correlation function $g_h^{(2)}(\tau)$ is a common quality metric with which the likelihood of multiphoton components in a heralded state can be quantified. The $g_h^{(2)}(\tau)$ function allows to estimate how closely a heralded state approximates a perfect single-photon state. The HBT interferometry for a heralded state is shown in **Figure. 10** which can be used for the measurement of the $g_h^{(2)}(\tau)$ function in the idler mode. In this setup, the heralding signal photons are detected by detector D1, whereas the idler beam is half split by a balanced beam splitter and detected by two detectors D2 and D3. A TDC module is employed to record the two- and three-fold coincidence events on detectors D1, D2 and D3.

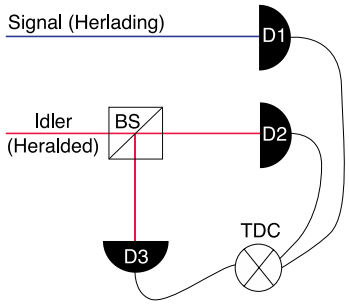

Figure. 10 Conceptual illustration of the HBT interferometry for measuring the heralded auto-correlation function $g_h^{(2)}(\tau)$. TDC: time-to-digital convertor.

The $g_h^{(2)}(\tau)$ function corresponding to the idler mode can be calculated from the following equation

$$g_h^{(2)}(\tau) = \frac{\mathrm{N}_{\mathrm{D2,D3|D1}}(\tau)}{\mathrm{N}_{\mathrm{D1,D2}}(0)\,\mathrm{N}_{\mathrm{D1,D3}}(\tau)}\mathrm{N}_{\mathrm{D1}} \tag{2.42}$$

where $\mathrm{N}_{\mathrm{D2,D3|D1}}$ is the three-fold coincidence counts, N_{D1} is the single detection counts from the heralding signal mode, and in the denominator, $\mathrm{N}_{\mathrm{D1,D2}}$ and $\mathrm{N}_{\mathrm{D1,D3}}$ are the two-fold coincidence counts between the heralding signal detections on D1 and the heralded idler detections on D2 and D3. In Eq. 2.42, the coincidence counts between D1 and D2 are non-delayed events ($\tau = 0$), whereas the coincidence counts between D1 and D3 are measured at different delay values τ. The delay τ parameter in the nominator is associated with the detections on D1 and either D2 or D3.

In this context, it is important to note that the detection of photons from an SPDC process is often characterized with significant vacuum state occupation due to the non-unity generation efficiency in SPDC process as well as failed detections. For the probability distribution of photons in an unheralded state, the vacuum state has the most significant occupation probability, i.e., P(0). However, using the heralding technique, the occupation probability of the vacuum state is considerably reduced, i.e., $\mathrm{P}^{(h)}(0) \to 0$, and the most significant probability is shifted to the single-photon state, i.e., $\mathrm{P}^{(h)}(1)$. Given that the probability distribution terms sum up to unity for the conditional (heralded) and unconditional (unheralded) detection settings, i.e., $\mathrm{P}^{(h)}(0) + \mathrm{P}^{(h)}(1) + \mathrm{P}^{(h)}(2) + \mathrm{P}^{(h)}(n > 2) = 1$ and $\mathrm{P}(0) + \mathrm{P}(1) + \mathrm{P}(2) + \mathrm{P}(n > 2) = 1$, the following inequality $\mathrm{P}^{(h)}(n) > \mathrm{P}(n)$ thus holds for $n \geq 1$, indicating that the conditional probability of

detecting $n \geq 1$ photons is larger than that of the unconditional detection. This can be observed by comparing the probability distribution of photon number states in **Figure. 11 a** & **b**, where the larger average photon number of the heralded state than that of the unheralded state is demonstrated.

For the calculations of chapter five, it is useful to demonstrate how the relationship between the heralded auto-correlation function $g_h^{(2)}(0)$ and the conditional probability distribution of photon number states denoted by $\mathrm{P}^{(h)}(n)$ can be formulated. Given the definition of average photon-number per pulse for a heralded state, $\langle \hat{n} \rangle = \mathrm{Tr}\{\tilde{\rho}_h^{id}\, \hat{n}\} = \sum_{n=0}^{\infty} n\, \mathrm{P}^{(h)}(n)$, from Eq. 2.34 it follows that $g_h^{(2)}(0)$ function can be expressed as

$$g_h^{(2)}(0) = \frac{\mathrm{Tr}\{\tilde{\rho}_h^{id}\, \hat{n}(\hat{n}-1)\}}{\left(\mathrm{Tr}\{\tilde{\rho}_h^{id}\, \hat{n}\}\right)^2} = \frac{\sum_{n=0}^{\infty} n(n-1)\mathrm{P}^{(h)}(n)}{[\,\sum_{n=0}^{\infty} n\, \mathrm{P}^{(h)}(n)\,]^2} \tag{2.43}$$

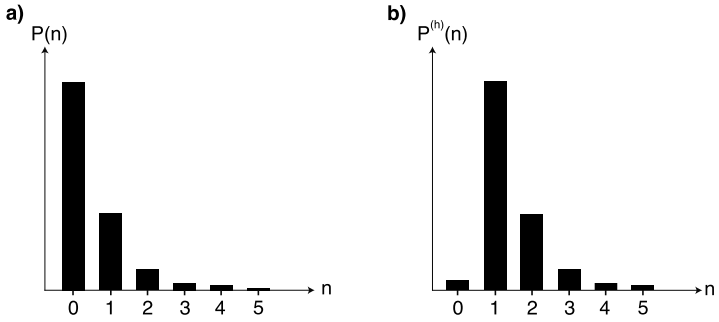

Figure. 11 Photon-number probability distribution for **a)** an unheralded state and a **b)** heralded state from SPDC process.

The normalized density matrix of a heralded state reads $\tilde{\rho}_h^{id} = \sum_{n=0}^{\infty} \mathrm{P}^{(h)}(n)|n\rangle\langle n|$, and $\mathrm{P}^{(h)}(n) = \mathrm{Tr}\{\tilde{\rho}_h^{id}|n\rangle\langle n|\}$ is the conditional probability distribution of photon number states which can also be expressed as $\mathrm{P}^{(h)}(n) = \mathrm{P}(n \cap h)/\mathrm{P}(h)$. In this definition, $\mathrm{P}(n \cap h)$ is the joint probability of detecting *h* number of heralding and *n* number of heralded photons, and $\mathrm{P}(h)$ is the probability of detecting *h* number of heralding photons. It is also important to note that in SPDC process, the probability of detecting a single-photon state in the heralded mode exceeds the probability of detecting two and more

heralded photons ($P^{(h)}(1) \gg P^{(h)}(2) \gg P^{(h)}(n>2)$). In Eq. 2.43, it is thus valid to assume $P^{(h)}(n>1)^2 \to 0$ and simplify the term in the denominator to $\left[\mathrm{P}^{(h)}(1)\right]^2$. For a heralded state created from a pulsed-driven SPDC process, the $g_h^{(2)}(0)$ function in Eq. 2.43 can thus be rewritten as in the following form

$$g_h^{(2)}(0) \approx \frac{2\mathrm{P}^{(h)}(2)}{[\,\mathrm{P}^{(h)}(1)\,]^2} \tag{2.44}$$

In experiment, for $\tau = 0$, an interferometric dip is observed for the heralded auto-correlation function $g_h^{(2)}(\tau = 0)$, whereas the unheralded $g^{(2)}(\tau = 0)$ peaks at $\tau = 0$. It is important to note that in experiments, for values that satisfy the following limit $g_h^{(2)}(0) < 0.5$, the heralded state can be approximated as a high quality (but imperfect) single-photon state.

Noteworthy, the unconditional $g^{(2)}$ function can be assessed using the experimental results from the HBT interferometry in **Figure. 10** and through the following relationship

$$g^{(2)}(0) = \frac{\mathrm{N}_{\mathrm{D2,D3|D1}}(0)}{\mathrm{N}_{\mathrm{D2,D3|D1}}(\tau \neq 0)} \tag{2.45}$$

where $\mathrm{N}_{\mathrm{D2,D3|D1}}$ denotes the delayed ($\tau \neq 0$; denominator) and non-delayed ($\tau = 0$; nominator) conditional two-fold coincidence counts on D2 and D3 triggered by the detections on D1. The unconditional $g^{(2)}$ function is inversely related to the purity of the heralded state and can be quantified through the following equation

$$purity = 1/(\,g^{(2)}(0) - 1) \tag{2.46}$$

which was also used for the measurement of the single frequency mode bandwidth in Sec. 2.11.

2.14. Electro-optic Phase Modulation

Electro-optic phase modulation (EOPM) is a technique used to alter the phase of a light wave by applying an external electric field. The core concept relies on electro-optic effect

where the interaction between an electric field and an electro-optic material, such as $LiNbO_3$, leads to the refractive index change of the material, in turn causing a corresponding change in the phase of the optical carrier and the generation of sidebands at certain offset spectral positions from the frequency of the original optical carrier (ω_0). Electro-optic phase modulation is widely deployed in fibre optic communication systems and quantum optics experiments, where the adjustment of the light phase is crucial to the quantum state manipulation [112].

Suppose a modulator with a half-wave voltage amplitude V_π, driven by an oscillator operating at an angular frequency Ω_m, a modulation voltage amplitude V_m, and a modulation phase θ_m. Periodic modulation generates new frequency components, referred to as sidebands, around the original carrier frequency ω_0 and spaced by integer multiples $r \geq 0$ of the modulation tone Ω, i.e., distributed at spectral positions $\omega_0 \pm r\,\Omega$. By tuning the modulation tone Ω and the modulation voltage amplitude V_m, the total number of the created sidebands, their corresponding amplitudes, and their spectral distance from the original optical carrier becomes adjustable [51,87] .

Consider an input state to the phase modulator from a monochromatic laser beam with angular frequency ω_0 and amplitude A. The input state $Ae^{i\omega_0 t}$ undergoes the following time-dependent transformation, $Ae^{i\omega_0 t + iV_m \sin(2\pi\,\Omega_m t + \theta_m)}$, which according to the Jacobi-Anger expansion, can be expanded by involving the Bessel functions of the first kind, $J_r(m)$. The normalized output state can thus be written as

$$\frac{(J_0(m) + \sum_{r=1}^{\infty} J_r(m)\, e^{ir\theta_m} + \sum_{r=1}^{\infty}(-1)^r J_r(m) e^{-ir\theta_m})}{\sqrt{J_0(m)^2 + 2\sum_{r=1}^{\infty} J_r(m)^2}} \tag{2.47}$$

In Eq. 2.47, the parameter $m = \pi V_m / V_\pi > 0$ is the modulation index. The following relationship $J_{-r}(m) = (-1)^r J_r(m)$ is valid between the positive and negative Bessel functions of the same order r. More detailed, the positive and negative sidebands of the same odd order have a phase difference of π, whereas for even order positive and negative sidebands, a zero phase difference exists. This characteristic of the generated sidebands is deployed in the experiments of this thesis to enable constructive and destructive quantum interference of adjacent frequency modes, required to probe the bosonic and fermionic-like HOM effects. Importantly, in the experimental implementation of the EBQKD in chapter

six, frequency mixing is deployed to perform random projection measurements onto mutually unbiased basis states.

It is important to note that in electro-optic phase modulation, the Bessel functions provide the amplitude of the created sidebands and are proportional to the modulation voltage amplitude, V_m. In **Figure. 12**, the diagram displays the normalized amplitude of Bessel functions calculated at different modulation indices (m).

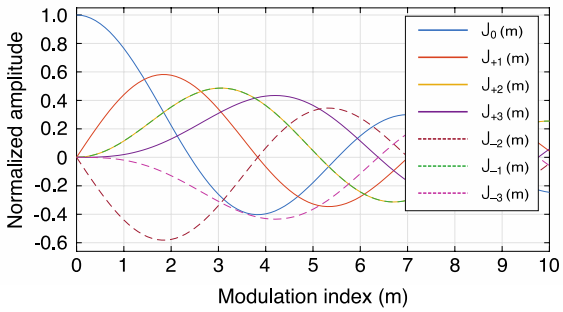

Figure. 12 Normalized amplitude of the Bessel functions $J_{1:3}(m)$ versus the modulation index $m = \pi V_m/V_\pi$.

2.15. Fundamentals of Spectral Broadening by Chromatic Dispersion

In this thesis, frequency-to-time mapping (FTM) technique is implemented using dispersive telecommunication components. In chapter three, this technique is used for the spectral characterization of biphoton states and as part of the experimental steps in chapter six to implement an EBQKD protocol. In this section, the theoretical fundamentals underlying the FTM technique will be briefly reviewed. To this end, temporal broadening of an ultra-fast laser pulse is considered.

Consider a train of laser pulses entering a dispersive medium. The electric field $E_{in}(t)$ of a laser pulse can be considered as a superposition of different spectral components, such that $E_{in}(t) = \frac{1}{\sqrt{2\pi}} \int_{-\infty}^{+\infty} \mathcal{E}(\omega) e^{i\omega t}\, d\omega$. As the pulse propagates through a dispersive medium, every individual spectral component acquires a frequency-dependent phase. The electric-field of the pulse thus evolves into $E_{out}(t) = \frac{1}{\sqrt{2\pi}} \int_{-\infty}^{+\infty} \mathcal{E}(\omega) e^{i(\omega t + \phi(\omega))}\, d\omega$, with an accumulated spectral phase term $\phi(\omega)$. Using the Taylor series, the acquired spectral phase can be expanded around the laser's central frequency ω_0 such that

$$\phi(\omega) = \phi(\omega_0) + \frac{\partial \phi}{\partial \omega}|(\omega - \omega_0) + \frac{1}{2}\frac{\partial^2 \phi}{\partial \omega^2}|(\omega - \omega_0)^2 + \cdots \quad (2.48)$$

$$= \phi^{(0)} + \phi^{(1)}\Delta\omega + \frac{1}{2}\phi^{(2)}(\Delta\omega)^2 + \cdots$$

where $\Delta\omega = \omega - \omega_0$ and $\phi^{(0)}$, $\phi^{(1)}$, and $\phi^{(2)}$ are the zeroth-order, first-order (linear phase or the group delay), and the quadratic (or the group delay dispersion: GDD) spectral phase terms, respectively. The higher-order terms on the right-hand side of Eq. 2.48 are neglected. The phase coefficient $\exp(i\omega t + \phi(\omega))$ is thus expressed as in the following

$$\exp(i\omega t + \phi(\omega)) = \exp\left[i(\omega_0 + \Delta\omega)t + \phi^{(0)} + \phi^{(1)}\Delta\omega + \frac{1}{2}\phi^{(2)}(\Delta\omega)^2\right] \quad (2.49)$$

The second-order phase term $\phi^{(2)}$ is of relevance to the context of this thesis, leading to spectral broadening. For clarity, the effect of this term is considered here independently and in the absence of other phase terms. It is thus assumed that $\phi^{(0)} = \phi^{(1)} = 0$, in which case the phase coefficient in Eq. 2.49 is reduced to

$$\exp(i\omega t + \phi(\omega)) = \exp(i\omega_0 t)\exp(i\Delta\omega t + i\frac{1}{2}\phi^{(2)}(\Delta\omega)^2) \quad (2.50)$$

$$= \exp(i\omega_0 t)\exp(i\Delta\omega(t + \frac{1}{2}\phi^{(2)}\Delta\omega))$$

suggesting a time shift from t to $t + \frac{1}{2}\phi^{(2)}\Delta\omega$ introduced in the time axis of the pulse bandwidth. Noteworthy, the time shift is not uniform throughout the bandwidth and varies for each spectral component dependent on its spectral distance $\Delta\omega$ from the central frequency ω_0. Each spectral component is thus shifted differently in time and the larger the $\Delta\omega$, the more severe the temporal broadening of the pulse bandwidth. The GDD, or the quadratic spectral phase $\phi^{(2)}$, is the source of pulse broadening and is the basis for the FTM technique. The frequency-dependent duration, $T(\omega)$, required for a given spectral component ω to traverse a dispersive medium can be calculated from the following formulation

$$T(\omega) = \text{Group delay} + \text{GDD} \times \Delta\omega \quad (2.51)$$

In Eq. 2.51, the GDD can take positive or negative values. For GDD > 0, the lower frequency components travel at a faster phase velocity than the higher frequency components (normal dispersion resulting in positively-chirped pulse). The opposite holds true for GDD < 0 (anomalous dispersion resulting in negatively-chirped pulse), that is the higher frequency components travel at a faster phase velocity than the lower frequency components. In **Figure 13,** the pulse spectrogram under negative and positive GDD is illustrated.

For a pulsed laser with a Gaussian spectral profile, the temporal width $\Delta\tau$ of the broadened spectrum can be calculated from Eq. 2.52

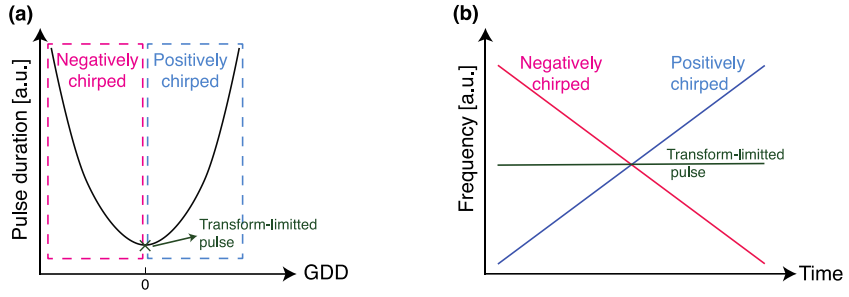

Figure. 13 (a) Pulse duration as function of accumulated quadratic spectral phase (GDD; group delay dispersion). **(b)** Spectrogram as function of time for a positively-chirped (blue), negatively-chirped (red), and transform-limited pulse. For a transform-limited pulse, that is an unchirped pulse, the spectral components travel at an identical phase velocity.

$$\Delta\tau = \tau_0 \sqrt{1 + \left(4\, ln2\, \phi^{(2)}/(\tau_0{}^2)\right)^2} \tag{2.52}$$

where τ_0 is the temporal width of the initially transform-limited Gaussian pulse with its spectral components traveling at an identical phase velocity. In FTM technique, certain amount of dispersion is required to allow for a measurable correspondence and mapping of the optical spectrum onto a time-stretched intensity profile. This is determined by the so-called far-field condition which requires $\left|\phi^{(2)}\right| \gg {\tau_0}^2/_{2\pi}$ where τ_0 is the initial pulse duration [113].

3. FTM-assisted Spectral Characterization of Biphoton States

In this chapter, a novel and time-efficient method is demonstrated to directly and through a single coincidence measurement, characterize the spectral correlations of biphoton states generated in pulsed-driven SPDC process within a PPLN waveguide. In addition, the first-time direct measurement of the second-order auto-correlation function in frequency domain is revealed. For this purpose, the well-established FTM technique is employed which relies on the chromatic dispersion to translate the frequency components of an optical spectrum onto a time-stretched temporal waveform. In this implementation, the frequency components of the biphoton state are temporally resolved post-propagation through a dispersive medium, i.e., a DCF. The fine timing resolution of our single-photon detection system allows for the spectrally-resolved detection and thus the direct frequency-mapping of the biphoton state in time. In particular, this technique enables the spectral characterization of biphoton states without the need to perform time-consuming measurements relying on successive frequency sweeping with expensive filtering devices. Specifically, this is achieved through only a single coincidence measurement over the SPDC biphoton spectrum. Contrary to the hitherto commonly-adopted schemes composed of successive scans over the frequency distribution of the biphoton state, in the presented approach the time-resolved coincidence detections are exploited to reconstruct the signal-idler JSI, to gain access to the CAR, and to directly perform a spectral HBT experiment. Importantly, for the first time, the direct measurement of the dependency of the $g^{(2)}(\Delta\nu)$ function on the frequency spacing $\Delta\nu$ between the spectral components within the biphoton state spectrum is revealed, in contrast to common demonstrations that exhibit the variations of the $g^{(2)}(\tau)$ as function of delay τ between the photons' arrival times at the detectors [107,114–116]. It is important to note that the $g^{(2)}(\Delta\nu)$ function incorporates information regarding the spectral correlations which can be used to determine the single frequency mode bandwidth of the system, whereas the $g^{(2)}(\tau)$ contains information over the temporal correlations and as a result for non-pure states the Fourier transformation does not hold between the two, $\mathcal{F}\{g^{(2)}(\tau)\} \neq g^{(2)}(\Delta\nu)$.

3.1. Experimental Setup for FTM-assisted Spectral Characterization

The experimental setup (see **Figure. 14a**) consisted of a PPLN waveguide (*Covesion*) excited by a 10 µW pulsed laser (50 MHz repetition rate) whose spectral bandwidth was filtered to a FWHM of δ_{pump}= 200 GHz and aligned at the center wavelength of λ_{pump}= 774.8 nm. Through type-0 SPDC processes within the PPLN waveguide, photons of the excitation pulse-train were down-converted into highly time-frequency correlated photon pairs. The frequency distribution of the created photon-pairs spans over a bandwidth of several THz which is determined by the SPDC phase-matching bandwidth. The PPLN was cascaded by a DCF with a GDD = 960 ps/nm and 6.5 dB loss measured for one passage through the fibre which allowed for the formation of a scaled and temporally-resolved replica of the SPDC biphoton spectrum.

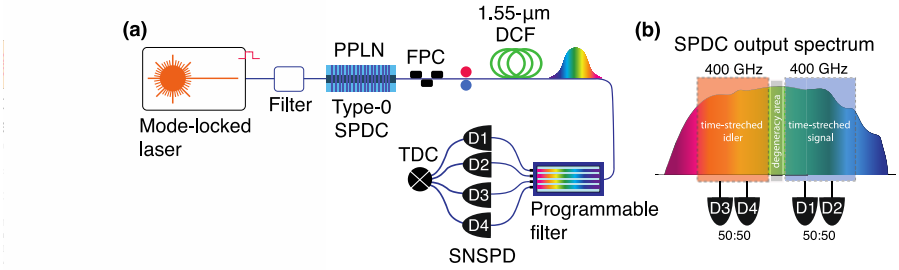

Figure. 14 a) Experimental setup based on the FTM technique employed to characterize the SPDC biphoton spectrum. **b)** Spectral configuration defined with the use of a programmable filter for the characterization of the SPDC biphoton spectrum. (HWP: Half-wave plate; DSM: D-shaped Mirror; PPLN: periodically-poled lithium niobate; FPC: fibre polarization controller; DCF: dispersion compensating fibre)

With the use of a programmable filter (*Finisar waveshaper* 4000S), the SPDC output spectrum was bandpass filtered to $\Delta f_{SPDC} = 800$ GHz bandwidth defined symmetric with respect to the SPDC degeneracy frequency $\upsilon_d = 193.46$ THz (see **Figure. 14b**). The signal (higher frequency) and idler (lower frequency) spectrum with $\Delta f_{signal\,(idler)} = 400$ GHz bandwidth, were each half split to separate ports on the programmble filter and were directed towards the following detectors D1 and D2 and the detectors D3 and D4, respectively. A TDC unit (*Swabian Instruments*; *time-tagger module*) was employed to collect the coincidence detections. In this experiment, the detectors were triggered by the pulsed laser repetition rate. The total integration time for the coincidence measurement was 11 hours.

3.2. FTM in a Dispersion Compensating Fibre

The frequency-to-time mapped replica of the signal and idler spectrum are shown in **Figure 15**. The frequency components within the signal and idler spectrum of $\Delta f_{signal(idler)}$ = 400 GHz bandwidth dispersed through the DCF and created time-resolved detections in synchronization with the pulsed laser repetition rate of 50 MHz, hence over the pulse period of T_{pulse}= 20 ns. By relating the time-scaled replica of ΔT_{scaled} ~ 3300 ps temporal-width to the initial undispersed spectral bandwidth of $\Delta f_{signal(idler)}$ = 400 GHz, a FTM correspondence of C_{FTM}~ 0.1212 GHz/ps was measured for the system, which was in good agreement with GDD = 960 ps/nm of the DCF. Considering the timing resolution t_r = 25 ps of the SNSPDs, the net spectral resolution of ν_r ~ 3.03 GHz was measured for the whole single-photon spectrometer, obtained from the combination of the SNSPD and the DCF.

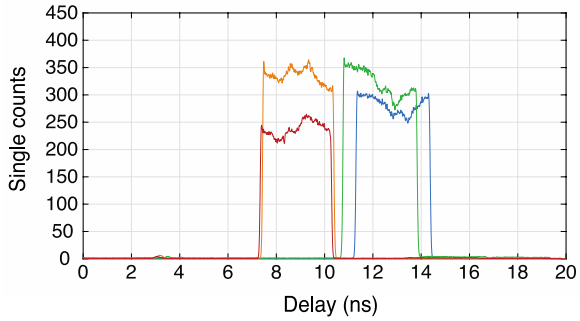

Figure. 15 Time-stretched replica of the signal and idler spectrum. The $\Delta f_{signal(idler)}$ = 400 GHz-bandwidth of the signal and idler spectrum are mapped onto a temporally-scaled intensity profile of ΔT_{scaled} = 3300 ps temporal width, corresponding to a FTM coefficient of C_{FTM}~ 0.1212 GHz/ps. The slight deviation between the intensity profiles can be ascribed to the systems electronics, slight difference in detectors' timing resolution or the optical path lengths, as well as the polarization sensitivity of the SNSPDs. Detections on detectors D1 and D2 (D3 and D4) correspond to the signal (idler) spectrum with higher (lower) frequency. Considering the normal dispersion, the higher-frequency nature of the signal spectrum is reflected in its larger delay in comparison to the idler spectrum. The single counts on each detector are measured over a three-minute integration time.

It is important to note that the frequency resolving capability of ν_r ~ 3.03 GHz that is achieved with the presented FTM-based spectrometer is 29 and 10 times higher than those reported by Avenhaus et. al. [80] and Eckstein et. al. [70], respectively. In these works, the detectors' large timing jitter of 180 ps and 250 ps restricted the achievable spectral resolutions to ~ 89.8 GHz and ~ 28.89 GHz at ~1550 nm wavelength, which to be compensated, required a DCF with longer length and/or with much larger GDD. In

addition, lower pulsed-laser repetition rate was indispensable to obviate the overlapping of adjacent pulses. Importantly, with the presented approach in this thesis, no pulse overlapping is observed.

Noteworthy, to achieve a spectral resolution of 3.03 GHz using a filtering device instead of a DCF, the amount of loss for 400 GHz bandwidth would amount to 10 log (400/3.03) ≈ 20 dB. Given the 4.5 dB insertion loss of a programmable filter, in total 24.5 dB optical loss would accrue. In contrast, using the FTM approach, the DCF introduced only 6.5 dB loss.

Overall, using the infrastructure of better specifications, the FTM-assisted spectral characterization scheme presented here enabled to achieve frequency-resolving capability higher than those previously reported and importantly at the cost of far less optical loss.

3.3. FTM-assisted Measurement of the Second-order Degree of Coherence

The two-fold coincidence events from the time-resolved detections on D1 and D2 allowed to directly measure the spectral second-order auto-correlation function defined as [107]

$$g^{(2)}(\nu_1, \nu_2) = \frac{\langle \hat{a}^\dagger(\nu_1)\, \hat{a}^\dagger(\nu_2)\hat{a}(\nu_2)\hat{a}(\nu_1)\rangle}{\langle \hat{a}^\dagger(\nu_1)\hat{a}(\nu_1)\rangle \langle \hat{a}^\dagger(\nu_2)\hat{a}(\nu_2)\rangle} \tag{3.1}$$

corresponding to the signal field. **Figure. 16a** illustrates the dependency of $g^{(2)}(\nu_1, \nu_2)$ on frequency components ν_1 and ν_2 distributed symmetric with respect to the SPDC degeneracy frequency $\upsilon_d = 193.46$ THz, and starting from $\nu_1 = \nu_2 = 50$ GHz to exclude the coincidence counts originating from the signal-idler frequency correlations. In **Figure. 16b**, the total intra- and inter-pulse coincidence counts as function of the spectral difference $\Delta\nu$ between the frequency components is shown, i.e., $\nu_1 = \nu$ and $\nu_2 = \nu + \Delta\nu$. The intra-pulse events refer to the coincidence detections that have originated from the same pulse, whereas the inter-pulse coincidence events correspond to the detections from different pulses. For the case of intra-pulse events and at zero frequency difference, $\Delta\nu = 0$, an increased number of coincidence detections is observed. The ratio of the intra- to the inter-pulse coincidence counts is measured $g^{(2)}(\Delta\nu = 0) \approx 2.07 \pm 0.06$ (see the inset of **Figure. 16b**). The FWHM at which the peak number of intra-pulse events were collected relates to the single frequency-mode bandwidth. With a Lorentzian fit, the single frequency-mode

bandwidth $\delta\nu = 57.18 \pm 0.94$ GHz could be directly determined. This value was additionally verified in a conventional measurement of the $g^{(2)}(\Delta f)$ as function of the spectral filter bandwidth Δf, i.e., by gradually increasing the spectral filter bandwidth from $\Delta f = 20$ GHz, and by fitting a theoretical model [61] to the experimental data (see **Figure. 16c**).

Under Gaussian profile approximation for an undispersed biphoton state spectrum, the spectral bandwidth of $\Delta f_{signal} = 400$ GHz corresponds to the transform-limited temporal modes of $\delta t \sim 1.1$ ps width. The single frequency mode bandwidth, $\delta\nu = 57.18 \pm 0.94$ GHz, measured via the FTM-assisted approach, corresponds to a photon wave packet of $\Delta\tau \approx 7.7$ ps temporal width (see **Figure. 17 a & b**). In light of $t_r = 25$ ps timing resolution for the singe-photon detectors, the temporal mode corresponding to a single frequency mode bandwidth is thus unresolvable by the employed detection system. This suggests that measuring the dependence of $g^{(2)}(\tau)$ on the temporal coherence, i.e., as function of delay τ between the photons' arrival times at the detectors, yields imprecise values for the single frequency-mode bandwidth. Noteworthy, the frequency resolving capability of $\nu_r \sim 3.03$ GHz obtained in the presented scheme guarantees that the measurement result $\delta\nu = 57.18 \pm 0.94$ GHz for the single frequency-mode bandwidth is reliable.

The direct measurement of $g^{(2)}(\nu)$ as function of frequency ν, i.e., by probing the frequency correlations, which is for the first-time revealed here, thus allows to quantify the single frequency mode bandwidth with much higher precision than through the conventional method of measuring $g^{(2)}(\tau)$ as function of delay τ, i.e., by probing the temporal correlations in biphoton states. This highlights the advantage of the FTM technique for reliable spectral characterization of biphoton states from parametric processes.

3.4. FTM-assisted Characterization of the JSI and the CAR

The FTM technique allows for a direct measurement of the JSI and the CAR of the signal and idler photon pairs from a parametric process. In this experiment, the time-resolved coincidence events corresponding to the signal and idler photon pairs were collected to reconstruct the JSI and to obtain the corresponding CAR. In **Figure. 18a**, the JSI of the signal and idler photon pairs and the corresponding CAR is displayed as function of

symmetric positive and negative frequency offsets from the SPDC degeneracy frequency, i.e., $\upsilon_d = 193.46$ THz for the *Covesion* PPLN waveguide.

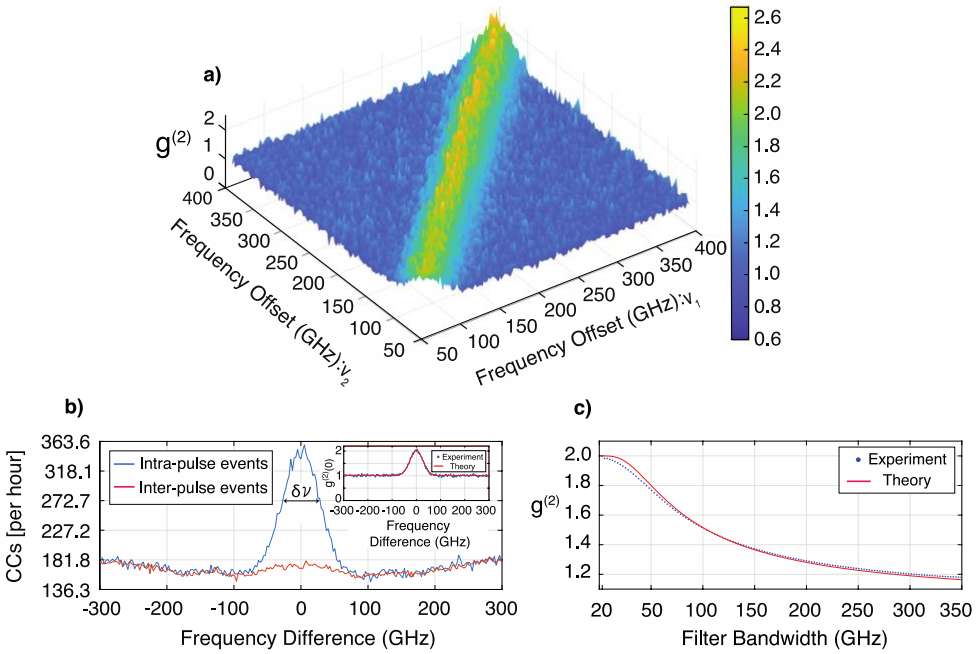

Figure. 16 Spectral second-order degree of auto-correlation $g^{(2)}$ as function of **a)** photons frequency offset ν_1 and ν_2 from the SPDC degeneracy frequency $\upsilon_{\mathrm{d}}^{\mathrm{SPDC}} = 193.46$ THz, and as function of **b)** frequency difference $\Delta\nu$ between the spectral components of the signal spectrum. **c)** Variation of $g^{(2)}(\Delta f)$ as function of the spectral filter bandwidth Δf. In panel (b), the FWHM of $\delta\nu = 57.18 \pm 0.94$ GHz is the single frequency-mode bandwidth of the system (See text for more details).

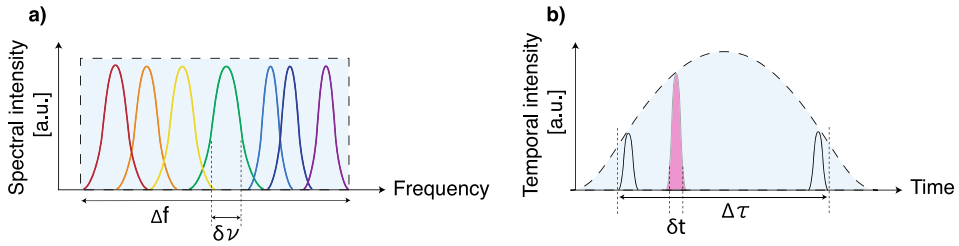

Figure. 17 Schematic illustration of the **a)** spectral profile and its reciprocal **b)** temporal intensity profile under the assumption of propagation through a non-dispersive medium. The undispersed signal spectrum ($\Delta f_{\mathrm{signal}} = 400$ GHz) and the single frequency-mode bandwidth $\delta\nu = 57.18 \pm 0.94$ GHz correspond to a temporal intensity profile of $\Delta\tau = 7.7$ ps width and composed of transform-limited temporal modes with $\delta t = 1.1$ ps temporal width (see main text for more details).

The diagram in **Figure. 18b** illustrates the corresponding total signal & idler intra-pulse and inter-pulse coincidence counts versus the spectral difference between the signal and idler frequency offsets from the SPDC degeneracy frequency. It is observed that at

perfectly symmetric spectral distance from the degeneracy point, i.e., at $\Delta\upsilon = 0$, where the frequency anti-correlations lie, the ratio between the intra- (actual) and inter- (accidental) pulse coincidence counts is ~ 80 (see inset in **Figure. 18b**), equivalent to a signal-to-noise ratio of ~ 19.03dB.

It is important to note that the FTM technique can only be used for the spectral characterization of biphoton states with broad spectra, that is for photon pairs generated from ultra-short pulsed-excited parametric processes. In particular, spectral characterization of photon pairs generated in high Q-factor (Q>1000000) resonators [117] as well as from cw-driven parametric processes are neither feasible with FTM technique nor via the state-of-the-art programmable filters, which is due to the inherently ultra-narrow line-width of the modes which are in the order of kHz. These systems are better characterized directly in the time-domain.

The FTM-assisted approach for spectral characterization of biphoton states from SPDC process was performed for an alternative PPLN waveguide (*AdvR*) with the previous knowledge that the phase matching bandwidth of the *AdvR* PPLN is wider than that of the *Covesion* PPLN waveguide. The same experimental setup illustrated in **Figure. 14a** was employed with an otherwise two instead of four detectors, such that detectors D1 and D2 both monitored the signal and idler spectra. By using two detectors, it was thus feasible to simultaneously reconstruct the strong frequency anti-correlations between the signal and idler photons as well as to obtain the signature of the second-order auto-correlation between the photons of the same (signal or the idler) spectrum (see **Figure. 18c**). In this experiment, the $g^{(2)}(\Delta\nu)$ was measured directly in the frequency domain and based on the results, the single frequency mode bandwidth of the biphoton state was determined to be $\sim$106 GHz. Importantly, this was not directly possible with the conventional characterization techniques relying on the measurement of $g^{(2)}$ (τ) as function of temporal coherence.

3.5. Summary and Conclusion

The conventional experimental scheme for determining the single frequency mode bandwidth of biphoton states from parametric processes involves probing the temporal correlations using the HBT interferometry, i.e., by measuring the second-order degree of coherence as function of delay τ. From $g^{(2)}(\tau = 0) = 2$ it follows that the emission probability of two photons from a single temporal mode is twice the probability of emission

of two photons from two different temporal modes. However, the biphoton states from pulsed-driven parametric processes are characterized with broad spectral bandwidth whose reciprocal is often by more than two orders of magnitude narrower than the timing resolution of the state-of-the-art detection systems, which are thus incapable of properly resolving the single temporal modes.

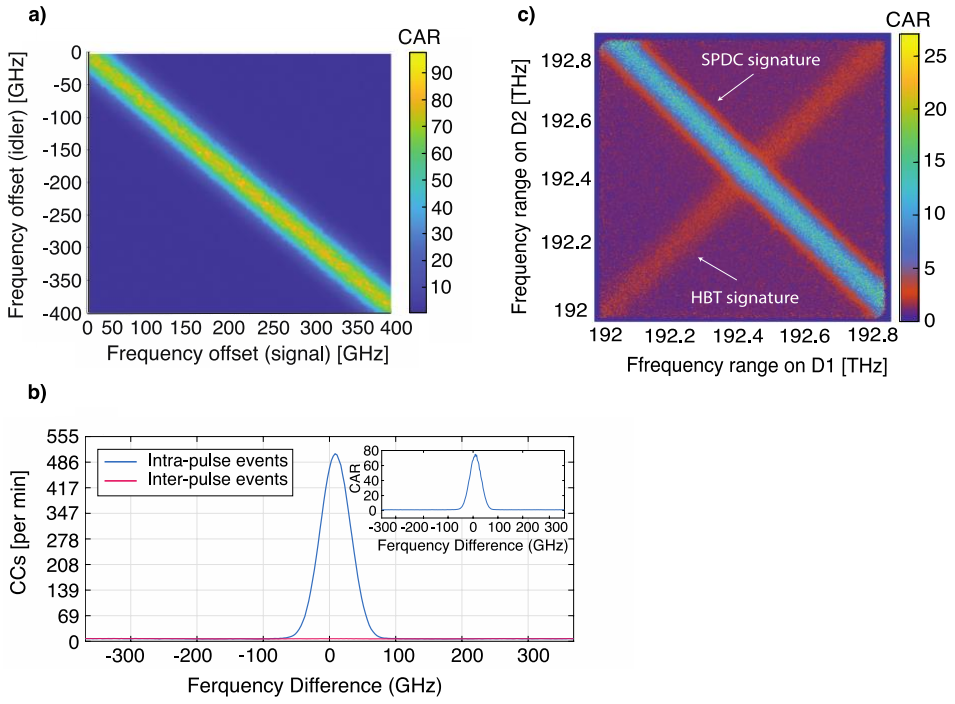

Figure. 18 a) JSI and CAR for the signal and idler photon pairs from SPDC process in a PPLN waveguide (*Covesion*). The results are displayed as function of incremental symmetric signal and idler frequency offsets from the SPDC degeneracy frequency $\upsilon_{\mathrm{d}}^{\mathrm{SPDC}} = 193.46$ THz. **b)** The coincidence counts rate corresponding to the intra-pulse and inter-pulse events versus the spectral difference between the signal and idler frequency offsets from the degeneracy frequency $\upsilon_{\mathrm{d}}^{\mathrm{SPDC}} = 193.46$ THz of the *Covesion* PPLN waveguide. The inset demonstrates the ratio between the intra-pulse (actual) and inter-pulse (accidental) coincidence counts. **c)** Simultaneous reconstruction of the JSI of the signal and idler photons and the auto-correlation signature of the signal or idler photons from SPDC process in *AdvR* PPLN waveguide. By comparing panels **(a)** and **(c)**, the larger phase matching bandwidth of the *AdvR* PPLN than that of the *Covesion* PPLN can be observed.

As a result, by probing the temporal correlations, i.e., $g^{(2)}(\tau)$, the single frequency mode bandwidth can not be determined reliably. Alternatively, measuring the degree of second-order coherence $g^{(2)}(\Delta\mathrm{f})$ as function of variable spectral filter bandwidth $\Delta\mathrm{f}$ could be exploited, where $\Delta\mathrm{f}$ corresponding to $g^{(2)}(\Delta\mathrm{f}) = 2$ is considered equivalent to a single frequency mode bandwidth. However, the frequency resolving capability of highly

elaborate spectral filtering devices often exceeds the single frequency mode bandwidth of biphoton states from ultra-short pulsed-excited parametric processes.

In this research, the first-time direct measurement of the second-order degree of coherence as function of frequency correlations, i.e., $g^{(2)}(\upsilon)$, was revealed using the well-established FTM technique which involves the formation of a time-resolved replica of a given spectral intensity profile. Importantly, the frequency anti-correlations from pulsed-excited SPDC process as well as the spectral auto-correlation signature, were accessible and characterized simultaneously through only a single coincidence measurement. In the presented scheme, a single-photon spectrometer with an FTM correspondence of $C_{FTM} \sim 0.1212$ GHz/ps was achieved through the combined deployment of SNSPDs with a timing resolution of t_r = 25 ps and a DCF of GDD = 960 ps/nm. The presented single-photon spectrometer provided a frequency resolution of $\nu_r \sim 3.03$ GHz which confirms the accuracy of our spectral HBT experiment in determining $\delta\nu = 57.18 \pm 0.94$ GHz as the single frequency-mode bandwidth. As a result, we were able to demonstrate the efficient application of FTM technique for spectral characterization of parametric processes, revealing its potential by making use of elaborate experimental infrastructure that could mitigate the amount of loss in the spectrometer, hence realizing unprecedented frequency resolving capability. In this implementation, higher spectral resolution could be achieved with a longer DCF (or larger GVD values), however, at the cost of more loss and in turn quadratic overhead in integration time.

4. Spectral HOM Effect between Independent Single-photon States

In this chapter, the first-time frequency-domain experimental implementation of the bosonic and fermionic-like HOM effects is demonstrated between independent single-photon states from pulsed-excited SPDC processes. In this implementation, a novel scalable experimental approach is employed that is based on the use of electro-optic phase modulator, a programmable filter, and SNSPDs. The HOM visibilities that are measured fall above the classical limit of 50% offering an appropriate candidate for quantum communication and information processing applications. In addition, the feasibility of switching between the bosonic and fermionic-like HOM effects extends the versatility of this quantum platform, required for the development of quantum networks.

4.1. Concept and the Spectral Configuration

The principal of operation of electro-optic phase modulation, outlined in Sec. 2.14, can be used for the frequency mixing of two or more number of frequency modes. By adjusting the phase modulation settings, perfect spectral overlap between different sidebands can be realized (see **Figure. 19**). This suggests that an electro-optic phase modulator can be considered as a frequency-domain analogue of a conventional spatial-domain beam splitter. This capability is deployed in the experiments of this chapter to realize the HOM interference effect in the frequency domain.

In this context, two photons in two different frequency modes simultaneously (within the reciprocal spectral bandwidth of the biphoton state) arrive at the modulator and mix. Depending on the relative phase of the interacting sidebands being π or 0, the photons bunch either in the same frequency mode which leads to zero coincidence count and in turn an interferometric dip (the bosonic HOM effect) is formed, or each end up in one of the two different frequency modes (anti-bunching phenomenon), resulting in an interferometric peak (the fermionic-like HOM effect). In **Figure. 20**, the spectral configuration and the concept which was followed for the experimental implementation of the frequency-domain bosonic and fermionic-like HOM effects between two independently created photons, is demonstrated.

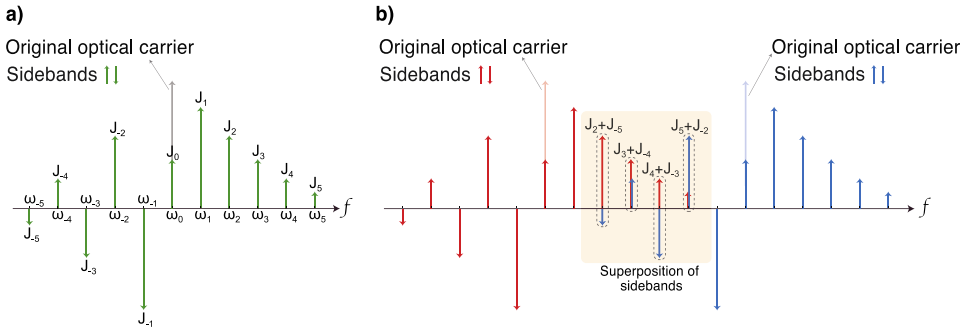

Figure. 19 a) Electro-optic phase modulation of an optical carrier, yielding the generation of five equally spaced sidebands at angular frequencies ω_i with field amplitudes J_i. **b)** An example for the frequency-mixing of two adjacent optical carriers. The dotted squares correspond to the superposition of sidebands.

In this experiment, two SPDC processes from one excitation pulse were considered, producing two signal-idler photon pairs (see Sec. 2.2), with one pair labelled as S1 (green) and I1 (yellow) and the other as S2 (blue) and I2 (red). The following state $|\psi\rangle_{2\mathrm{SPDC}} = \frac{1}{\sqrt{3}}(|1_{\mathrm{I2}}, 1_{\mathrm{I1}}, 1_{\mathrm{S1}}, 1_{\mathrm{S2}}\rangle + |2_{\mathrm{I2}}, 0_{\mathrm{I1}}, 0_{\mathrm{S1}}, 2_{\mathrm{S2}}\rangle + |0_{\mathrm{I2}}, 2_{\mathrm{I1}}, 2_{\mathrm{S1}}, 0_{\mathrm{S2}}\rangle)$ could thus be considered for the generated photon pairs with the first term emerging from two SPDC processes radiating into different frequency modes, and the last two terms describing the emission into the same pair of frequency modes. The detection of photons in S1 and S2 gives access to two independent single-photon states in the corresponding idler frequency modes I1 and I2, respectively. The following state $|\psi\rangle_{2\mathrm{SPDC}}$ is thus projected onto $|\psi\rangle_{\mathrm{in}} = |1_{\mathrm{I1}}, 1_{\mathrm{I2}}\rangle$ as a two-photon input state to the phase modulator. To probe the HOM effect, frequency mixing is applied between the two idler frequency modes in the input state.

4.2. Experimental Setup and Implementation

The experimental setup is presented in **Figure. 21**. A pulsed laser with a centre wavelength of ~775 nm was filtered to a FWHM of ~200 GHz, and coupled into a PPLN waveguide (*Covesion*, type-0 quasi-phase-matched, 40 mm long, 5% MgO-doped). Two pairs of time-energy correlated signal-idler photon pairs were created from two pulsed-driven SPDC processes and around the SPDC degeneracy wavelength of 1549.6 nm. A programmable filter (*Finisar 4000S*) was used to define two pairs of independent signal and idler frequency bins each with a bandwidth of 22 GHz. The programmable filter had a minimum arrangeable bandwidth of ca. 10 GHz, an extinction ratio of 60 dB, and an insertion loss of

4.5 dB. The single detection rate from the frequency bins was approx. 14 kHz measured, which was linearly dependent on the spectral filter bandwidth.

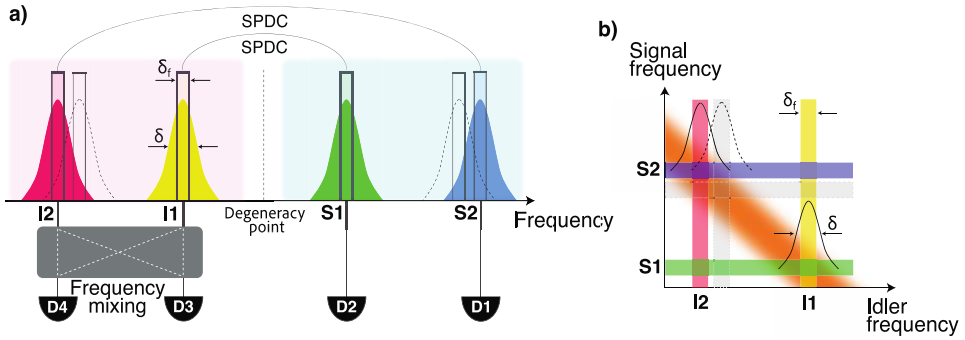

Figure. 20 Spectral configuration defined for the frequency-domain HOM effect between two pure and independently generated single-photons from two SPDC processes. **a)** The single-frequency-mode bandwidth δ of the biphoton states, indicated by colored Gaussian profiles, is accessible with common telecommunication filters. The spectral filters of bandwidth δ_f, represented by rectangular shapes, were employed to define pure signal and idler frequency bins labeled by S1, S2, I1, and I2. The frequency mixing is applied between I1 and I2, and the four-fold coincidence detections on detectors D1, D2, D3, and D4 are collected. The dash-dotted spectral profiles are demonstrated to represent an alternative spectral filter setting for the selection of I1 and S1 which due to the overlap of the spectral profiles would add to the background noise. **b)** Schematic illustration of the JSI of the biphoton states with the corresponding spectral filter positions.

In this experiment, high spectral purity of photons was crucial to obtain high degree of visibility in the HOM effect. The pulsed excitation bandwidth of 200 GHz together with a phase matching bandwidth of ~55 GHz were selected such that photons with high spectral purity could be prepared (confirmed by the HBT experiment presented in Sec. 2.11).

The capability of the programmable filter in defining two coexistent spectral transmission windows allowed to create two single-frequency mode photons within the same spatial mode. The selection of the idler frequency bins requires at its minimum a centre-to-centre frequency spacing of a single frequency mode bandwidth, such that the unwanted background coincidence counts from S1 and I2 as well as from S2 and I1 are suppressed, emerging from off-diagonal spurious spectrally correlated regions (see **Figure. 20b**, the dash-dotted filter settings for I1 and S1). This condition was achieved at 75 GHz (ca. 1.35 times the single mode bandwidth) and 100 GHz (ca. twice the single mode bandwidth) for the bosonic and fermionic cases, respectively.

The two signal photons in S1 and S2 were directed through different ports of the first programmable filter to two SNSPDs, i.e., D2 and D1, respectively. The idler photons were

directed to an electro-optic phase modulator where the frequency mixing was implemented, functioning as a frequency-analogue of a spatial-domain beam splitter [118]. A second programmable filter was employed to direct the photons into frequency bins I1 and I2, monitored by D3 and D4. In this experiment, the electro-optic phase modulator was characterized with an insertion loss of 2.8 dB and was driven by a radio frequency (rf) tone of $\Omega = 25$ GHz (the operation range of the available RF amplifier was within 18-26 GHz). For reference, the two-photon signal-idler coincidence rate in the HOM experiment were 173.5 Hz and 107 Hz measured for the bosonic and fermionic cases, respectively.

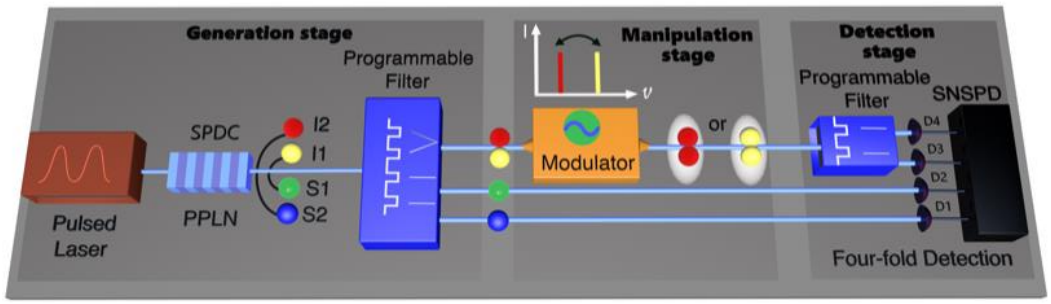

Figure. 21 Schematic illustration of the experimental setup employed for the implementation of the frequency domain HOM effect between two independently generated single-photons (see text for more details).

4.3. Sideband Selection for the Bosonic and Fermionic-like HOM Effects

For the electro-optic phase modulator to realize a frequency-analogue of a balanced spatial-domain beam splitter, the modulation setting should be adapted such that an equal mixing ratio is realized between the fundamental mode (0^{th}-order sideband) and the sidebands of certain order number. In **Figure. 22**, the normalized amplitude of the r^{th}-order sidebands ($r = 0, \pm 3, \pm 4$) as function of different modulation indices is shown. Importantly, to probe the bosonic HOM effect, the signs in the mixing process of the frequency modes are required to differ. Such a sign difference is present when the third-order sidebands are selected for the mixing process, requiring the frequency spacing of the idler frequency bins to be set at 75 GHz. It is observed that at specific modulation indices, the intensity in the fundamental frequency mode equals that of the 3^{rd} order sidebands with a relative π phase difference between $+3$ and -3.

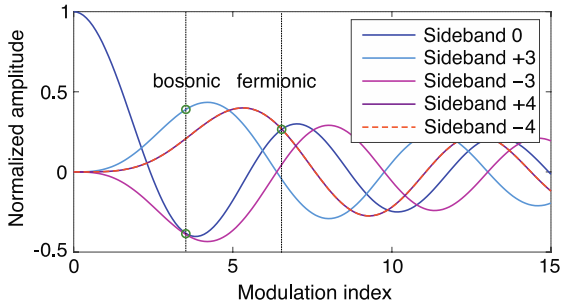

Figure. 22 Simulation of sideband generation in electro-optic phase modulation. The sidebands are expressed as Bessel functions of r^{th}-order ($r = 0, \pm 3, \pm 4$). The left and right black dotted lines, indicate the modulation indices well suited to the experimental requirements for the bosonic and fermionic-like HOM effects, respectively.

The π phase difference between ± 3 sidebands (similar to the phase flip of a spatial beam splitter) leads to the cancelation of transmission and reflection probability amplitudes for a two-photon input state. Here, the transmission probability amplitude refers to the 0^{th} order sideband whereas the reflection probabilities are represented by 3^{rd} order sidebands. This will in turn result in the formation of an interferometric dip, the whole process being the bosonic HOM effect.

In contrast, to realize the fermionic-like HOM effect, the sings in the frequency mixing need to be identical, which can be achieved by choosing the fourth-order sidebands for the mixing process, requiring frequency spacing between the idler frequency bins to be adjusted at 100 GHz. The relative 0 phase difference between ± 4 sidebands leads to the constructive interference between the transmission and reflection probability amplitudes, thereby creating an interferometric peak, representing the fermionic-like HOM interference effect. Note that the sideband creation outside the computational domain can be overcome by e.g., concatenation of phase modulators and programmable filters, where a state transmission of close to 100% can be achieved. **Figure. 23** shows the spectral response of the electro-optic phase modulation applied on classical fields for the bosonic and fermionic-like HOM effect cases.

4.4. Frequency-domain Bosonic and Fermionic-like HOM Effects

Four-fold coincidence measurements were performed for the bosonic and fermionic settings. The pulsed excitation of 20 ns provided the required timing between the two pairs, deployed in the post processing of the coincidence counts. Specifically, the creation of the

two idler photons I1 and I2 in the same excitation pulse led to their simultaneous and thus temporally indistinguishable arrival at the electro-optic phase modulator, in turn leading to the HOM effect (interactive case). In contrast, two idler photons each originating from a different excitation pulse were temporally distinguishable at the splitter and as a result no HOM effect took place (non-interactive cases). In the post processing stage, the four-fold coincidence counts were classified into integer multiples of the pulse period, considered as the time difference between the detection of the idler photons.

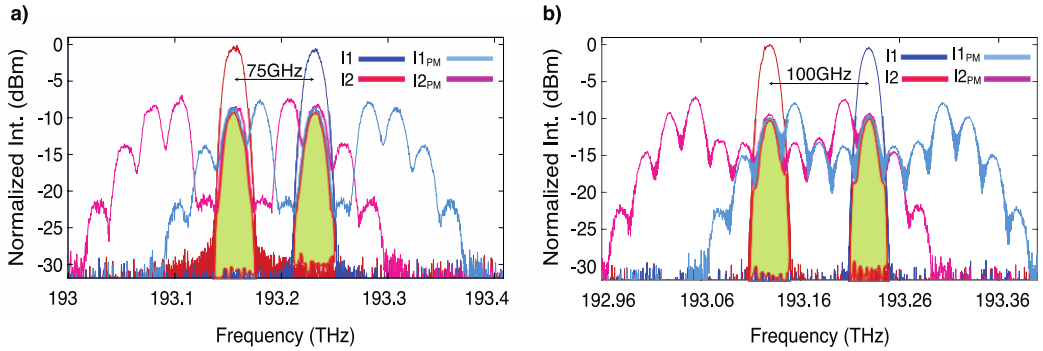

Figure. 23 Classically measured spectrum of the defined idler components before (indicated by I1 and I2) and after phase modulation (indicated by $I1_{PM}$ and $I2_{PM}$): **a)** Bosonic configuration with 75 GHz frequency spacing set between the idler frequency bins, where the phase-modulated 3rd and the 0th order sidebands superimpose, and **b)** Fermionic case with 100 GHz frequency spacing between the idler frequency bins, set to enable the phase-modulated 4th and 0th order sidebands to superimpose. The shaded areas indicate the overlap of the respective sidebands post phase modulation. With an insertion loss of 2.8 dB for the electro-optic phase modulator, a total transmission for the 2-by-2 splitter of 16.64% and 12.26% was measured for the bosonic and fermionic settings, respectively.

Four-fold coincident counts as function of different pulse periods are shown in **Figure. 24 a** & **b** for enabled frequency mixing (modulation enabled) and in **Figure. 24 c** & **d** for disabled frequency mixing (modulation disabled). For the bosonic setting, shown in **Figure. 24a**, a HOM dip with a visibility of $74.31\% \pm 3.57\%$ was observed for active splitting. Here the visibility is determined by $\mathrm{Vis_B} = (\mathrm{CC^B_{max}} - \mathrm{CC^B_{min}})/\mathrm{CC^B_{max}}$ (see Sec. 2.5) where $\mathrm{CC^B_{max}}$ is the average maximum coincidence counts obtained from the non-interactive cases (non-zero delay) and $\mathrm{CC^B_{min}}$ is the minimum coincidence counts resulted from the interactive case (zero delay). For the fermionic setting, displayed in **Figure. 24 b**, a HOM peak with a visibility of $86.44\% \pm 8.27\%$ was obtained, calculated through $\mathrm{Vis_F} = (\mathrm{CC^F_{max}} - \mathrm{CC^F_{min}})/\mathrm{CC^F_{min}}$, with $\mathrm{CC^F_{min}}$ being the average count of the non-interactive cases and $\mathrm{CC^F_{max}}$ the count of the interactive case. By simply turning off the modulator, a

measurement with disabled splitting was performed (see **Figure. 24 c** & **d)**, where no HOM effect was observed, further validating that the previously obtained interferometric dip and peak were due to the frequency mixing and hence the HOM effect.

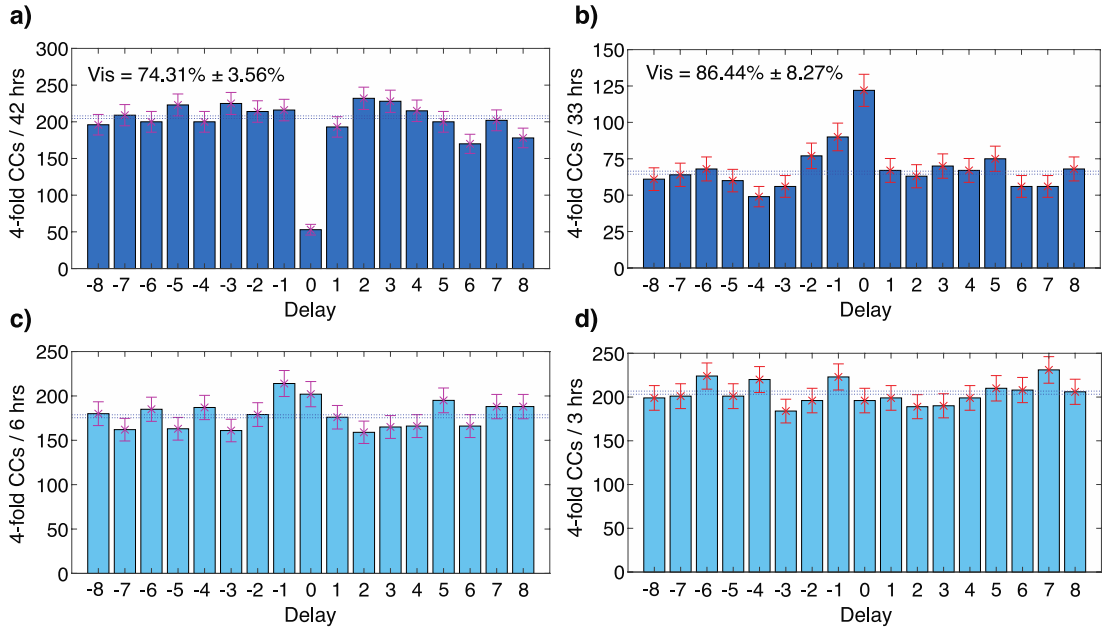

Figure. 24 Post selected four-fold coincidence counts versus pulse delay expressed in terms of multiple integers of the pulse period. Two-photon HOM interference pattern obtained under **a)** bosonic and **b)** fermionic experimental conditions for enabled frequency splitting. The error bars indicate standard deviation (calculated as the square root of the four-photon coincidence counts) corresponding to the integration time of each measurement. For disabled frequency splitting (within an otherwise identical experimental conditions), the coincidence counts versus different pulse periods are shown in panels **c)** and **d)** corresponding to the bosonic and fermionic configurations, respectively. In all four panels, the dotted horizontal lines represent the average counts for the non-interacting cases. The bosonic and fermionic measurements were performed under 160 and 190 µW excitation power, respectively.

It is important to note that in this approach, a characterization of the HOM interferogram in the frequency domain by adjusting the frequency overlap though an RF frequency scan is not implementable as in that case the frequency dependency of the RF amplification affects the splitting ratio of the frequency mixer.

In this experiment, the HOM visibility degrades as a result of experimental imperfections, among which are the spectral profile mismatch between the interacting frequency modes, the unequal spectral splitting ratio of the involved sidebands and the following background terms $|2,0,1,1\rangle_{bg}$ and $|0,2,1,1\rangle_{bg}$, emerging from both spurious correlations and higher-order SPDC emissions (not leading to HOM interference).

In order to have a quantitative estimate over the imperfection contributions, the classical measurements presented in **Figure. 23** were considered, where a 90.96% spectral overlap between the fundamental 0^{th} and the $\pm 3^{rd}$ order sidebands, and 97.75% spectral overlap between the 0^{th} and $\pm 4^{th}$ order sidebands were measured. Furthermore, a 4% deviation from perfect 50:50 frequency mixing ratio was measured for both the bosonic and fermionic cases. As an additional degradation factor, the input state $|\psi\rangle_{\text{in}} = \alpha|1,1,1,1\rangle_{\text{S}} + \beta|2,0,1,1\rangle_{\text{bg}} + \gamma|0,2,1,1\rangle_{\text{bg}}$ was characterized to determine the coefficients (β and γ) of the background terms to the ideal input state (α) by performing the four-fold coincidence detection with no phase modulation applied. For the bosonic setting the following coefficients $\alpha_{\text{B}} = 0.9945$, $\beta_{\text{B}} = 0.0727$, and $\gamma_{\text{B}} = 0.0587$ were measured, whereas for the fermionic setting $\alpha_{\text{F}} = 0.9920$, $\beta_{\text{F}} = 0.0826$, and $\gamma_{\text{F}} = 0.0958$ were obtained. The slightly higher values of the background coefficients in the fermionic case can be explained by higher excitation powers which subsequently led to higher multi-photon generation rates. Considering the background terms, the corresponding degradations in the HOM visibility were 1% and 1.5% for the bosonic and fermionic-like cases, respectively. The sum of the degradation contributions in both cases thus explains the deviation of the measured visibilities from 100%.

4.5. Summary and Conclusion

Here, the first-time frequency-domain implementation of the HOM interference effect between independently created single photon states was demonstrated. A combination of pulsed laser source, reconfigurable electro-optic phase modulator, and programmable filters allowed for a controllable photonic frequency processing circuit, not reported in previous demonstrations of the HOM effect. The HOM visibilities of 74.31%±3.57% and 86.44%±8.27% corresponding to the bosonic and fermionic settings, fell beyond the classical limit, thus applicable to quantum information processing applications. The reconfigurability of the frequency processing setup enabled the bosonic and fermionic-like HOM effects within the same experimental setup which can be used, e.g., for functionality adaptation of quantum logic gates as well as preparing antisymmetric Bell states. This highlights the versatility and potential of the frequency domain approach. Importantly, the results enable the scalability of frequency domain processing to higher numbers of photons, e.g., allowing fundamental Bell-state measurement in the frequency degree-of-freedom.

Larger multi-chromatic multi-photon states can be achieved by defining additional filter functions and adding to the number of single photon detectors.

In this regard, the capability of the electro-optic phase modulator as a frequency mixer can be extended from a 2-by-2 to an N-by-N splitter by considering further sidebands, increasing transmission and giving access to richer photon interactions. To improve the detection rates and the overall performance, the phase modulation process can be optimized by, e.g., the use of more complex modulation functions as well as the concatenation of modulators and the integration of the presented scheme on photonic chips. Our work thus allows for the practical and meaningful frequency-domain implementation of fundamental concepts, such as entanglement swapping, quantum teleportation, the development of novel complex gates, and the creation of frequency-based complex states for quantum metrology applications which are at the basis of future quantum networks. In addition, the feasibility of switching between the bosonic and fermionic-like HOM effects extends the versatility of this quantum platform, hence contributing to the overall scalability.

5. Spectral HOM Effect between a Heralded State and a Thermal Field

In the previous chapter, a scalable realization of the spectral HOM effect between independent single-photon states was demonstrated. The HOM effect underpins the development of measurement-device-independent quantum key distribution protocols, addressing the side-channel security gaps. In particular, the HOM effect is implemented between weak classical states and imperfect single-photon sources, such as heralded states from SPDC process [119–124]. To enable quantum interference, preparing single-mode heralded single-photon states involves eliminating frequency correlations. This introduces thermal characteristics to the state, the impact of which has not been explicitly studied on the HOM visibility.

In this chapter, the experimental implementation of the spectral HOM effect between a thermal field and a heralded single-photon state from a pulsed-excited SPDC process is demonstrated. The impact of multiphoton contamination in imperfect single-photon states on the HOM visibility is revealed for the first time. Importantly, the findings of this research reveal that multiphoton components in a heralded state partially contribute to the quantum interference with the thermal field. This observation, questions the common assumption in literature that multiphoton components in a heralded state exclusively degrade the visibility and that can be subtracted from the total coincidence counts [125]. This study provides fundamental insight into the link between the HOM visibility and photon statistics of the interacting fields, with potential application to ascertaining security in high-speed remote secret key sharing [126].

5.1. Theoretical Derivation of the HOM Visibility

In a pulsed-driven SPDC process with a two-mode squeezer (see **Figure. 25**), a single detection in the signal mode s1 (on detector D3) heralds the existence of at least one photon in the idler mode i1 (on detector D1), resulting in a heralded state in the latter mode. The first- and the second-order moments associated with the heralded state are written as

$$\langle \hat{a}^{\dagger}\hat{a} \rangle_{i1} = \mathrm{Tr}\,\{\hat{a}_{i1}^{\dagger}\hat{a}_{i1}\,\tilde{\rho}_{h}^{i}\} = \bar{n}_{i1,th} + 1, \tag{5.1}$$

$$\langle \hat{a}^{\dagger 2}\hat{a}^{2}\rangle_{i1} = \mathrm{Tr}\,\{\hat{a}_{i1}^{\dagger 2}\,\hat{a}_{i1}^{2}\,\tilde{\rho}_{h}^{i}\} = 2\bar{n}_{i1,th}^{2} + 2\bar{n}_{i1,th},$$

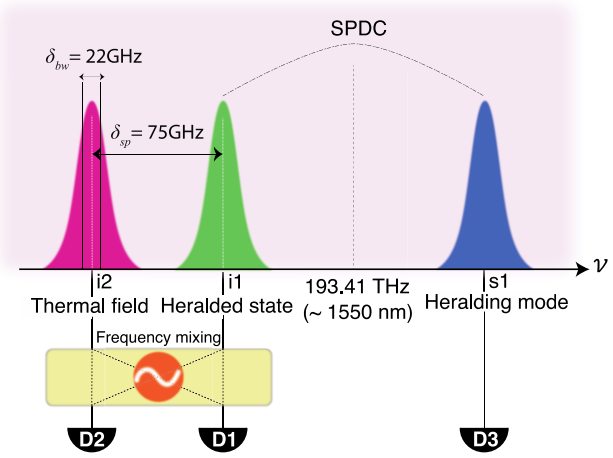

Figure. 25 Spectral configuration of the spectral HOM experiment between a thermal field (i2: red) and a heralded single-photon state (i1: green); Electro-optic phase modulation (frequency mixing) is applied between i1 and i2. (Insertion loss of the modulator: 2.8 dB, δ_{sp} = 75 GHz; δ_{bw} = 22 GHz; rf modulation tone Ω = 25 GHz; rf power amplitude: -10 dB; ν: the frequency axis)

where $\tilde{\rho}_{h}^{i}$ is the normalized density matrix describing the heralded state (see Sec. 2.13.2). The $\hat{a}_{i1}^{\dagger}$ and $\hat{a}_{i1}$ are the photon creation and annihilation operators, respectively, and $\bar{n}_{i1,th}$ represents the average photon number per pulse period within the thermal part of the heralded state, i.e., the multiphoton components. The thermal field is created in the idler frequency mode i2 from an independent SPDC process and by discarding the detections on its twin signal frequency mode. From Eq. 5.1, the second-order correlation between the thermal field and the heralded state is derived as follows (see Sec. 2.8)

$$g_{i1,i2}^{(2)} = 2\overline{n}_{i1,th}^{2} + 2\overline{n}_{i2}^{2} + 2\overline{n}_{i1,th} + 2\overline{n}_{i2}(\overline{n}_{i1,th} + 1)(1 - \delta_{i1,i2}), \qquad (5.2)$$

with $\overline{n}_{i2}$ as the mean photon number per pulse period of the thermal field triggered by detections on s1. The modulation coefficient $\delta_{i1,i2} \in [0,1]$ depends on the fields' degree of indistinguishability, which is partly dependent on the extent of temporal overlap between the interacting photons at the beam splitter. From Eq. 5.2, the following new relationship for the HOM visibility is derived showing its dependency on $\bar{n}_{i1,th}$ and $\overline{n}_{i2}$

$$V_{\text{theory}} = \frac{1}{1 + \frac{\overline{n}_{i1,th}^{2} + \overline{n}_{i2}^{2} + \overline{n}_{i1,th}}{\overline{n}_{i1,th}\,\overline{n}_{i2} + \overline{n}_{i2}}} \tag{5.3}$$

5.2. Experimental Setup and Implementation

The experimental setup (see **Figure. 26**) is composed of a pulsed laser source (*Menlo Systems*) with 50 MHz repetition rate, centred at λ_{pump}= 774.93 nm wavelength, and filtered to a FWHM = 200 GHz. A 40 mm-long, 5% MgO-doped PPLN waveguide (*Covesion*) is used to create time-energy correlated signal-idler photon pairs via SPDC, centred around the degeneracy wavelength λ_{deg}~1550 nm. The spectral configuration (see **Figure. 25**) is defined precisely using a programmable filter (*Finisar Waveshaper 4000S; insertion loss: 4.5 dB*) to guarantee high spectral purity of the photons, that is a single frequency mode bandwidth of approx. 50 GHz (measured in the HBT experiment; see Sec. 2.11**)**.

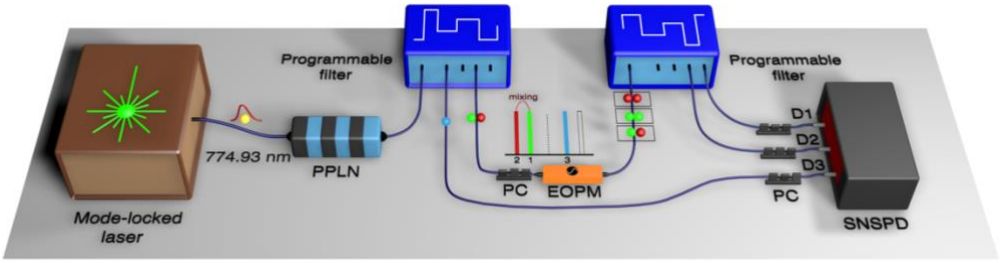

Figure. 26 Experimental setup of the spectral HOM effect between a thermal field and a heralded state. A single excitation photon (yellow) is sent through a PPLN waveguide and decays into pairs of correlated signal-idler photons. The system's spectral configuration is defined at the first programmable filter. The idler photon i1 (green) is heralded by the detection of its twin photon in the signal mode s1 (blue), and the idler mode i2 (red) is detected independently but triggered by detections on s1. Electro-optic phase modulation is applied on the idler modes i1 and i2, and the coincidence detections are collected on detectors D1 (monitoring i1), D2 (monitoring i2), and D3 (monitoring s1) (PC; polarization controller, EOPM; electro-optic phase modulator, SNSPD; superconducting nanowire single photon detector).

Electro-optic phase modulation (*EO Space*) is used to half split the power between the heralded state (i1) and the thermal field (i2) enabling to probe the HOM effect in frequency domain. The sidebands are generated at 25 GHz free spectral range and band-pass filtered to maintain the experiment's spectral configuration. Coincidence events are recorded at

integer multiples of the pulse period (20 ns) via a TDC module (*Swabian instruments; Timetagger Ultra*).

The action of 50:50 beam splitting in frequency is implemented via electro-optic phase modulation between i1 and i2, through which one frequency mode converts into five positive- and negative-order sidebands. Among the total ten side bands, the 0^{th}- and $+3^{rd}$-order side bands for i2 and the 0^{th}- and -3^{rd}-order sidebands for i1 were selected which are of equal amplitudes and are spectrally distanced at δ = 75GHz. For each frequency mode, the power is half-transmitted into the 0^{th}-order side band and half-reflected into the 3^{rd}-order sideband. This leads to the cancelation of the equal-amplitude side bands that feature a π-phase-difference, hence yielding photon-bunching in one of the two output modes of the beam splitter and the realization of the HOM effect. Considering the post selection of two out of multiple sidebands generated in electro-optic phase modulation, the operation of the frequency-domain beam splitter in this HOM experiment is non-unitary. From the single detection rates in the modulation-disabled and modulation-enabled experiments (see **Table. 1**), the effective transmission of the beam splitter was obtained ~33% which corresponds to - 4.75dB operational loss. The coincidence to accidental ratio of CAR ≈ 16 was measured corresponding to the generation in the frequency modes s1-i1.

Table. 1 Single detection rates on detectors D1, D2, and D3.

Experiment	D1	D2	D3
Modulation-disabled	9.38 kHz	10.28 kHz	230.35 kHz
Modulation-enabled	3.28 kHz	3.29 kHz	220.82 kHz

5.3. Experimental Retrieval of the HOM Visibility

The experimental result of the spectral HOM effect is shown in **Figure. 27**. The three-fold coincidence counts are displayed versus delay – expressed as integer multiples of the pulse period ($\Delta t = m \times T$; T = 20 ns; m = 0, ±1, ±2, ...) – between D2 and the heralded detections on D1. In general, the visibility in the HOM effect is probed by contrasting the number of two-photon amplitudes of indistinguishable photons (from two input modes of a beam splitter) that bunch in the output modes, to those of distinguishable photons that emerge as coincidence detections, the latter considered as reference point CC_{ref}. Distinguishability is achievable by introducing non-zero delay values ($\Delta t \neq 0$)

between the photons. In conventional HOM setups [125,127], temporal distinguishability is realized between the two input modes of a beam splitter via an optical delay line.

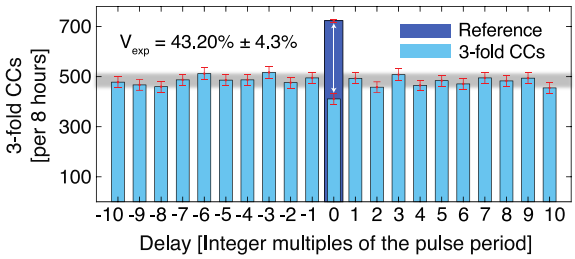

Figure. 27 Results from the spectral HOM experiment between a thermal field and a heralded state: Three-fold coincidence counts as function of delay between detectors D1 and D2 – triggered by single detections on D3. The grey line shows the average number of delayed coincidence counts $CC^{ave}(\Delta t \neq 0) = 484 \pm 22$. The arrow shows the experimental value for the HOM visibility, V_{exp} = 43.2% ± 4.3%, defined as the difference between the reference point, CC_{ref} = 724 ± 45, and the coincidence counts measured at zero delay, $CC(0) = 411 \pm 20$. The error bars show the standard deviation (square root) of the coincidence counts per 8-hour integration time.

Unlike such approaches where the average delayed coincidence counts serve as the reference point $CC_{ref} = CC^{ave}(\Delta t \neq 0)$, the inter-pulse delay principle ($\Delta t = m \times T$; T = 20 ns; m = 0, ±1, ±2, ...) adopted in this experiment necessitates considering additional coincidence counts to determine CC_{ref} (see **Appendix II**). Such enhancement in CCs is associated with the thermal statistics of multiphoton components in the heralded state. Three contributions can be distinguished for the total CCs: The three-fold CCs from photons residing prior to phase modulation in different input modes $CC_{i2,i1|s1}$, from multiphoton components within the thermal field $CC_{i2,i2|s1}$, and from multiphoton components within the heralded state $CC_{i1,i1|s1}$. The reference point is thus written

$$CC_{ref} = A \times CC_{i1,i1|s1}(\Delta t \neq 0) + B \times CC_{i2,i2|s1}(\Delta t \neq 0) + C \times CC_{i2,i1|s1}(\Delta t \neq 0) \quad (5.4)$$

and the HOM visibility V_{exp} can be obtained through

$$V_{exp} = \frac{[CC_{ref} - CC(0)]}{CC_{ref}} \quad (5.5)$$

with CC(0) as the three-fold coincidence counts measured at zero delay ($\Delta t = 0$). On the right-hand side of Eq. 5.4, D1 and D2 detect photons exclusively emitted from i1 (first term), exclusively emitted from i2 (second term), and emitted from i1 and i2 (third term). The enhancement coefficients A = $g^{(2)}_{i1,i1|s1}(0)$ and B = $g^{(2)}_{i2,i2|s1}(0)$, which account for the additional CCs introduced by multiphoton components, are defined as the unconditional second-order auto-correlation functions

$$g^{(2)}_{i1(i2),i1(i2)|s1}(0) = \frac{CC_{i1(i2),i1(i2)|s1}(0)}{CC_{i1(i2),i1(i2)|s1}(\Delta t \neq 0)} \tag{5.6}$$

The enhanced CCs result from high spectral purity and temporal indistinguishability at zero delay, essential for implementing the HOM effect [96,100]. In two separate experiments using the same experimental setup, the following second-order auto-correlation functions A $= g^{(2)}_{i1,i1|s1}(0)$ and B $= g^{(2)}_{i2,i2|s1}(0)$ are measured. In these measurements (see **Figure. 28**), by exclusively allowing the emission from i1 (i2) and s1 to pass through the first programmable filter and blocking the emission into the frequency mode i2 (i1), the unconditional second-order auto-correlation functions A = 1.98 ± 0.1 and B ≈ 2 for the heralded-state in i1 and the thermal field in i2, are measured, respectively, confirming their single frequency-mode nature.

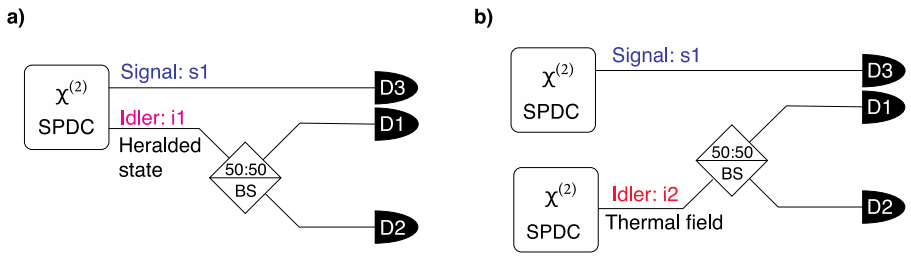

Figure. 28 Conceptual illustration of the three-fold second-order auto-correlation measurements for **a)** the heralded state and **b)** the thermal field. (BS: Beam Splitter).

In this experiment, the contribution from the second term in Eq. 5.4 is found negligible for the delayed and non-delayed events ($CC_{i2,i2|s1}(\Delta t \neq 0) \approx CC_{i2,i2|s1}(\Delta t = 0) \approx 0$) which ascribes to three SPDC processes per pulse. For the last term in Eq. 5.4, C = 1 is obtained, namely, the three-fold coincidence detections from two different input modes i1 and i2, emerge at an identical delayed and non-delayed rate, $CC_{i2,i1|s1}(\Delta t \neq 0) = CC_{i2,i1|s1}(\Delta t =$

0). This stems from the fact that the generation in i1 and i2 emerge from two independent SPDC processes. Since the separation bandwidth between i1 and i2 exceeds the single-mode bandwidth (~50 GHz), i1 and i2 are considered independent spectral modes. As a result, the generation rate of photons in i1 and i2, whether in different pulses or the same pulse, are identical. In this experiment, the average delayed three-fold coincidence counts are measured $\mathrm{CC}^{\mathrm{ave}}(\Delta t \neq 0) = 484 \pm 22$, which consists in the following events: $\mathrm{CC}^{\mathrm{ave}}(\Delta t \neq 0) = \mathrm{CC}^{\mathrm{ave}}_{\mathrm{i1,i1|s1}}(\Delta \mathrm{t} \neq 0) + \mathrm{CC}^{\mathrm{ave}}_{\mathrm{i2,i1|s1}}(\Delta \mathrm{t} \neq 0)$; The contribution of each constituent term can be determined by having access to the generation ratio $\bar{n}_{\mathrm{i1,th}}/\bar{n}_{\mathrm{i2}} \approx 1.02$ (see **Appendix III**) between the mean photon number per pulse period of the thermal part of the heralded state ($\bar{n}_{\mathrm{i1,th}}$) and the thermal field ($\bar{n}_{\mathrm{i2}}$). From this ratio the following terms $\mathrm{CC}^{\mathrm{ave}}_{\mathrm{i1,i1|s1}}(\Delta t \neq 0) \approx 245$ and $\mathrm{CC}^{\mathrm{ave}}_{\mathrm{i2,i1|s1}}(\Delta t \neq 0) \approx 239$ are retrieved. In Eq. 5.4, the reference point $\mathrm{CC}_{\mathrm{ref}} \approx 724 \pm 45$ is thus determined. From the coincidence counts measured at zero delay $\mathrm{CC}(0) = 411 \pm 20$, the experimental value of $\mathrm{V}_{\mathrm{exp}} = 43.2\% \pm 4.3\%$ is calculated for the HOM visibility using Eq. 5.5.

5.4. Validating the Experimental Results

From Eq. 2.42, the heralded auto-correlation function $g_h^{(2)}(0) \approx 0.25$ is measured at zero delay ($\tau = 0$; see **Figure. 29**). For better understanding, the equation is rewritten as follows

$$g_h^{(2)}(0) = \frac{\mathrm{CC}_{\mathrm{D2,D1|D3}}(0) \times \mathrm{N}_{\mathrm{D3}}}{\mathrm{CC}_{\mathrm{D1,D3}}(0) \times \mathrm{CC}_{\mathrm{D2,D3}}(0)} \tag{5.7}$$

where $\mathrm{CC}_{\mathrm{D1,D3}}(0)$, $\mathrm{CC}_{\mathrm{D2,D3}}(0)$ and $\mathrm{CC}_{\mathrm{D2,D1|D3}}(0)$ are the non-delayed two- and three-fold coincidence counts[2]; N_{D3} is the total number of single detections on D3, each of which heralds a corresponding detection on D1. It is important to note that the value of $g_h^{(2)}(0) < 0.5$ indicates that the heralded state can be approximated as a single-photon state.

[2] Note that the indices to the coincidence counts here indicate the corresponding detector used in the measurement as opposed for the relation used for the autocorrelation function.

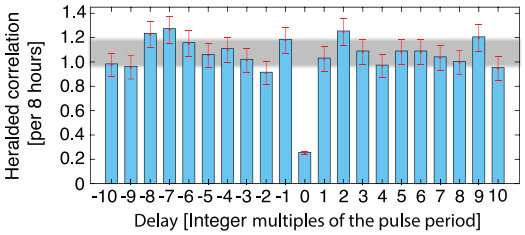

Figure. 29 Heralded correlation function $g_h^{(2)}(\Delta t)$ versus delay between detections on detectors D1 – heralded by single detections on D3 – and D2. At zero delay $g_h^{(2)}(0) \approx 0.25$ was measured. The grey horizontal line is the average value of the delayed heralded correlation function, $g_{h,ave}^{(2)}(\Delta t \neq 0) = 1.07 \pm 0.1$. The error bars show the standard deviation – square-root – of the three-fold coincidence counts corresponding to 8-hour integration time.

The average photon number in the heralded state $\bar{n}_{i1}$ is obtained from the following $\bar{n}_{i1} = \mathrm{Tr}\{\hat{\rho}_{i1}\hat{n}_{i1}\} = \mathrm{P}(1) + 2\mathrm{P}(2)$ where $\hat{n}_{i1}$ is the photon number operator, and $\hat{\rho}_{i1} = \sum_n \mathrm{P}(n)\,|n\rangle\langle n|$ is the density matrix of the heralded state. The experimental system was characterized such that for $n > 2$ the following $\mathrm{P}(n > 2) \approx 0$ could be assumed. In addition, for a heralded state, the occupation probability in the vacuum state reads $\mathrm{P}(0) \approx 0$ (see Sec. 2.13.3). From Eq. 2.44 the following probabilities $\mathrm{P}(1) \approx 0.89$ and $\mathrm{P}(2) \approx 0.1$ were determined, which gave $\bar{n}_{i1} \approx 1.1$. Subtraction of the single-photon contribution from $\bar{n}_{i1}$ gave $\bar{n}_{\mathrm{i1,th}} \approx 0.1$. From the generation ratio $\bar{n}_{i1,th}/\bar{n}_{i2} \approx 1.02$, the average photon number in the thermal field is thus obtained as follows $\bar{n}_{i2} \approx 0.098$. By replacing $\bar{n}_{i1,th}$ and $\bar{n}_{i2}$ in Eq. 5.3, the visibility $\mathrm{V_{theory}} = 47.3\% \pm 0.7\%$ for the HOM effect between the heralded state and the thermal field is calculated, which is in good agreement with the experimental result from the previous section.

5.5. Multiphoton-assisted Partial Improvement in the HOM Visibility

By definition, the HOM effect is considered as a two-photon bunching effect that results from the superposition on a balanced beam splitter of two indistinguishable photons, coming from different input modes of the beam splitter. This definition establishes the presumption of full involvement in the HOM effect – under perfect indistinguishability – for the two-photon amplitudes from i1 and i2, hence leading to zero coincidence counts at zero delay ($\mathrm{CC}_{i2,i1|s1}(0) = 0$). In contrast, the three-fold events from multiphoton components in the heralded state i1 were presumed to remain intact as a result of emerging from two photons in the same frequency mode, i.e., perceived as background terms. On

this account, a minimum predicted value $\mathrm{CC_{pr}}(0) = \mathrm{CC_{i1,i1|s1}}(0) \sim 485 \pm 40$ was foreseen for the non-delayed coincidence counts – considering the enhancement coefficient. However, in experiment, the coincidence counts at zero delay were measured as follows $\mathrm{CC}(0) = 411 \pm 20$, which falls outside the standard deviation range and below the minimum predicted amount of $\mathrm{CC_{pr}}(0)$. Importantly, as conducted in previous works [125], subtraction of $\mathrm{CC}_{i1,i1|s1}(0)$ from $\mathrm{CC}(0)$ – if assumed as background – would lead to negative values, hence proved unphysical. The difference between experiment and initial expectation is explainable by the engagement of the multiphoton components in the heralded state in the HOM effect with the thermal field. This is verified by the theory derived in Eq. 5.1 and illustrated in **Figure. 30** showing the dependency of the HOM visibility on $\bar{n}_{i2}$ and $\bar{n}_{i1,th}$. The dashed arrow shows the conjunction between $\bar{n}_{i2}$ and $\bar{n}_{i1,th}$ from experiment and the corresponding visibility. Under $\bar{n}_{i2} \ll 1$ and for $\bar{n}_{i1,th} = 0$, a visibility of 100% is achievable. For increasing values of $\bar{n}_{i1,th}$, the visibility decreases as a consequence of multiphoton components added to mode i1 (i.e., under the emergence of an imbalance between the thermal mean photon numbers), which leads to coincidence counts at zero-delay, hence a reduction in visibility. However, with increasing $\bar{n}_{i2}$, the imbalance between $\bar{n}_{i1,th}$ and $\bar{n}_{i2}$ is reduced, yielding an improvement in the visibility. The interplay between the thermal fields indicates the engagement of multiphoton components in the heralded state in the quantum interference.

5.6. Quantifying the Degree of Non-classicality of a Heralded State

Our approach allows to determine the non-classicality degree of a heralded state [128] which depends on the average photon number of its multiphoton components. A negative Mandel parameter (QM < 0) is sufficient to classify a field as non-classical [100,129,130]. For a heralded state, the Mandel parameter is defined as follows $\mathrm{Q_M} = (\bar{n}_{i1,th}^2 - 1)/(\bar{n}_{i1,th} + 1)$, from which the following upper bound on the average photon number of its multiphoton components $\bar{n}_{i1,th} < 1$ is derived to realize a non-classical state. This condition corresponds to a lower bound on the peak visibility of the heralded state's HOM effect with a thermal field, such that for the following range of visibilities V > 41.42%, the heralded state can be classified as nonclassical. As depicted in **Figure. 31**, the HOM visibility varies with the average photon number $\bar{n}_{i2}$ of a thermal field. Two cases are presented: the HOM effect between a heralded state and a thermal field (solid curves)

and the HOM effect between two thermal fields (dashed curves). The solid curves follow Eq. 5.3, whereas the dashed curves are based on the formulation of the HOM visibility between two thermal fields (see **Appendix IV**). In case of the HOM effect between two thermal fields, the maximum visibility reaches approximately 33.33%.

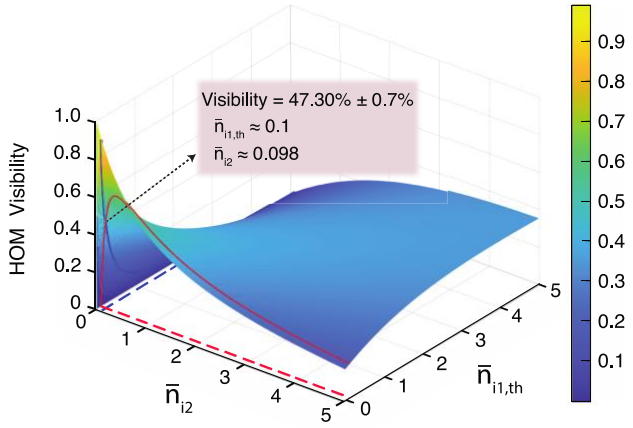

Figure. 30 Visibility of the HOM interference effect between a thermal field and a heralded state, as function of average photon number per pulse period of the thermal field ($\bar{n}_{i2}$) and the thermal part of the heralded state ($\bar{n}_{i1,th}$). The dashed arrow points to the intersection of the experimentally measured mean photon numbers $\bar{n}_{i1,th} \approx 0.1$ and $\bar{n}_{i2} \approx 0.098$, in turn corresponding to the theoretical value of the HOM visibility $V_{theory} \approx 47.3\% \pm 0.7\%$.

5.7. Summary and Conclusion

In this chapter, an experimental implementation of the spectral HOM effect between a heralded state from SPDC process and a thermal field was demonstrated. An experimental approach was presented to retrieve the HOM visibility and a novel theoretical relationship was derived describing the dependency of the HOM visibility on the photon statistics of the interacting states of light. The experiment and theory in this chapter confirmed that multiphoton components partially contribute to the HOM visibility depending on the relative statistics of the interacting states of light. This observation contradicted the common assumption in literature considering the multiphoton contamination as background terms to the HOM visibility.

The validity of our adopted approach for obtaining the HOM visibility is confirmed by applying it to the case of the HOM effect between two thermal fields, where a good agreement between the experimental and theoretical values for the visibility, i.e., $V_{exp} = 28.4\% \pm 3.1\%$ and $V_{theory} \approx 33.32\%$, was obtained (see **Appendix V**), falling

below the upper limit of ~33.33% set for the HOM effect between two thermal fields [131].

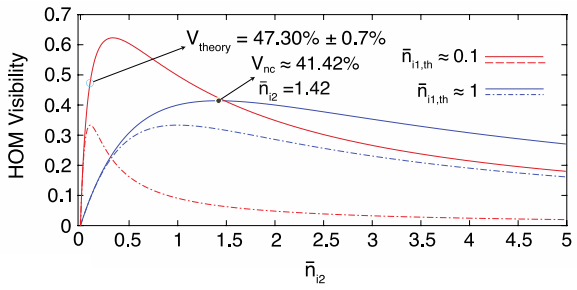

Figure. 31 HOM visibility versus $\bar{n}_{i2}$ for fixed values of $\bar{n}_{i1,th} = 0.1$ and $\bar{n}_{i1,th} = 1$, corresponding to the experimental value and the nonclassicality upper threshold of the multiphoton components in the heralded state. The $V_{theory} \approx 47.3\% \pm 0.7\%$ is our theoretical HOM visibility under $\bar{n}_{1,th} \approx 0.1$ and $\bar{n}_2 \approx 0.098$.

Overall, the results in this experiment provide insight into the HOM effect and propose using controlled higher intensities of heralded states for measurement-device-independent QKD protocols, which can improve the key-rate, speed up the process, and reduce statistical fluctuations in information processing.

It is important to note that in these experiments, photon number resolving detectors could enhance the statistical characterization of the heralded state. However, the limited detection efficiencies of such detectors and their substantial timing jitters, hinder their adoption in quantum photonic labs [132].

6. Frequency-bin-encoded EBQKD

In this chapter, the first-time frequency-bin-encoded implementation of the BBM92 EBQKD protocol paired with a flexible entanglement distribution over long fibre links is demonstrated. A novel frequency-bin-basis analyser module is developed which considerably reduces system complexity and hardware overhead. The functionality of this module is based on the deployment of off-the-shelf telecommunication components such as a programmable filter, an electro-optic phase modulator, a FTM unit, and a SNSPD of high timing resolution. With a fine-tuned frequency mixing, the presented scheme allows for performing passive frequency-bin projection measurements in two mutually unbiased basis, realizing a random basis choice as a fundamental security condition in QKD protocols [84,85]. Importantly, the projection measurements in two mutually unbiased basis and for multiple quantum channels are performed simultaneously using a single measurement apparatus, i.e., an electro optic phase modulator. In this implementation, direct frequency-to-time mapping of quantum channels paired with pulsed excitation provides each user with a simultaneous access to the projection measurement results corresponding to four basis states, using only a single SNSPD. Remarkably, it will be demonstrated that the projection states corresponding to multiple quantum channels are detectable using the same single detector.

6.1. Concept and Experimental Implementation

The experimental setup for the frequency-bin-encoded implementation of the BBM92 protocol is illustrated in **Figure. 32a**. The entangled photon-pair source is composed of a 40 mm-long 5%-MgO-doped PPLN waveguide (*Covesion Ltd.*) excited by a pulsed laser with 180 μW input power (*C-Fibre 780 Femtosecond Erbium laser by Menlo systems*), 50 MHz repetition rate, and 10 ps pulse duration. The laser beam is spectrally filtered to a FWHM of 200 GHz via a 4f-configuration optical setup (see **Figure. 32b**) which consists in a half-wave plate (to adjust the incoming polarization of the laser beam for maximum conversion efficiency), a ruled optical grating, a coated bi-convex lens with a focal length of F = 100, and an adjustable mechanical slit to centre the laser wavelength at the PPLN's phase matching wavelength (774.82 nm).

Highly time-energy correlated photon pairs are generated from pulsed-driven SPDC processes within the PPLN waveguide, creating a broad-band biphoton spectrum with a symmetric distribution around the SPDC degeneracy frequency f_d^{SPDC}=193.46 THz (1549.6 nm). A temperature controller (*Covesion OC3*) is used to maintain the PPLN's temperature at the phase matching point (43.4°C) to enable photon-pair generation with maximum efficiency at the SPDC degeneracy wavelength. The photon-pair source is followed by a central programmable wavelength switch (PWS; *Finisar 4000S*; 4.8 dB insertion loss) separating the propagation path of the higher- (signal) and lower- (idler) energy photons to two users, conventionally named Alice and Bob, respectively.

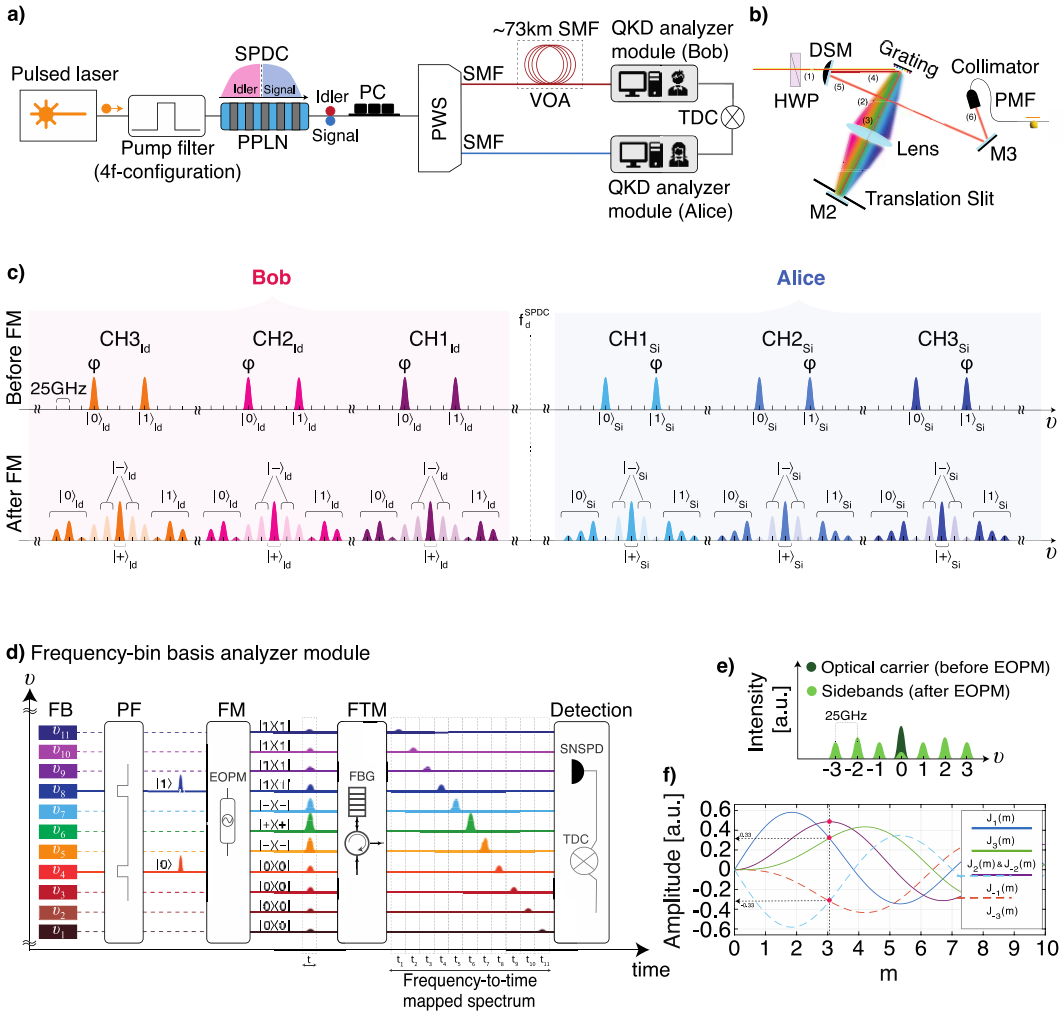

Figure. 32 a) Experimental setup used for the implementation of the BBM92 QKD protocol. **b)** Schematic of the 4f-configuration optical setup employed to spectrally filter the pulsed laser beam to a FWHM of 200 GHz centred at 774.82 nm Wavelength. The numbers in the figure show the propagation direction of the laser beam. Note that the reflected beam from the Grating denoted by (4) is parallel and underneath the incoming beam denoted by (1). **c)** Spectral configuration of the BBM92 protocol before and after frequency mixing. The spectrum is created from an SPDC source which spans around the degeneracy frequency f_d^{SPDC}

= 193.46 THz. Alice and Bob are allocated with the signal (Si) and idler (Id) spectra, respectively. **d)** Frequency-bin basis analyser module. The projection measurements using the operators of the Z and X basis are displayed in the frequency mixing stage. The dotted and solid lines represent the uninvolved and involved spectral positions in each stage, respectively (t: time axis, υ: frequency axis). The FTM unit projects the phase-modulated spectral bins from the common temporal mode t (realized by the pump pulse) to the distinct temporal modes ranging from t_1 to t_{11}, corresponding to frequency bins υ_{11} to υ_1 under negative dispersion, enabling a time-resolved detection of the frequency-mixed spectrum. In this basis analyser module, the insertion loss of the components was as follows, PWS: 4.80 dB, PF: 4.8 dB, $EOPM_{Alice}$: 2.98 dB, $EOPM_{Bob}$: 3.91 dB, FBG_{Alice}: 2.80 dB, FBG_{Bob}: 2.23 dB. **e)** Schematic illustration of electro-optic phase modulation of a single frequency mode, creating up to three sidebands where the $\pm 1^{st}$ and $\mp 3^{rd}$ order sidebands have equal amplitudes. **f)** Simulation of sideband generation using Bessel functions: Sideband amplitudes $J_{\pm 1:3}(m)$ versus modulation index m. The dotted vertical black line shows the modulation index m at which $J_{\pm 1}(m)$ and $J_{\mp 3}(m)$ are generated at a maximum identical amplitude. (PPLN: periodically-poled lithium niobate; SPDC: spontaneous parametric down conversion; PC: polarization controller; PWS: programmable wavelength switch; SMF: single mode fibre; VOA: variable optical attenuator; HWP: half-wave plate; DSM: D-shaped mirror; M: mirror; PMF: polarization maintaining fibre; FB: frequency bins; PF: programmable filter; FM: frequency mixing; EOPM: electro optic phase modulation; FTM: frequency-to-time mapping; FBG: fiber Bragg grating; SNSPD: superconducting nanowire single photon detector; TDC. Time-to-digital convertor)

The PWS served to define the spectral channels on the signal and idler spectrum (CH_{si} and CH_{id}; see **Figure. 32c:** before FM) with 300 GHz frequency spacing and symmetric with respect to the SPDC degeneracy frequency 193.46 THz. Each channel was composed of two frequency bins, labelled $|0\rangle$ and $|1\rangle$ with 20 GHz bandwidth and separated by 100 GHz frequency spacing. The spectral configuration of channels was defined by taking into account the single frequency mode bandwidth of $\sim$ 50 GHz, determined in a second-order autocorrelation measurement (see Sec. 2.11). The symmetric signal and idler pairs of frequency bins were time-energy correlated with their exact spectral positions determined through correlation measurements. The state amplitude of $|0\rangle$ and $|1\rangle$ were prepared equal to provide a maximally entangled state. To demonstrate scalability, three channels were multiplexed, namely CH1, CH2, and CH3, into the single-mode fiber of each user. The channels were separated by 300 GHz frequency spacing on the signal and idler spectrum, respectively. The idler and signal frequency bins in each channel were defined at the following centre frequencies: $CH1_{id}$: 192.36, 192.46, $CH1_{Si}$: 194.46, 194.56, $CH2_{id}$: 191.96, 192.06, $CH2_{Si}$:194.86, 194.96, $CH3_{id}$: 191.56, 191.66, $CH3_{Si}$: 195.26, 195.36 THz. It is important to note that in this experiment, the operation range of the available

programmable filter (191.250 to 196.275 THz; specified by the manufacturer *Finisar* 4000S) allowed for the definition of three frequency channels. A spectral filtering device providing a wider selection bandwidth would enable the definition of additional signal and idler frequency channels further apart from the SPDC degeneracy point. Given the specific definition of the frequency bins in each channel shown in **Figure. 32c**, the frequency-bin entangled states can be defined as follows

$$|\Psi\rangle^{\mathrm{CH1}} = \frac{1}{\sqrt{2}}\left(|0;t\rangle_{\mathrm{si}}^{\mathrm{CH1}}|1;t\rangle_{\mathrm{id}}^{\mathrm{CH1}} + |1;t\rangle_{\mathrm{si}}^{\mathrm{CH1}}|0;t\rangle_{\mathrm{id}}^{\mathrm{CH1}}\right) \tag{6.1}$$

$$|\Psi\rangle^{\mathrm{CH2}} = \frac{1}{\sqrt{2}}\left(|0;t\rangle_{\mathrm{si}}^{\mathrm{CH2}}|1;t\rangle_{\mathrm{id}}^{\mathrm{CH2}} + |1;t\rangle_{\mathrm{si}}^{\mathrm{CH2}}|0;t\rangle_{\mathrm{id}}^{\mathrm{CH2}}\right)$$

$$|\Psi\rangle^{\mathrm{CH3}} = \frac{1}{\sqrt{2}}\left(|0;t\rangle_{\mathrm{si}}^{\mathrm{CH3}}|1;t\rangle_{\mathrm{id}}^{\mathrm{CH3}} + |1;t\rangle_{\mathrm{si}}^{\mathrm{CH3}}|0;t\rangle_{\mathrm{id}}^{\mathrm{CH3}}\right)$$

where *t* denotes the common temporal mode (defined by the excitation pulse) for the signal and idler frequency bins for all quantum channels. In this experiment, the brightness of the SPDC source was characterized as 5.6×10^5 pairs/sec/mW. Under 180 uW input power, the photon pair detection rate for channels CH1, CH2, and CH3 were measured ~ 695, ~796, and ~ 433 pairs/min, corresponding to ~3860 pairs/min/mW, ~ 4422 pairs/min/mW, and ~2405 pairs/min/mW, respectively. The coincidence to accidental ratio for channels CH1, CH2, and CH3, were obtained ~ 46, ~ 48, and ~ 50, respectively, signifying the high quality of the time-energy correlated photon pair source. A variable optical attenuator was employed to exert incremental optical attenuation corresponding to the optical loss experienced at different lengths of a single-mode fiber placed in Bob's arm (see **Table. 2**), hence creating an asymmetric optical fiber link between the users.

To implement the BBM92 QKD protocol (see **Appendix VI**), a novel frequency-bin basis analyser module (see **Figure. 32d**) was developed. Alice and Bob were each equipped with one such module, composed of a programmable filter, an electro-optic phase modulator, a FTM component, and a single SNSPD followed by a TDC module.

In general, the BBM92 protocol requires the users to individually perform projection measurements on their received photons by randomly selecting among two mutually unbiased basis [84,133], here Z = $\{|0\rangle, |1\rangle\}$ and X = $\{|+\rangle, |-\rangle\}$ (where $|+\rangle = 1/\sqrt{2}\,(|0\rangle + |1\rangle)$ and $|-\rangle = 1/\sqrt{2}\,(|0\rangle - |1\rangle)$). In the presented approach, the random

choice between the Z and X basis and the corresponding projection measurements using the following operators $\{|0\rangle\langle 0|, |1\rangle\langle 1|, |+\rangle\langle +|, |-\rangle\langle -|\}$ were realized in the frequency mixing stage.

Table. 2 Optical Attenuation and the Corresponding Optical Fiber Length.

Optical attenuation (dB)	1.64	3.71	5.73	7.98	15.60
Optical fiber length (km)	7.65	17.31	26.66	37.14	73.06

For simplicity, the operation of the basis analyser module is explained for one given channel. In this module, the programmable filter is configured for each user to let pass the photons of the specified frequency bins with an equal intensity. For clarity, the spectral computational space is identified for a given channel on the signal/idler spectrum with υ_1, ... , υ_{11} with the input frequency bins $|0\rangle$ and $|1\rangle$ residing in υ_4 and υ_8, respectively (see **Figure. 32d**).

In this experiment, Bob and Alice owned an electro-optic phase modulator, driven by an RF signal provided by a common arbitrary waveform generator (*Keysight*, M8196A). Electro-optic phase modulation leads to the generation of sidebands around the original optical carrier at integer multiples of the modulation frequency, here Ω = 25 GHz. The modulation voltage amplitude was fine-tuned to enable the generation of maximum three positive and negative order sidebands (see **Figure. 32e**). This configuration led to the superposition of $|0\rangle$ and $|1\rangle$ on the spectral positions υ_5, υ_6 and υ_7.

To experimentally realize the projection measurement onto the $|+\rangle$ and $|-\rangle$ states, in these spectral positions, a specific amplitude and phase relationship between the sidebands were required (see **Figure. 32c**; after FM). The projection onto $|+\rangle$ was realized in the spectral position υ_6, where the positive and negative second-order sidebands superimpose with an intrinsic equal amplitude and a relative phase difference of 0 (even-order sidebands have an intrinsic phase factor of 0). Projections onto $|-\rangle$ were realized in υ_5 and υ_7, where the first- and third-order sidebands superimpose with a relative phase difference of π (negative odd-order sidebands have an intrinsic phase factor of π). In this realization, it was required to have the first and third-order sidebands $\mathrm{J}_{1,3}(\mathrm{m})$ generated at equal amplitudes. By simulating the sideband generation in electro-optic phase modulation using the Bessel functions (see **Figure. 32e**), an optimal modulation RF voltage amplitude was extracted, where this condition is met, i.e., for a specific modulation index *m*, the following equality

$|J_{\pm 1}(m)| = |J_{\mp 3}(m)|$ is realized. Remarkably, at this modulation index almost maximal amplitude for the second-order sidebands were as well obtained, such that efficient projections onto $|+\rangle$ and $|-\rangle$ were simultaneously feasible for each user. It was verified that the sum of the superposition of sideband amplitudes in υ_5 and υ_7 are with good approximation equal to the superposition of sideband amplitudes in υ_6, realizing equal probability for projections on $|+\rangle$ or $|-\rangle$. Furthermore, an extent of sideband generation limited to three, renders the spectral regions υ_1 to υ_4 and υ_8 to υ_{11} devoid of any superpositions. These spectral regions thus represent the projection measurements in the Z basis, realized via the following operators $|0\rangle\langle 0|$ and $|1\rangle\langle 1|$, respectively (see **Figure. 32c**; after FM). Due to the symmetry in the sideband generation, the probability amplitudes for projections onto $|0\rangle$ and $|1\rangle$ states were equal. Importantly, the sum of the probability amplitudes of the states in the Z basis yield nearly identical value to that of the X basis, ensuring that projection measurements in the two mutually unbiased basis occur randomly. In this approach, the phase modulation thus projects a single-photon randomly to either the spectral region corresponding to the X basis or to that of the Z basis, hence realizing a stable, passive and random implementation of the projection measurements. The explained concept can be extended to additional frequency channels, hence enabling scalability.

To measure the frequency-mixed single-photon spectrum directly with a single SNSPD (labelled D1 and D2 for Bob and Alice, respectively), the frequency-bins υ_1, ..., υ_{11} were resolved in time by implementing the FTM technique using a fiber Bragg grating as a dispersive component. In this experiment, the timing reference between the users is realized using the trigger signal from the common pulsed laser source, captured via the TDC module. By exploiting the pulsed laser signal as a time reference in post processing, the time-resolved spectral components of the single photons became accessible using only a single detector. Given the fine timing jitter of the SNSPD (~25 ps), the dispersion in the fiber Bragg grating was precisely selected so as to enable time-resolved detection of adjacent 25-GHz frequency bins. The fiber Bragg grating possessed by Alice and Bob featured negative and positive second-order dispersion values of $\pm$0.0568 ps/nm^2/km, respectively, support a wavelength range from 1528 nm to 1565 nm, and introduce a maximum insertion loss of 2.80 dB and 2.23 dB, respectively. By this detection technique, each user is granted simultaneous access to the projection measurement results in all four basis states $\{|0\rangle, |1\rangle, |+\rangle, |-\rangle\}$ using only a single detector, hence a considerably reduced resource overhead compared to conventional schemes requiring four detectors. In this

approach, the basis analyser module is capable of multiplexing several frequency channels without suffering hardware overhead. A determining factor for the number of frequency channels that could be resolved is the repetition rate of the pulsed laser. In this case, given the 300 GHz spectral distance between adjacent frequency channels, the T = 20 ns pulse period combined with the dispersion introduced by the fiber Bragg grating, it was possible to demultiplex three frequency channels CH1, CH2, CH3 for each user (see **Figure. 33**).
In this experiment, the SNSPDs feature 100 Hz dark count rate and have approx. a timing jitter of 25 ps. The detectors were operating in free running mode. However, in post-processing, the FWHM of the detection windows were considered, corresponding to four projection states, so as to exclude the contributions from adjacent sidebands. The specific definition of detection windows introduces a photon gating loss which was quantified for Alice and Bob's channels separately, shown in **Table. 3**. The values in this table indicate that a wider detection window could be considered to obtain higher key rates.

6.1.1. Projection Measurements via Electro-optic Phase Modulation

In electro-optic phase modulation an arbitrary waveform generator (*Keysight*, M8196A) was employed to drive the modulators. The RF signals from channels 1 and 2 of the arbitrary waveform generator were precisely adjusted at 415 mV and 240 mV voltage amplitudes to drive the electro-optic phase modulators in possession by Bob and Alice, respectively. The modulators possessed by Bob and Alice introduced an insertion loss of 3.91 dB and 2.98 dB, respectively.
Noteworthy, in this experiment, the modulators were required to be phase-stable to maintain the phase relationship for the projections onto the X basis states. In this experiment, the electro-optic phase modulators were intrinsically phase-stable as they were referenced to the same oscillator within the arbitrary waveform generator. In practical scenarios where the users reside in their independent laboratories, the transmission of the RF signal over an optical fiber can be implemented to achieve phase stability.

Table. 3 Gating loss corresponding to detection windows.

Detector	CH1	CH2	CH3
D1 (Bob)	36.34%	31.63%	31.19%
D2 (Alice)	30.35%	30.49%	29.45%

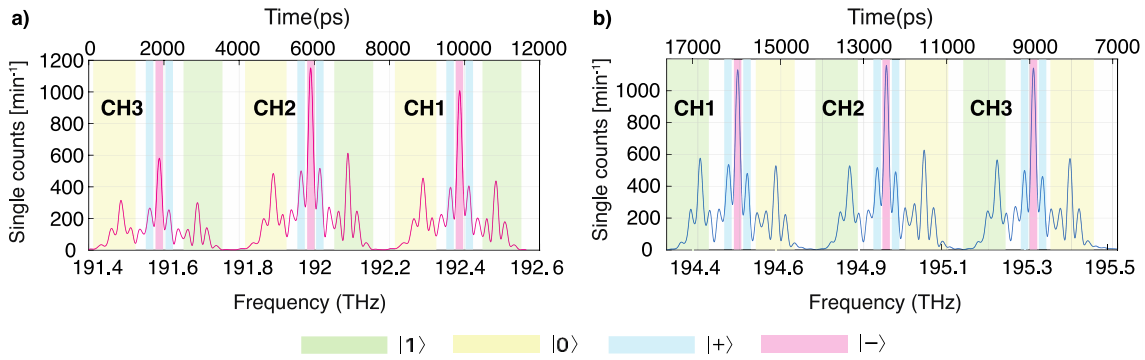

Figure. 33 Frequency-to-time mapped spectral profiles of three frequency channels, namely CH1, CH2, and CH3 after frequency mixing, detected by the detectors **a)** D1 (owned by Bob) and **b)** D2 (owned by Alice). The coloured green, yellow, red and blue spectral regions correspond to the projections onto the states $|1\rangle$, $|0\rangle$, $|+\rangle$, and $|-\rangle$, respectively.

6.1.2. Coherence Stability of Frequency-bin States

The coherence stability of the frequency-bin states is examined under propagation through an optical fiber link of 25 km length cascaded by a dispersion compensating module. In this experiment, the frequency-mixed single-photon spectrum was measured for two cases of 'without' and 'with' 25 km fiber link plus a dispersion compensating module, shown in **Figure. 34 a(b) & c(d)**, respectively. By comparing the results, it is observed that dispersion is compensated over the whole spectrum and that the profile shape of the frequency-mixed spectrum is not distorted. Specifically, the frequency-to-time mapped profiles with 122 ± 5 ps and 2517 ± 20 ps temporal widths (corresponding to ~25 GHz and ~325 GHz bandwidths, respectively) are maintained after propagation through the fiber link cascaded by a dispersion compensating module. Moreover, given the 30-minute measurement time, the impact of the second-order dispersion-induced fluctuations on the spectral profile were measured negligible. The measurement results confirm the stability with respect to the reference signal obtained from the pulsed laser source.

In addition, the similarity of the spectral profile before and after transmission through 25 km fiber link signifies that the equivalence between the optical attenuation and the actual optical fiber link is a valid assumption in this experiment. Specifically, for the propagation of single photons through long optical fiber links, non-linear noise, such as e.g., Raman scattering, is not observed.

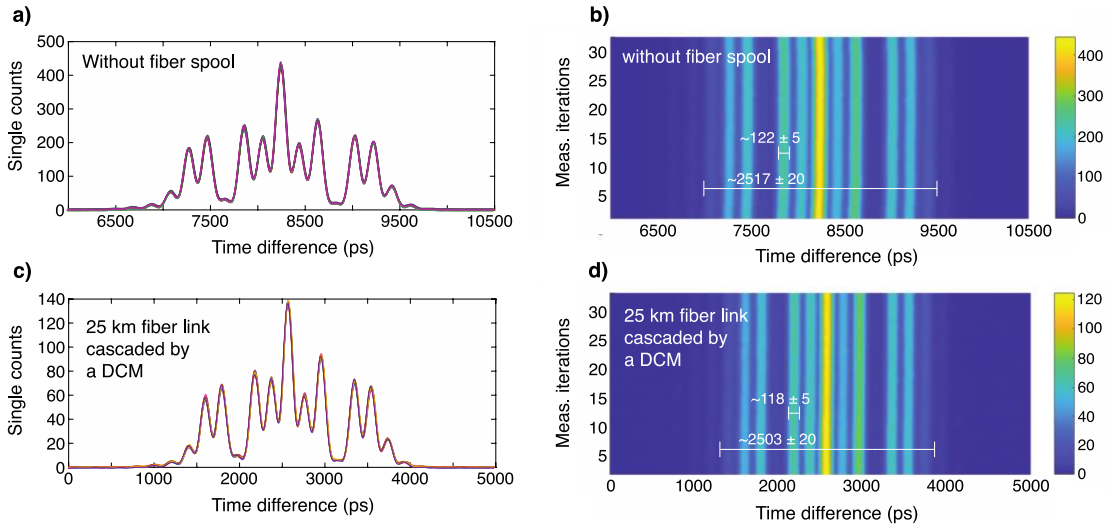

Figure. 34 Time-stretched frequency-mixed spectrum of an arbitrary frequency channel for **(a)** & **(b)** without and **(c)** & **(d)** with a 25 km optical fiber link cascaded by a dispersion compensating module. The experimental results were obtained for 30 iterations of a measurement with 60 seconds integration time. (DCM: dispersion compensating module)

To further assess the coherence stability of the frequency-bin states after propagation through the 25km-long optical fiber link cascaded by a dispersion compensating module, a one-hour coincidence measurement is performed for the phase-modulated signal/idler field at a fixed phase value. The normalized coincidence counts versus measurement time are shown in **Figure. 35**, revealing an almost flat response over time, which demonstrates phase stability for the basis state projection measurements within the thermally controlled laboratory environment. The slight deviation from a perfect phase stable result can be ascribed to slight environmental fluctuations changing the relative photon arrival time with respect to the RF signal.

In practical scenarios, the presented approach can be adapted to address the larger environmental fluctuations in longer optical fiber lengths. In such cases, by employing a common transmission mode technique using RF signal over optical fiber, the phase instability can be mitigated. In this case, the common transmission mode of the RF tone and the photons' electric-field allows for their simultaneous accumulation of phase drifts, leading to a stable two-photon interference over time and thus stable projection measurements.

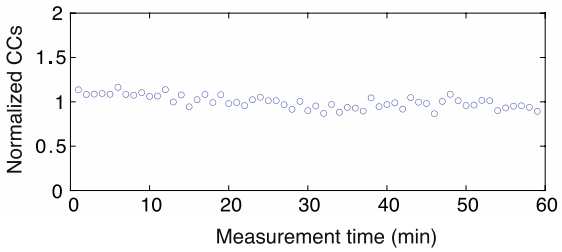

Figure. 35 Coincidence counts measured at an arbitrary fixed phase value versus measurement time. The results are normalized to the average 560 coincidence counts collected per minute.

6.1.3. Polarization Stability

In this experiment, the operation of electro-optic phase modulator is polarization-dependent. A polarization-mismatch between the propagating photons and the optical axis of the electro-optic phase modulator would lead to photon loss and in turn a decrease in the detection rate. However, this case does not lead to a rotation of the qubit's Bloch sphere coordinate system (as it would be the case for polarization encoding), since the qubits in our experiment are defined in the frequency space.

In our experiment, the single detection rates from the signal spectrum were characterized (see **Table 4**), suggesting that polarization was stable at different steps of the experiment (identified by incremental optical attenuation applied on Bob's arm).

Table. 4 Single detection rates on D2 (Alice) at different steps of the experiment.

Single detection rates on D2 (Alice)						
CH1	12.22 kHz	12.74 kHz	12.27 kHz	12.32 kHz	12.81 kHz	13.16 kHz
CH2	12.52 kHz	13.50 kHz	13.31 kHz	13.33 kHz	13.31 kHz	13.50 kHz
CH3	12.15 kHz	11.69 kHz	11.77 kHz	11.63 kHz	11.46 kHz	11.60Hz

6.2. Raw Key Rate Performance Metrics

With the presented novel frequency-bin basis analyser, a frequency-bin-encoded BBM92 protocol (see **Appendix VI**) is implemented. The raw key bits in the Z and X basis were obtained from the coincidence events between D1 and D2 and by identifying the spectral regions associated with the projections $|00\rangle, |11\rangle, |01\rangle, |10\rangle, |{+}{+}\rangle, |{-}{-}\rangle, |{+}{-}\rangle, |{-}{+}\rangle$. The raw coincidence counts in the Z and X basis, $\mathrm{CC}_{\mathrm{Z(X)}}^{\mathrm{raw}}$, consist of the true and accidental counts, i.e., $\mathrm{CC}_{\mathrm{Z(X)}}^{\mathrm{True}}$ and $\mathrm{CC}_{\mathrm{Z(X)}}^{\mathrm{Acc}}$, such that $\mathrm{CC}_{\mathrm{Z(X)}}^{\mathrm{raw}} = \mathrm{CC}_{\mathrm{Z(X)}}^{\mathrm{Acc}} + \mathrm{CC}_{\mathrm{Z(X)}}^{\mathrm{True}}$. The true and accidental counts are defined as $\mathrm{CC}_{\mathrm{Z}}^{\mathrm{Acc}} = \mathrm{CC}_{00} + \mathrm{CC}_{11}$, $\mathrm{CC}_{\mathrm{X}}^{\mathrm{Acc}} = \mathrm{CC}_{+-} + \mathrm{CC}_{-+}$, $\mathrm{CC}_{\mathrm{Z}}^{\mathrm{True}} =$

$CC_{01} + CC_{10}$, and $CC_X^{True} = CC_{++} + CC_{--}$. The coincidence events were collected over an integration time of $\tau = 1560$ s. The coincidence counts averaged over time in each basis are referred to as the raw key rates, i.e., $R_Z = CC_Z^{raw}/\tau$ and $R_X = CC_X^{raw}/\tau$. The ratio between the accidental and the raw coincidence counts in the Z and X basis is termed quantum bit error ratio (QBER) and is denoted by $E_Z = CC_Z^{Acc}/CC_Z^{raw}$ and $E_X = CC_X^{Acc}/CC_X^{raw}$, respectively. In **Table 5**, the experimentally obtained QKD performance metrics for the BBM92 protocol are presented for channels CH1, CH2, and CH3 at different optical attenuations corresponding to different fiber lengths. At 15.6 dB of optical attenuation, corresponding to ~73km fiber length, the QBER remained for all frequency channels well below the 11% upper bound for a secure QKD protocol [134], guaranteeing the security of the protocol.

6.2.1. Minimization of the QBER

In this experiment, electro-optic phase modulation was tuned to provide power radiation into sidebands of maximum 3rd-order. However, a slight amount of power also radiates into the higher-order sidebands, leading to slight increase in the erroneous projections for the Z basis. Specifically, in post processing, the QBER corresponding to the Z basis was obtained on average between ~5.2% to ~6.3%, whereas for the X basis, the QBER was obtained roughly within the range from ~2.5% to ~3.5%. The larger QBER of the Z basis has raised the average QBER to roughly ~4% (see **Table. 5**). To minimize the QBER, the detection window for the Z basis states could be defined from the second-order sideband. Alternatively, by tuning the RF signal waveform, the sideband creation could be controlled such that the generation of higher order sidebands are better suppressed.

6.2.2. Theoretical Modelling of the Raw Key Rate and the QBER

For an EBQKD with a pulsed laser source, the Eq. 6.2 & 6.3 are valid for the raw key rate per pulse period ($Q_{Z(X)}$) and the QBER denoted by $E_{Z(X)}$ in the Z and X basis [135,136]

$$Q_{Z(X)} = 1 - \frac{(1 - D_{Z(X)}^{A})}{(1 + \eta_A \frac{\mu_{Z(X)}}{2})^2} - \frac{(1 - D_{Z(X)}^{B})}{(1 + \eta_B \frac{\mu_{Z(X)}}{2})^2} + \frac{(1 - D_{Z(X)}^{A})(1 - D_{Z(X)}^{B})}{(1 + \eta_A \frac{\mu_{Z(X)}}{2} + \eta_B \frac{\mu_{Z(X)}}{2} - \eta_A \eta_B \frac{\mu_{Z(X)}}{2})^2} \quad (6.2)$$

Table. 5 Performance metrics of the frequency-bin-encoded BBM92 QKD protocol at different lengths of the optical fiber, prior to error reconciliation and privacy amplification. The results correspond to a measurement integration time of τ =1560 s. RCC: raw coincidence counts; ACC: accidental coincidence counts; RKR: raw key rate (per second); QBER: qubit error ratio.

	Optical attenuation (dB) [corresponding fiber length (km)]					
	0 [0]	1.64 [7]	3.71 [17]	5.73 [26]	7.98 [37]	15.6 [73]
CH1						
RCC	25431	18952	12248	7334	4033	652
ACC	1034	759	513	323	158	29
RKR	16.30 ± 0.07	12.14 ± 0.08	7.85 ± 0.07	4.70 ± 0.05	2.58 ± 0.04	0.41 ± 0.01
QBER (%)	4.12 ± 0.18	4.05 ± 0.15	4.19 ± 0.19	4.40 ± 0.25	3.92 ± 0.32	4.45 ± 0.85
CH2						
RCC	34603	24571	14464	9513	5504	922
ACC	1797	1198	647	473	273	60
RKR	22.18 ± 0.17	15.75 ± 0.09	9.27 ± 0.07	6.09 ± 0.05	3.52 ± 0.04	0.59 ± 0.01
QBER (%)	5.20 ± 0.17	4.88 ± 0.14	4.47 ± 0.18	4.97 ± 0.23	4.96 ± 0.32	6.51 ± 0.86
CH3						
RCC	19485	11941	7322	4490	2937	453
ACC	836	525	315	226	142	28
RKR	12.49 ± 0.06	7.65 ± 0.07	4.69 ± 0.05	2.88 ± 0.04	1.88 ± 0.03	0.29 ± 0.01
QBER (%)	4.25 ± 0.21	4.40 ± 0.19	4.30 ± 0.25	5.03 ± 0.34	4.83 ± 0.41	6.18 ± 1.17

$$E_{Z(X)} = e_0 - \frac{2(e_0 - e^{d}_{Z(X)})\,\eta_A\eta_B\frac{\mu_{Z(X)}}{2}(1+\frac{\mu_{Z(X)}}{2})}{Q_{Z(X)}(1+\eta_A\frac{\mu_{Z(X)}}{2})(1+\eta_B\frac{\mu_{Z(X)}}{2})(1+\eta_A\frac{\mu_{Z(X)}}{2}+\eta_B\frac{\mu_{Z(X)}}{2}-\eta_A\eta_B\frac{\mu_{Z(X)}}{2})} \quad (6.3)$$

In Eq. 6.2, the following dark count rates $D^A_Z \approx D^B_Z \approx 0.143\times10^{-6}(\text{sec}^{-1})$ and $D^A_X \approx D^B_X \approx 0.033\times10^{-6}(\text{sec}^{-1})$ were calculated within the 1430 ps and 330 ps coincidence windows of the Z and X basis, respectively, with A and B denoting Alice and Bob. In this implementation, Alice and Bob encounter fixed amounts of -10.58 dB and -10.94 dB loss on their optical paths, respectively. These amounts were resulted from -2.98 dB and -3.91 dB insertion loss from the modulators, - 4.8 dB insertion loss from the programmable

filters, and - 2.80 and - 2.23 dB loss from the fiber Bragg gratings, for Alice and Bob, respectively. For calculating the overall transmittance of Alice and Bob channels, $\eta_A = 0.07$ and $\eta_B = 0.0644$, the detectors' intrinsic efficiencies (~0.8) and the optical loss were considered. Given the incremental optical attenuation on Bob's arm, the overall transmittance for Bob degrades at different optical attenuations, whereas for Alice the amount of loss persists at all lengths of the optical fiber link. In Eq. 6.3, $e_0 = 0.5$ is the error probability, $e^d_{Z(X)}$ is the intrinsic detection error probability arising from the experimental system, and $\mu_{Z(X)}$ is the average photon number per pulse period in the Z and X basis. In **Table 6**, the calculation results for $\mu_{Z(X)}$ and $e^d_{Z(X)}$ are presented for CH1, CH2, and CH3.

Table. 6 Average photon number per pulse period $\mu_{Z(X)}$ and the system detection error probability $e^d_{Z(X)}$ in the Z and X basis.

	CH1	**CH2**	**CH3**
e^d_Z	0.052	0.060	0.049
e^d_X	0.030	0.039	0.036
μ_Z	3.54×10^{-5}	5.29×10^{-5}	2.91×10^{-5}
μ_X	3.76×10^{-5}	4.89×10^{-5}	2.61×10^{-5}

6.3. Asymptotic and Finite Secret Key Analysis

The secret key rate and length are calculated for the asymptotic and non-asymptotic (finite) regimes. The asymptotic regime assumes an infinite number of signals to be exchanged between Alice and Bob. Following the Shor-Preskill security proof for an ideal QKD protocol [137,138], the asymptotic maximum length ℓ^A_Z of the final secret key could be calculated in the Z basis from the following equation

$$\ell^A_Z = n_Z(1 - H_2(E_X)) - \text{leak}_{EC} \tag{6.4}$$

Here, $H_2(e) = -e\log_2(e) - (1-e)\log_2(1-e)$ denotes the binary entropy function, $\text{leak}_{EC} = n_Z\, f_e H_2(E_Z)$ accounts for the number of raw key bits in the Z basis used for error correction, and $f_e \geq 1$ is the error correction inefficiency parameter. Here, the following $f_e = 1$ is considered as the Shannon limit for a given error correcting code. In Eq. 6.4,

$H_2(E_X)$ represents the lower bound for the fraction of the raw key bits that are lost during privacy amplification. The same applies for the asymptotic maximum secret key length in the X basis, ℓ_X^A. The total secret key length in the asymptotic regime reads $\ell^A = \ell_Z^A + \ell_X^A$. In the Z basis, the asymptotic secret key rate is computed through the following formulations

$$S_Z^A = R_Z(1 - H_2(E_X)) - \frac{1}{\tau}\text{leak}_{EC} \tag{6.5}$$

The same applies to the asymptotic secret key rate in the X basis, S_X^A. The total secret key rate in the asymptotic limit is obtained from $S^A = S_Z^A + S_X^A$. From the raw key bits (see **Table. 5**) the asymptotic secret key rate S^A was quantified, shown in the diagram of **Figure. 36**. The theoretical calculations predicted a positive non-zero asymptotic secret key rate for up to ~233 km. For the ~73 km fiber link, a maximum asymptotic secret key length of $l^{A,max} = 310$-bits, $l^{A,max} = 283$-bits and $l^{A,max} = 149$-bits are calculated for channels CH1, CH2, and CH3, respectively.

In the non-asymptotic regime, a finite number of signals are considered to be exchanged between Alice and Bob. In practice, the statistical fluctuations introduced by the finite key size effect, combined with failure probabilities in performing error correcting codes, impede the establishment of perfectly secure and correct key bits. Here, it is assumed that our protocol is correct and secret up to failure probabilities of $\varepsilon_{cor} = 10^{-10}$ and $\varepsilon_{sec} = 10^{-10}$, respectively. (It is important to note that the source-independent nature of the EBQKD protocols renders the inefficiencies in the source irrelevant for the secret key analysis). Additionally, the asymmetry in the implementation of the protocol, arising from unavoidable experimental imperfections, was accounted for. Specifically, an asymmetry in the detection probability in our experimental implementation arises from the different modulation efficiencies in sideband generation, different quantum channels and in turn different amounts of loss, the specific selection of detection windows for post-selecting the coincidence events in the Z and X basis, as well as the slight difference in the intrinsic efficiencies of the detectors. In **Table 7**, maximum detection probability mismatch (δ) between the states in the Z basis and the states in the X basis is presented for frequency channels CH1, CH2, and CH3.

In this implementation, such deviations (from an ideal protocol) were accounted for by adapting the amount of privacy amplification [139].

Table. 7 Maximum detection probability mismatch δ in the Z and X basis.

Basis	CH1	CH2	CH3
Z	1.72%	6.3%	0.7%
X	2.24%	3.41%	3.66%

Additionally, the detection probability mismatch between the Z and X basis is accounted for by performing the secret key analysis for each basis independently. In our finite secret key analysis in the Z basis, the finite secret key length $\ell_{\mathrm{Z}}^{\mathrm{F}}$ is quantified from the following formulation

$$\ell_Z^F = n_{\mathrm{Z}}(1 - \mathrm{H}_2(\frac{\mathrm{E}_{\mathrm{X}} + \alpha}{1 - \Delta})) - \mathrm{leak}_{\mathrm{EC}} - n_{\mathrm{Z}}\Delta - \log(\frac{2}{\varepsilon_{\mathrm{cor}}\varepsilon_{\mathrm{sec}}{}^2}) \tag{6.6}$$

In Eq. 6.6, the following term $\Delta = 1 - 1/(1+\delta)^2$ accounts for the maximum fraction of the key bits in the Z basis removed in privacy amplification to counteract the sources of detection probability mismatch. The parameter α accounts for the statistical fluctuations associated with the finite key size effect and is obtained from the following formulation $\alpha = \sqrt{(n_{\mathrm{Z}}+1)\log\,(\frac{1}{\varepsilon_{\mathrm{sec}}})/2n_{\mathrm{X}}(n_{\mathrm{Z}}+n_{\mathrm{X}})}$. The same applies for the finite secret key length in the X basis, $\ell_{\mathrm{X}}^{\mathrm{F}}$. The total finite secret key length is obtained from the following $\ell^{\mathrm{F}} = \ell_{\mathrm{Z}}^{\mathrm{F}} + \ell_{\mathrm{X}}^{\mathrm{F}}$. The finite secret key rate is thus computed from the following relationship $\mathrm{S}_{\mathrm{Z(X)}}^{\mathrm{F}} = \ell_{\mathrm{Z(X)}}^{\mathrm{F}}/\tau$ and the total finite secret key rate of the protocol is obtained collectively from the finite secret key rates in the Z and X basis, such that $\mathrm{S}^{\mathrm{F}} = \mathrm{S}_{\mathrm{Z}}^{\mathrm{F}} + \mathrm{S}_{\mathrm{X}}^{\mathrm{F}}$ (see **Figure. 36** and **Table 8**).

The finite secret key analysis provided a positive non-zero secret key rate of up to approximately a fiber length of 73 km. At ~15.6 dB optical attenuation (equivalent to ~73 km optical fiber length) the finite secret key rate for CH1 has a positive value, whereas for CH2 and CH3 the finite secret key analysis resulted in negative values and thus no secret key could be extracted. This can be explained by the larger overall detection mismatch for channels CH2 and CH3 compared to CH1 (see **Table 7**), requiring larger amount of raw key bits to be sacrificed for privacy amplification.

6.4. Frequency-based Entanglement Distribution

In this experiment, the SPDC source produces biphoton frequency-bin entangled states. To assess the entanglement quality supported by each channel, Bell-test measurements at zero optical attenuation were performed. In this measurement, Bob and Alice user their programmable filters to impart an identical phase term φ on their frequency bins $|0\rangle$ and $|1\rangle$, respectively. By sweeping the phase term from $\varphi = 0$ to 2π, we performed projection measurements onto the following vector states $|\Psi\rangle_{\mathrm{DD}} = \frac{1}{2}\,(e^{i\varphi}|0\rangle_{\mathrm{Id}} + |1\rangle_{\mathrm{Id}})\otimes(|0\rangle_{\mathrm{Si}} + e^{i\varphi}|1\rangle_{\mathrm{Si}})$, $|\Psi\rangle_{\mathrm{AA}} = \frac{1}{2}\,(e^{i\varphi}|0\rangle_{\mathrm{Id}} - |1\rangle_{\mathrm{Id}})\otimes(|0\rangle_{\mathrm{Si}} - e^{i\varphi}|1\rangle_{\mathrm{Si}})$, $|\Psi\rangle_{\mathrm{DA}} = \frac{1}{2}\,(e^{i\varphi}|0\rangle_{\mathrm{Id}} + |1\rangle_{\mathrm{Id}})\otimes(|0\rangle_{\mathrm{Si}} - e^{i\varphi}|1\rangle_{\mathrm{Si}})$, and $|\Psi\rangle_{\mathrm{AD}} = \frac{1}{2}\,(e^{i\varphi}|0\rangle_{\mathrm{Id}} - |1\rangle_{\mathrm{Id}})\otimes(|0\rangle_{\mathrm{Si}} + e^{i\varphi}|1\rangle_{\mathrm{Si}})$. Here, D and A correspond to measurements on the spectral positions υ_6 as well as υ_5 and υ_7, respectively. The quantum interference corresponding to these projections are shown in **Figure. 37**. We calculated the quantum interference visibilities through the following formulation $\mathrm{V} = (\mathrm{CC}_{\max} - \mathrm{CC}_{\min})/(\mathrm{CC}_{\max} + \mathrm{CC}_{\min})$ where $\mathrm{CC}_{\max}$ and $\mathrm{CC}_{\min}$ are the maximum and minimum coincidence counts without subtracting the background accidental counts (see **Table 9**).

Table. 8 Performance metrics of the frequency-bin-encoded BBM92 QKD protocol at different lengths of the optical fiber, subsequent to error reconciliation and privacy amplification steps. S^A and S^F denote the asymptotic and finite secret key rates, respectively. The maximum asymptotic and finite secret key lengths are denoted by ℓ^A and ℓ^F, respectively. The results correspond to an integration time of τ =1560 s.

	Optical attenuation (dB) [corresponding fiber length (km)]					
	0 [0]	1.64 [7]	3.71 [17]	5.73 [26]	7.98 [37]	15.6 [73]
CH1						
$S^A(s^{-1})$	8.28 ± 0.13	6.23 ± 0.11	3.95 ± 0.09	2.24 ± 0.07	1.35 ± 0.05	0.19 ± 0.02
$S^F(s^{-1})$	6.48	4.75	2.86	1.47	0.81	0.011
$S^A(N^{-1})$	0.50	0.51	0.50	0.47	0.52	0.47
$S^F(N^{-1})$	0.39	0.39	0.36	0.31	0.31	0.026
ℓ^A	12930	9724	6172	3506	2108	310
ℓ^F	10108	7424	4471	2308	1268	17
CH2						
$S^A(s^{-1})$	9.16 ± 0.16	6.95 ± 0.13	4.40 ± 0.10	2.62 ± 0.08	1.51 ± 0.06	0.18 ± 0.02
$S^F(s^{-1})$	5.30	4.04	2.50	1.26	0.61	–
$S^A(N^{-1})$	0.41	0.44	0.47	0.43	0.43	0.30
$S^F(N^{-1})$	0.24	0.25	0.26	0.20	0.17	–
ℓ^A	14302	10844	6867	4102	2367	283
ℓ^F	8271	6303	3901	1979	960	–
CH3						
$S^A(s^{-1})$	6.16 ± 0.12	3.73 ± 0.09	2.34 ± 0.07	1.24 ± 0.05	0.83 ± 0.04	0.09 ± 0.02
$S^F(s^{-1})$	4.56	2.73	1.67	0.78	0.44	–
$S^A(N^{-1})$	0.49	0.48	0.49	0.43	0.44	0.33
$S^F(N^{-1})$	0.40	0.38	0.36	0.27	0.24	–
ℓ^A	9609	5820	3659	1944	1298	149
ℓ^F	7928	4553	2691	1233	726	–

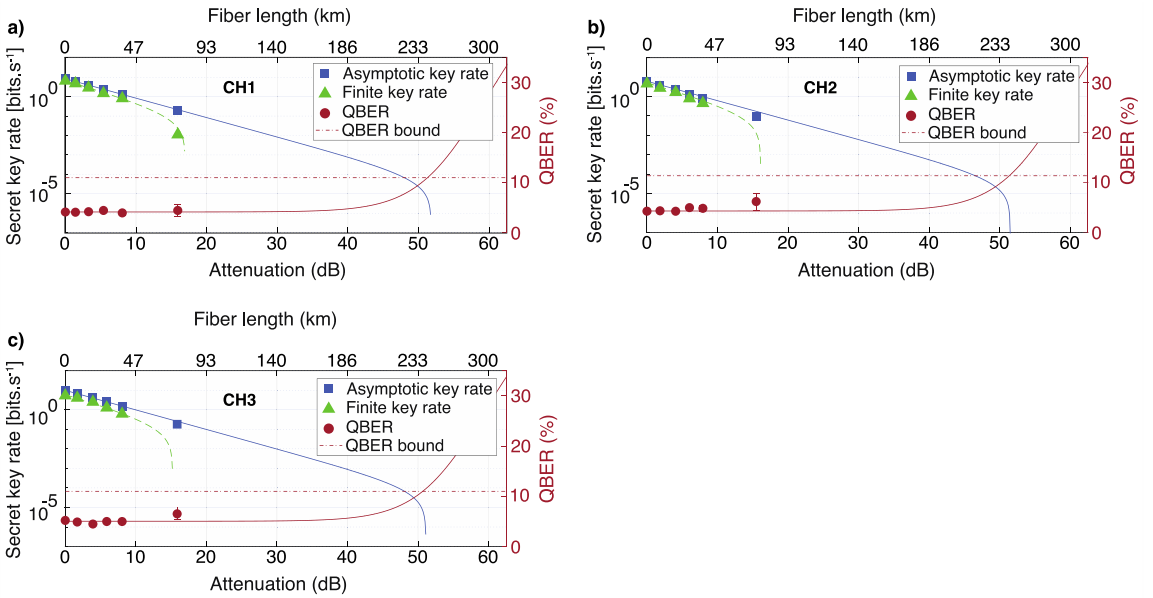

Figure. 36 Secret key rate (logarithmic representation) and QBER as function of transmission loss (bottom axis) and the equivalent optical fiber length (top axis) for frequency channels **a)** CH1, **b)** CH2, and **c)** CH3. The experimental results are shown with geometrical coloured shapes. The theoretical predictions for asymptotic secret key rate and QBER are indicated with solid blue and red lines, respectively. The theoretical prediction for the finite secret key rate is indicated with green dotted lines. At ~15 dB optical attenuation (equivalent to ~73 km optical fiber length) the finite secret key rate for CH1 is 0.011/s, whereas for CH2 and CH3 the values are negative and thus no finite key can be extracted. The red dotted horizontal line represents the 11% upper bound of the QBER, below which the security of a protocol with a positive non-zero secret key is guaranteed.

Table. 9 Visibilities of the quantum interferences corresponding to the projection vectors $|DD\rangle_{Si,Id}$, $|AD\rangle_{Si,Id}$, $|AA\rangle_{Si,Id}$ and $|DA\rangle_{Si,Id}$. The visibilities are calculated without background subtraction. The errors correspond to an integration time of 1560 s.

	Biphoton projection vector states versus the visibility of quantum interference			
	$\|DD\rangle_{Si,Id}$	$\|DA\rangle_{Si,Id}$	$\|AA\rangle_{Si,Id}$	$\|AD\rangle_{Si,Id}$
CH1	(89.59 ± 2.23) %	(93.50 ± 2.11) %	(88.66 ± 3.19) %	(93.56 ± 2.25) %
CH2	(92.16 ± 1.78) %	(92.68 ± 1.99) %	(92.25 ± 2.45) %	(92.17 ± 2.12) %
CH3	(92.43 ± 2.43) %	(92.70 ± 2.71) %	(92.22 ± 3.41) %	(93.45 ± 2.80) %

The obtained visibilities for frequency channels CH1, CH2, and CH3 indicate the violation of Bell inequality ($V > 70.71\%$ [51]) by more than ~13 standard deviation which certifies the high quality entanglement supported at different spectral regions. The exploited phase difference in odd-order negative sidebands for the basis analyzer is here reflected in a shift of the interference pattern by $\pi/2$ for the projections $|\psi\rangle_{DD}, |\psi\rangle_{AA}$ and $|\psi\rangle_{AD}, |\psi\rangle_{DA}$.

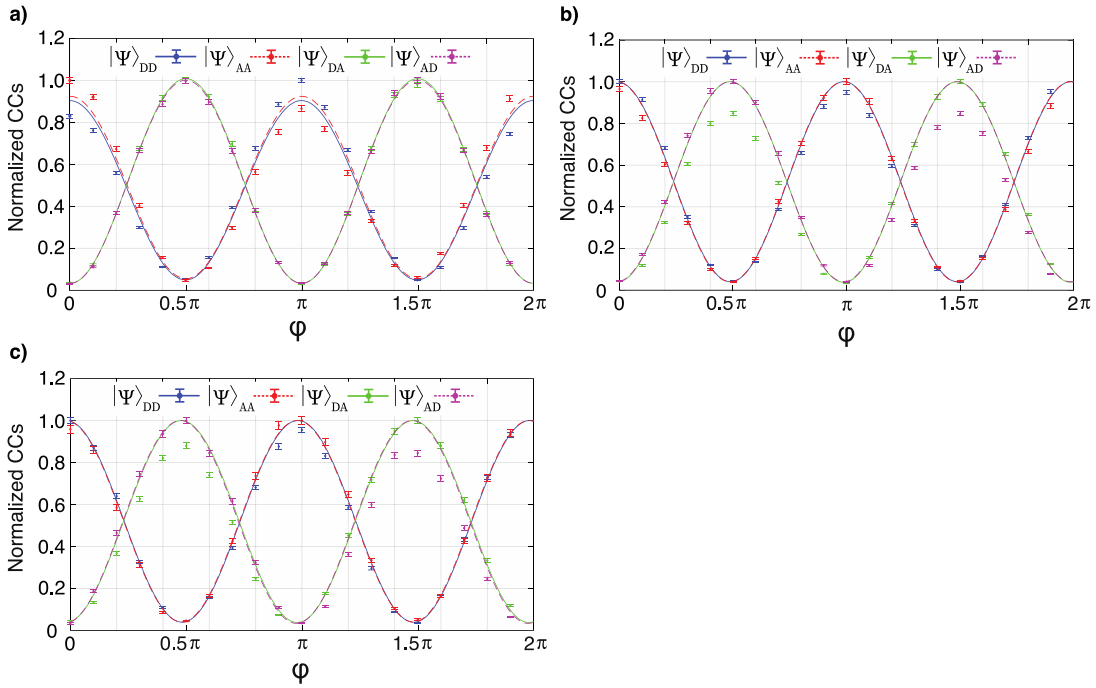

Figure. 37 Proof of non-classical correlations for projection measurements onto the states $|DD\rangle_{Si,Id}$, $|AD\rangle_{Si,Id}$, $|AA\rangle_{Si,Id}$, and $|DA\rangle_{Si,Id}$ (shown in different colors) indicating the violation of Bell inequality in the frequency channels **a)** CH1 **b)** CH2, and **c)** CH3. The solid and dotted curves are the theoretical fits and the points are the normalized average coincidence counts measured at different phase values φ. The error bars are the standard deviation corresponding to an integration time of 1560 s.

The capability of the system in preserving entanglement across remote fiber links was assessed by conducting Bell state measurements at varying amounts of optical attenuation. The average visibilities for each frequency channel can be found in **Table 10** and **Figure. 38**. It was observed that for all frequency channels at ~15 dB optical attenuation (equivalent to ~73 km fiber link), the average visibility remains above the lower threshold 70.71%, hence the Bell inequality was violated. With reference to Eq. 6.2 & 6.3, the average visibility is modelled as function of channel loss through the following relationship [135,136,140]

$$V_{ave} = 1 - 2e_0 + \frac{4(e_0 - e^{d}_{Z(X)})\,\eta_A\,\eta_B\,\frac{\mu_{Z(X)}}{2}\left(1+\frac{\mu_{Z(X)}}{2}\right)}{Q_{Z(X)}\left(1+\eta_A\frac{\mu_{Z(X)}}{2}\right)\left(1+\eta_B\frac{\mu_{Z(X)}}{2}\right)\left(1+\eta_A\frac{\mu_{Z(X)}}{2}+\eta_B\frac{\mu_{Z(X)}}{2}-\eta_A\eta_B\frac{\mu_{Z(X)}}{2}\right)} \quad (6.7)$$

To assess the capability of our approach in entanglement distribution over long fiber links, the following equation $QBER = (1 - Visibility_{ave})/2$ was considered [140], relating the

QBER and the average visibilities associated with projections onto $|DA\rangle_{Si,Id}$ and $|AD\rangle_{Si,Id}$ states. The theoretical model predicts the violation of Bell inequality across all channels up to approximately ~55 dB channel loss (equivalent to ~257 km fiber link). This underscores the capability of the presented scheme to enable frequency-insensitive entanglement distribution.

6.5. Reconfigurable Frequency-multiplexed EBQKD Network

The presented experimental approach can be extended to include multi-user EBQKD network architecture. In such a network, the central PWS allows for the specification of an arbitrary number of frequency channels and their dynamic allocation to an arbitrary number of users, hence allowing for different network topologies. According to the graph theory, for a fully-connected network of N users, at least N(N-1)/2 links are required to be established evenly among the users [35,141–143]. This can be applied to the presented approach by considering a network with a single entanglement source shared among N users and a PWS that functions as a central service provider multiplexing N-1 frequency channels into the SMF of each user. In such a network, with growing number of users, the network scales linearly since the additional quantum channels are defined from the same source of entanglement.

In **Figure. 39**, a schematic illustration of a fully-connected 4-user entanglement-based QKD network is presented. In **Figure. 39a**, the physical layer of this network is shown, where each user is connected to the service provider via a SMF and owns a personal frequency-bin basis analyser module. In the quantum correlation layer, at least six frequency channels are required to form a fully-connected quantum network. As illustrated in **Figure. 39b**, each user is linked to the other three users through at least three frequency channels. The specification of the frequency channels and their distribution among the four users to form a fully-connected network is shown in **Figure. 39c.** As is demonstrated, the channels embrace correlated signal-idler pairs of frequency-bins defined within the broadband spectrum of a single SPDC-based entanglement source. Noteworthy, in this implementation, given the 50 GHz single mode bandwidth and the 25 GHz modulation tone, a frequency spacing of 100 GHz was required to be defined between the frequency bins in each channel.

Table. 10 Average visibility of the quantum interference corresponding to projection vector states $|DA\rangle_{Si,Id}$ and $|DA\rangle_{Si,Id}$ at different lengths of the optical fiber link for frequency channels CH1, CH2, and CH3. The errors correspond to an integration time of 1560 s.

	Average visibility (%) versus optical attenuations (dB) [corresponding fiber length]					
	0 [0]	1.64 [7]	3.71 [17]	5.73 [26]	7.98 [37]	15.6 [73]
CH1	93.53 ± 1.54	93.39 ± 1.84	94.22 ± 2.19	92.89 ± 3.04	92.43 ± 4.13	91.44 ± 10.96
CH2	92.43 ± 1.45	92.62 ± 1.72	94.20 ± 2.00	92.22 ± 2.84	91.43 ± 3.79	91.02 ± 09.55
CH3	93.07 ± 1.95	93.98 ± 2.35	93.46 ± 3.07	94.35 ± 3.66	92.63 ± 5.25	92.43 ± 12.74

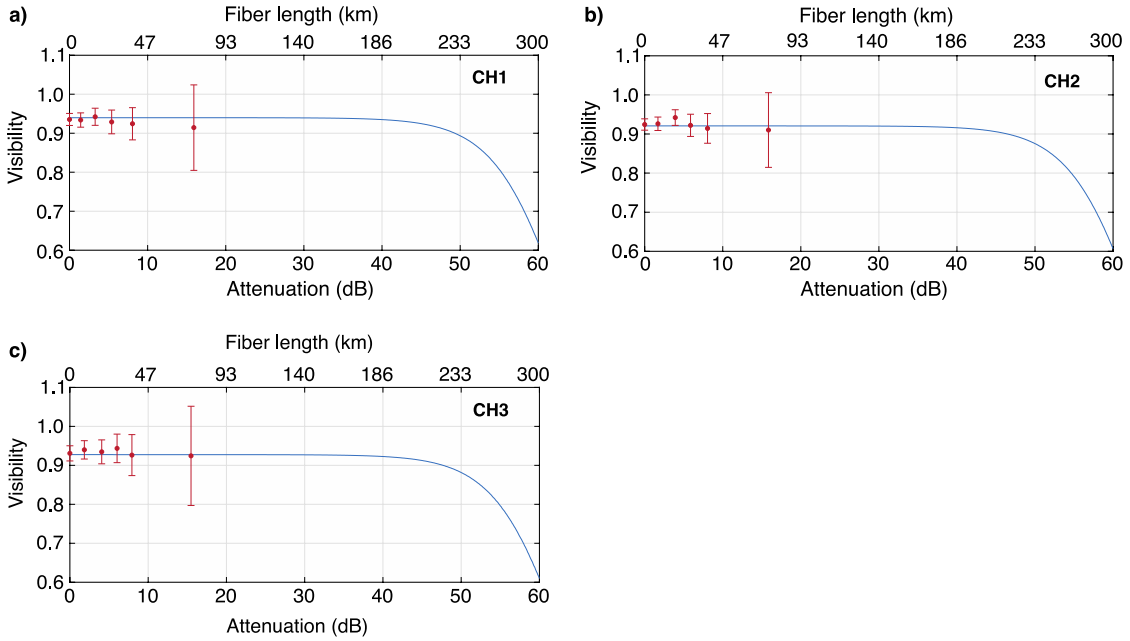

Figure. 38 The visibility of quantum interference at different attenuations (bottom axis) corresponding to different optical fiber lengths (top axis) for frequency channels **a)** CH1, **b)** CH2, and **c)** CH3. The experimental data are shown with dots and the solid curves are the theoretical models. The error bars are standard deviations corresponding to a measurement integration time of 1560 s. The increasing standard deviation with increased optical attenuation stems from lower measurement statistics.

As a result, in a four-user fully-connected EBQKD network, some frequency-bins are left unassigned such as I04, I08 and I09. However, the frequency bins I04 and I08 could also be deployed together as an additional QKD channel and multiplexed to a fifth added user. With this specific spectral configuration for channel allocation, the frequency bin I09 would ultimately be left unassigned as the adjacent frequency bin to I09 needs to be necessarily selected either I13 or I05. Modified RF modulation tones could realize an

optimized sideband modulation setting to save on the available frequency bins for allocation of further QKD channels to additional users in the network.

Note that the presented approach allows for the connection of two users through more than one quantum channel (see Charlie and Fiona in **Figure. 39**), which increases the key rate while preserving the security as the secret key bits from each channel can be simply added. This is in contrast to increasing the photon flux by applying higher excitation powers aiming at improving the finite secret key rate. In the latter case, the CAR will decrease, the entanglement quality degrades, and the QBER will increase accordingly. To create the finite key, more raw key bits will in turn be required. The allocation of more than one quantum channel for finite key extraction can be an alternative solution to increasing the pump power. Note that for the case where two users are connected by more than one quantum channel, the channel in which projection measurement is performed does not necessarily need to be announced in the sifting stage (however, at the cost of increased QBER).

The connection between the users can be dynamically reconfigured enabling to adjust to the demand on the key exchange load. Moreover, this fully-connected network architecture can also be reduced to subset topologies to enable QKD between any given two or three users.

6.6. Summary and Conclusion

A proof-of-concept experimental realization of a frequency-bin encoded BBM92 EBQKD protocol was demonstrated for which a novel, scalable and resource-efficient frequency-bin basis analyser module was developed. In this implementation, random projection measurements in the Z and X basis were realized simultaneously based on electro-optic phase modulation of the signal and idler photons in each frequency channel. Importantly, as opposed to previous implementations of the BBM92 protocol [36], the constant phase modulation settings throughout the protocol renders the users needless of any active switching between different settings to enable the transition between the Z and X basis projection measurements. This is a significant advantage of the presented approach for that it realizes directly the condition of random choice of basis (required by the BBM92 protocol to ensure security) as well as a speed-up in communications.

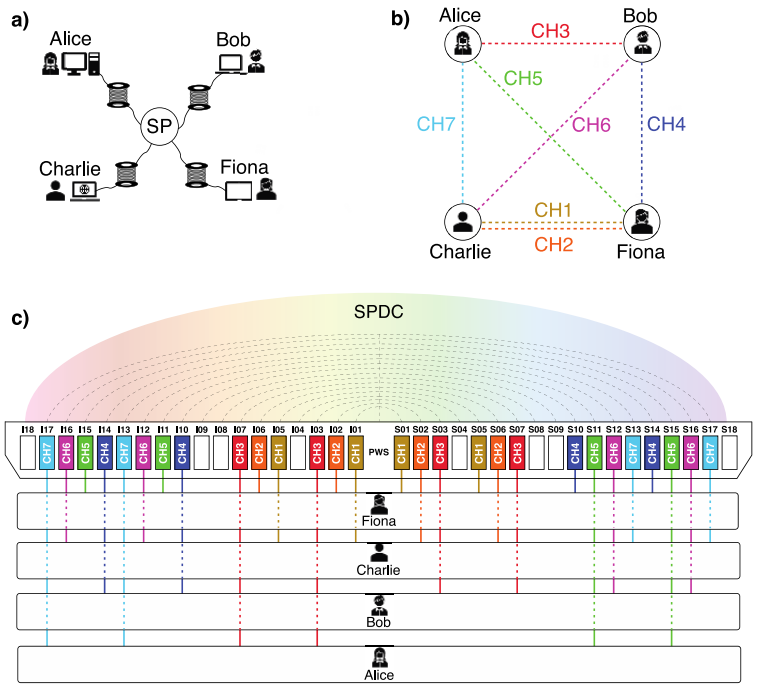

Figure. 39 Schematic illustration of **a)** the physical layer, **b)** the quantum correlation layer, and **c)** the spectral configuration of a fully-connected 4-user EBQKD network. The frequency bins belonging to the same channel are presented with the same colour and are labelled with an identical channel number ranging from 1 to 6. The pairs of correlated signal and idler frequency bins from the same SPDC process are shown with dotted curves and are numbered from 01 to 18. (SP: Service Provider, PWS: Programmable Wavelength Switch, SPDC: Spontaneous Parametric Down Conversion)

Based on a frequency-to-time-mapping technique, a frequency demultiplexing capability in time was showcased, providing each user with access to the projection states using only a single SNSPD. In contrast to schemes where each user is necessarily equipped with four detectors to detect the four Z and X basis projection states for one quantum channel, the employment of a single detector by each user reduces considerably the resource overhead, minimizes the dark count contribution and the overall vulnerability of the protocol to the detector side-channel attacks. Moreover, the use of a single detector mitigates the imbalance (the asymmetry arising from different amounts of loss encountered in users' optical paths as well as the detectors' intrinsic detection efficiency mismatch), required to meet the fair sampling condition to maintain the security level of the protocol. In enabling such characteristics, our approach contributes significantly to reducing complexity while maintaining the security of the protocol.

The frequency-insensitivity of our approach in preserving high-quality entanglement over long fiber links enables entanglement distribution in quantum networks of metropolitan scale. Noteworthy, with a common transmission mode technique for the RF signal and the

optical field, phase stability for the basis state projections required in practical scenarios can be readily achieved. The compatibility of the photonic frequency domain with standard fiber-optic telecommunication infrastructure renders it directly deployable.

The architecture of the presented analyser module allows for the inclusion of additional frequency channels to the QKD network without any hardware overhead. Remarkably, the capability of our approach was showcased in detecting the projection states corresponding to N >1 quantum channels using the same single detector rather than N×4 detectors. Additionally, for N quantum channels, a single electro-optic phase modulator can be employed rather than N phase modulators, hence providing a simultaneous frequency-mixing and random projection measurements of all channels, in turn addressing the scalability hurdles in large-scale quantum networks.

The frequency-to-time mapping technique adopted in the presented approach provides simultaneous demultiplexing-in-time of the measurement outcomes of all channels to enable their detection with one single detector. However, a trade-off between the pulsed laser repetition rate and the number of multiplexed frequency channels needs to be considered. The lower the repetition rate of the pulsed laser, the larger the capacity for multiplexing additional frequency channels. The frequency-channel multiplexing can be directly used to increase the key exchange rate in a point-to-point QKD. This is an alternative solution to increasing the pump power, which is unavoidably accompanied by a degraded signal-to-noise ratio, hence detrimental to entanglement fidelity. At the same time, using the same quantum light source and adding further basis analysers, the frequency-channel multiplexing can be exploited to expand the network for multi-user operations within different network topologies. It is important to note that the efficiency of photon pair generation in SPDC process can differ over its spectral emission range which affects the key exchange rate of different channels. However, the affected key rate of such channels could be compensated for by shaping the source's emission characteristics.

The frequency domain combined with the programmable wavelength switch provides an adaptive implementation platform capable of supporting dynamic networking functionalities, in contrast to static wavelength-division-multiplexing components. Specifically, our frequency multiplexing approach can support a dynamic architecture for wavelength allocation to multiple users (hence a further optimized resource-overhead). The basis analyser directly accepts different frequency channels without a change of system hardware and only by adaptation in measurement operation via a software control. Our

approach thus allows for a scalable multi-user QKD network with an adaptive topology, wherein the key rate could be optimized dynamically on-demand with maintained security. Our proof-of-concept demonstration for frequency-bin entanglement-based QKD lays the foundation for further advancements. For example, on-chip integration can be adopted in future steps to reduce loss by an amount of 4-5 dB per module and brightness-enhanced sources could be considered to further improve the key rates. The presented solution demonstrates dynamic resource-efficient QKD for multi-user operations with different topologies, thus supporting scalability to future quantum networks.

7. Summary, Conclusion and Future Outlook

This thesis provides proof-of-concept contributions for addressing the scalability of future quantum networks by harnessing the potential of photonic frequency encoding and information processing.

7.1. Summary and Conclusion

In this thesis, the first-time measurement of the second-order degree of coherence as function of frequency correlations was revealed, allowing for a time-efficient, precise and reliable determination of the single frequency mode bandwidth which is essential to QIP applications that involve quantum interference.

The bosonic and fermionic-like HOM effects between independent single photons were demonstrated for the first time in the frequency domain and within a unique dynamic frequency processing setup, demonstrating the scalability potential of frequency-domain processing for large-scale quantum networks.

Additionally, the HOM effect between a thermal field and a heralded state was demonstrated for the first time in the frequency domain. This experiment gave prominence to the previously unobserved phenomena concerning the partial contribution of multiphoton components in heralded states to the HOM visibility with a potential application to certain QKD protocols and different QIP applications in quantum networks. Importantly, a novel theoretical description was derived showing the relationship between the HOM visibility and the average photon number of the interacting fields.

Moreover, the EBQKD was demonstrated for the first-time using frequency-bin encoding and in a reconfigurable frequency multiplexing quantum network. In this implementation, dynamic allocation of multiple quantum channels was feasible via the adaptive frequency multiplexing capability. In addition, passive random projection measurements in two mutually unbiased basis by each user was realized via a single measurement apparatus and using only a single detector rather than four detectors. The presented approach was thus demonstrated resource-efficient and featured less vulnerability to detector side channel attacks compared to conventional implementations of the BBM92 protocol. The dynamic architecture of the frequency-bin processing setup thus enables multi-user QKD operations

with an enhanced security, and provides resource efficiency, hence proved to contribute to the overall scalability of quantum key distribution networks.

7.2. Future Outlook

The research solutions demonstrated in this thesis, lay the foundations of future steps to address the distance limitations of entanglement distribution in quantum networks. The trusted-node and relay-based schemes [144], currently exploited in quantum networks to extend the distance of entanglement distribution, inevitably compromise the security of quantum protocols. The frequency-domain experimental solutions in this thesis, i.e., the spectral HOM effect and the frequency-domain EBQKD, provide a framework to implement the frequency-domain quantum teleportation, which is the basis of the future quantum repeaters technology as an alternative solution to the relay-based schemes.

The experimental results of EBQKD demonstrated that in order to extend the distance of high quality entaglement distribution and to preserve the security of protocol within the standard limits (QBER<11%), stable projection measurements are indispensable. With the presented approach in this thesis, it is thus required for the RF tone and the frequency bins to be phase stabilized to a reference frame. In a practical scenario where the users are at distant locations, the random phase drifts of the optical field and the RF signal emerging from environmental fluctuations, can perturb the output space of the projection measurements, yielding disturbed projection states. This increases the QBER and in turn the security of the protocol. In a future implementation step, the phase stability can be realized by using the common transmission mode technique for the RF signal and the optical field. This allows for the accumulation of identical amounts of phase drift for the propagating photons and the RF signal, hence realizing a stable projection measurement basis space and an overall enhanced security for the protocol.

In addition, fully on-chip integration of the frequency processing setup can be considered to reduce the amount of loss encountered by each user and in turn to boost the security of the protocol. Furthermore, the multi-mode nature of the frequency domain can be further harnessed to realize high-dimensional encoding of secret key, or in combination with time-bin encoding, to realize hyper-entangled states, hence intrinsically augmenting the noise-resilience nature of the encoding platform, and in turn improving the overall security of the protocol.

On the other note, by relying on the equivalence between the HOM effect and key components in machine learning such as the swap test [145], the HOM effect in frequency domain can be deployed for the classification of high dimensional vectors as a means to accelerate the classically intractable classification tasks.

Overall, with the research presented in this thesis, the initial framework based on frequency processing was established to address the scalability issues of photonic quantum networks.

Appendix I

The equivalence between the cross-correlation function $g_{3,4}^{(2)}$ and the auto-correlation function $g_{1,1}^{(2)}$ in Eq. 2.32 can be proved as it follows. The creation and destruction operators corresponding to the input and output ports of the beam splitter in **Figure. 7** can be written as follows

$$\hat{a}_3^\dagger = \mathrm{R}^* \hat{a}_1^\dagger + \mathrm{T}^* \hat{a}_2^\dagger \tag{I.1}$$

$$\hat{a}_3 = \mathrm{R}\, \hat{a}_1 + \mathrm{T} \hat{a}_2$$

$$\hat{a}_4^\dagger = \mathrm{T}^* \hat{a}_1^\dagger + \mathrm{R}^* \hat{a}_2^\dagger$$

$$\hat{a}_4 = \mathrm{T} \hat{a}_1 + \mathrm{R} \hat{a}_2$$

where R^* and T^* are the transpose conjugates of the reflection and transmission coefficients of the beam splitter. In the denominator of Eq. 2.32, the average photon number in the output ports 3 and 4 can be obtained from the following

$$\begin{aligned} \langle \hat{n}_3 \rangle &= \langle 0|_2 \langle arb|_1 \, \hat{a}_3^\dagger \hat{a}_3 \, |arb\rangle_1 |0\rangle_2 \\ &= \langle 0|_2 \langle arb|_1 (\mathrm{R}^* \hat{a}_1^\dagger + \mathrm{T}^* \hat{a}_2^\dagger)(\mathrm{R} \hat{a}_1 + \mathrm{T} \hat{a}_2) \, |arb\rangle_1 |0\rangle_2 \\ &= |\mathrm{R}|^2 \langle arb|_1 \, \hat{a}_1^\dagger \hat{a}_1 \, |arb\rangle \\ &= |\mathrm{R}|^2 \langle arb|_1 \hat{n}_1 \, |arb\rangle_1 \\ &= |\mathrm{R}|^2 \langle \hat{n}_1 \rangle \end{aligned} \tag{I.2}$$

where $|arb\rangle_1 |0\rangle_2$ is the input state to the beam splitter. Similarly, it can be proved that

$$\langle \hat{n}_4 \rangle = |\mathrm{T}|^2 \langle \hat{n}_1 \rangle. \tag{I.3}$$

In the nominator of Eq. 2.32, the photon number correlation $\langle \hat{n}_3 \hat{n}_4 \rangle$ between the output ports can be written as follows

$$\langle \hat{n}_3 \hat{n}_4 \rangle = \langle 0|_2 \langle arb|_1 \, \hat{a}_3^\dagger \hat{a}_3 \hat{a}_4^\dagger \hat{a}_4 \, |arb\rangle_1 |0\rangle_2 \tag{I.4}$$

$$= \langle 0|_2 \langle arb|_2 (\mathrm{R}^* \hat{a}_1^\dagger + \mathrm{T}^* \hat{a}_2^\dagger)(\mathrm{R}\hat{a}_1 + \mathrm{T}\hat{a}_2)$$

$$\times (\mathrm{T}^* \hat{a}_1^\dagger + \mathrm{R}^* \hat{a}_2^\dagger)(\mathrm{T}\hat{a}_1 + \mathrm{R}\hat{a}_2)|arb\rangle_1 |0\rangle_2$$

$$= \mathrm{R}^*\mathrm{R}\mathrm{T}^*\mathrm{T} \, \langle arb|_1 \hat{a}_1^\dagger \hat{a}_1 \hat{a}_1^\dagger \hat{a}_1 \, |arb\rangle_1 + \mathrm{R}^*\mathrm{T}\mathrm{R}^*\mathrm{T} \, \langle arb|_1 \hat{a}_1^\dagger \hat{a}_1 |arb\rangle_1$$

$$= \mathrm{R}^*\mathrm{R}\mathrm{T}^*\mathrm{T} \, \langle arb|_1 \hat{a}_1^\dagger \hat{a}_1 \hat{a}_1^\dagger \hat{a}_1 \, |arb\rangle_1 - \mathrm{R}\mathrm{T}^*\mathrm{R}^*\mathrm{T} \, \langle arb|_1 \hat{a}_1^\dagger \hat{a}_1 |arb\rangle_1$$

$$= \mathrm{R}^*\mathrm{R}\mathrm{T}^*\mathrm{T} \, \langle arb|_1 \hat{a}_1^\dagger (\hat{a}_1^\dagger \hat{a}_1 + 1) \hat{a}_1 \, |arb\rangle_1 - \mathrm{R}\mathrm{T}^*\mathrm{R}^*\mathrm{T} \, \langle arb|_1 \hat{a}_1^\dagger \hat{a}_1 |arb\rangle_1$$

$$= |\mathrm{R}|^2 |\mathrm{T}|^2 \, \langle arb|_1 \hat{a}_1^\dagger \hat{a}_1^\dagger \hat{a}_1 \hat{a}_1 \, |arb\rangle_1$$

$$= |\mathrm{R}|^2 |\mathrm{T}|^2 \, \langle arb|_1 \hat{a}_1^\dagger (\hat{a}_1 \hat{a}_1^\dagger - 1) \hat{a}_1 \, |arb\rangle_1$$

$$= |\mathrm{R}|^2 |\mathrm{T}|^2 \, \langle arb|_1 \hat{n}_1 (\hat{n}_1 - 1) \, |arb\rangle_1$$

$$= |\mathrm{R}|^2 |\mathrm{T}|^2 \langle \hat{n}_1 (\hat{n}_1 - 1) \rangle.$$

From Eq. I.2-I.4, it can be concluded that

$$g_{3,4}^{(2)}(\tau) = \langle \hat{n}_3 \hat{n}_4 \rangle / (\langle \hat{n}_3 \rangle \langle \hat{n}_4 \rangle) \tag{I.5}$$

$$= \langle \hat{n}_1 (\hat{n}_1 - 1) \rangle / \langle \hat{n}_1 \rangle^2.$$

Given the definition of $g^{(2)}(\tau)$ in Eq. I.6 for a single-mode light,

$$g_{1,1}^{(2)}(\tau) = \langle \hat{a}_1^\dagger \hat{a}_1^\dagger \hat{a}_1 \hat{a}_1 \rangle / \langle \hat{a}_1^\dagger \hat{a}_1 \rangle^2 \tag{I.6}$$

$$= \langle \hat{a}_1^\dagger (\hat{a}_1 \hat{a}_1^\dagger - 1) \hat{a}_1 \rangle / \langle \hat{a}_1^\dagger \hat{a}_1 \rangle^2$$

$$= \langle \hat{n}_1 (\hat{n}_1 - 1) \rangle / \langle \hat{n}_1 \rangle^2,$$

it can thus be concluded that $g_{3,4}^{(2)}(\tau) = g_{1,1}^{(2)}(\tau)$.

Appendix II

For the single frequency-mode heralded state, the coincidence detections from multiphoton components from the same temporal mode – the same pulse – emerge approx. twice as much as when emitted from two different temporal modes – two different pulses, which is a characteristic of a thermal photon statistics.

In literature [125], the HOM effect is generally implemented by introducing different delay $\Delta\tau$ values between the two input (spatial) modes of the beam splitter (see **Figure. 40 a**). By means of an optical delay line placed in one input mode of the beam splitter, the gradual shift from full indistinguishability to distinguishability of photons is realized, in turn allowing for the emergence of the HOM dip. In such approaches, the contribution to the coincidence counts by multiphoton components persist at an identical rate for all delay values $\Delta\tau$. This is shown in **Figure. 40 a**, where the coincidence events $CC_{i1,i1|s1}$ are collected over the displayed detection window. Regardless of the delay value $\Delta\tau$ between the input modes of the beam splitter, the coincidence counts from multiphotons (residing in the same temporal mode) emerge at an enhanced (twice as much) rate compared with the coincidence detections from different temporal modes. This justifies the practice of considering the delayed events as the reference point which is a common practice to retrieve the HOM visibility.

Contrary to such implementations, in the HOM experiment presented in this thesis (see **Figure. 40 b**) the delay is not introduced by using an optical delay line. In this experiment, 'inter-pulse delay' principle is considered, i.e., the coincidence events are collected exclusively at delay values defined as integer multiples of the pulse period (T). As a result, the contribution of multiphoton components to the coincidence counts differs at $\Delta t = 0$ and $\Delta t \neq 0$, due to different photon statistics involved. Namely, for $\Delta t = 0$, the coincidence counts from multiphoton components emerge twice as much as those of emerging at $\Delta t \neq 0$. In light of this fact, to determine the reference point CC_{ref}, the enhancement coefficient of (approx.) two is to be considered for the coincidence counts stemming from multiphoton components.

The source of difference between the reference point CC_{ref} and the delayed CC ($\Delta t \neq 0$) and non-delayed CC (0) measured coincidence counts lies in the fact that at zero delay, due to temporal indistinguishability, the two-photon amplitudes from different input modes of the beam splitter get involved in the HOM effect. In order to obtain the exact value of CC_{ref},

full distinguishability was assumed for the photons which would inhibit their involvement in the HOM effect, hence emerging as coincidence detections. With reference to the previous explanations, the delayed coincidence counts from multiphoton components exhibit no enhancement. However, at zero delay, the thermal statistics associated with multiphoton components leads to an enhancement with a factor of $\sim$ two, which renders additional coincidence counts at zero delay, hence accounting for the difference between $\mathrm{CC_{ref}}$ and CC ($\Delta t \neq 0$). In the HOM experiment, the photons at zero delay feature temporal indistinguishability which leads to their involvement in the HOM effect, thus bunching in the output modes. As a result, from the total two-photons at zero delay, a portion does not emerge as a coincidence detection, introducing a difference between CC (0) and $\mathrm{CC_{ref}}$. The ratio of two-photon events involved in the HOM effect, i.e., $\mathrm{CC_{ref}}$ – CC (0), to the reference point $\mathrm{CC_{ref}}$, reveals the HOM visibility.

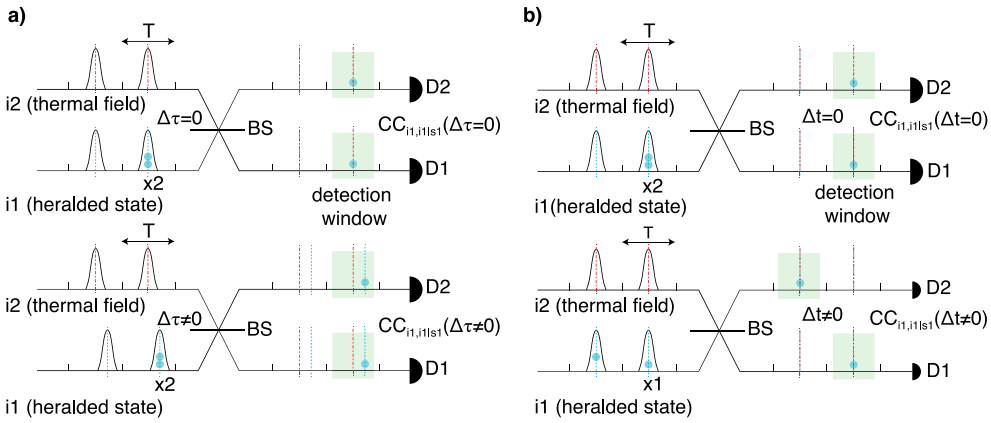

Figure. 40 Illustrative comparison of the experimental schemes for the implementation of the HOM effect: **a)** The common approach using optical delay lines, where the coincidence detections are collected over a specified detection window. Delay $\Delta\tau$ in such approaches is exerted between the two input (spatial) modes of the beam splitter. In this approach, for all delay values $\Delta\tau$, the contribution by multiphoton components from the same temporal mode persists at a constant rate. **b)** The principal adopted in the experiments of this thesis, which relies on the inter-pulse definition of delay between the detectors, i.e., exclusively defined in terms of non-zero integer multiples of the pulse period T ($\Delta t = m \times \mathrm{T}\,; m = \pm 1, \pm 2, \pm 3, ...$).

Appendix III

A modulation-disabled experiment was performed within the same experimental setup and spectral configuration presented in **Figures. 25** & **26**. Since no frequency mixing is performed, in this experiment the detectors D1 and D2 detect photons exclusively emitted from frequency modes i1 and i2, respectively (detections on D1 were heralded by D3).

From this experiment the following generation ratio $\bar{n}_{i1,th} \,/\, \bar{n}_{i2} \approx 1.02$ was obtained whose value depends on the output spectral density of the SPDC process. A delayed coincidence detection between D1 and itself ($\mathrm{D1-D1|D3}$) corresponds to two independent SPDC processes. The same also applies to the coincidence detections between D1 and D2 ($\mathrm{D2-D1|D3}$). The ratio between the generation rate (or the average photon number) of multiphoton components in i1 to i2 ($\bar{n}_{i1,th}/\bar{n}_{i2}$) could thus be obtained through the following

$$\frac{\bar{n}_{\mathrm{i1,th}}}{\bar{n}_{\mathrm{i2}}} = \frac{\mathrm{CC}^{ave}_{\mathrm{D1,D1|D3}}(\Delta \mathrm{t})}{\mathrm{CC}^{ave}_{\mathrm{D2,D1|D3}}(\Delta \mathrm{t}')} \tag{III.1}$$

On the right side of Eq. III.1, the nominator is the average three-fold coincidence counts between D1 (heralded by D3) and the delayed triggered detections on the same detector D1 ($\Delta t = m \times \tau; \tau = 20\, ns;\ m = \pm 1, \pm 2, \ldots$; It is important to note that the values for m start at ±1 (and not 0) due to the detectors' deadtime). The denominator stands for the average coincidence counts at different delays ($\Delta \mathrm{t}' = m \times \tau; \tau = 20$ ns; $m = 0, \pm 1, \pm 2, \ldots$) between the heralded detections on D1 and the triggered detections on D2.

Appendix IV

The HOM effect between two thermal fields (denoted by 1 and 2) is treated theoretically in this section. To derive the relationship between the HOM visibility and the average photon number of the fields, Eq. 2.31 is followed, giving access to the density matrix of a thermal field. The first and second-order moments are written as

$$\langle \hat{a}^{\dagger}\hat{a}\rangle_{th} = \mathrm{Tr}\{\hat{a}^{\dagger}\hat{a}\,\hat{\rho}_{th}\} = \overline{n} \qquad \text{(IV.I)}$$

$$\langle \hat{a}^{\dagger 2}\hat{a}^{2}\rangle_{th} = \mathrm{Tr}\{\hat{a}^{\dagger 2}\hat{a}^{2}\,\hat{\rho}_{th}\} = 2\overline{n}^{\,2}$$

and the second-order correlation function between two thermal fields is written as follows

$$g_{1,2}^{(2)}(\Delta t) = 2\overline{n}_1{}^2 + 2\overline{n}_2{}^2 + 2\overline{n}_1\overline{n}_2 - 2\overline{n}_1\overline{n}_2\,\delta_{12} \qquad \text{(IV.II)}$$

with $\overline{n}_i$ (i = 1, 2) being the mean photon number per pulse period of the thermal field corresponding to the frequency mode i. The coefficient δ_{12} in Eq. IV.II imparts the degree of temporal indistinguishability between the thermal fields at their arrival time at the beam splitter. Under perfect indistinguishability ($\delta_{12} = 1$), the correlation function lies at its minimum $g_{1,2}^{(2)}(0)_{min}$ whereas its maximum value $g_{1,2}^{(2)}(\Delta t)_{max}$ is linked with fully distinguishable fields ($\delta_{12} = 0$). Proceeding from Eq. 2.26, the HOM visibility between two thermal fields is derived as below

$$\mathrm{V}_{\mathrm{theory}} = \frac{1}{\bar{n}_1/\bar{n}_2 + \bar{n}_2/\bar{n}_1 + 1} \qquad \text{(IV-III)}$$

which demonstrates the dependency of the HOM visibility on the fields' relative average photon numbers.

Appendix V

The experimental realization of the spectral HOM effect between two thermal fields is demonstrated in this section. For this purpose, the experimental setup and spectral configuration presented in chapter five are considered. Electro-optic phase modulation was applied between the two *idler* frequency modes i1 and i2, each created from an independent SPDC process (see **Figure. 25** & **26**). For this experiment, the detections on the *idlers*' twin *signal* frequency modes were simply discarded. The thermal characteristics of the fields were independently verified through separate HBT experiments on each field, from which the second-order auto-correlation functions were measured: $g^{(2)}_{i1,i1}(0) \approx 1.93$ and $g^{(2)}_{i2,i2}(0) \approx 1.92$, corresponding to the frequency modes i1 and i2, respectively. From a modulation disabled experiment, the ratio $\overline{n}_{i1}/\overline{n}_{i2} \approx 0.97$ between average photon numbers per pulse period for the thermal fields in i1 and i2 were obtained. From Eq. IV-III, the theoretical value $\mathrm{V_{theory}} \approx 33.32\%$ for the visibility in the HOM effect between the two thermal fields was obtained. Experimentally, the visibility was retrieved by defining a reference point, composed of two-fold coincidence detections that either originate from photons in two different frequency modes or those initially residing in the same mode. For a thermal field which is composed of a superposition of two independent idler frequency modes, the enhancement coefficient (the auto-correlation function) was obtained $g^{(2)}(0) \approx 1.46$ using Eq. 2.36. At zero delay the reference point was thus defined as $\mathrm{CC_{ref}}(0) = 1.46 \times \mathrm{CC_{i1,i2}}(\Delta t \neq 0)$, wherein $\mathrm{CCs_{i1,i2}}(\Delta t \neq 0)$ is the average delayed two-fold coincidence counts whose value multiplied by the enhancement coefficient is equal to the non-delayed coincidence counts, i.e. $\mathrm{CCs_{i1,i2}}(0)$, which is here defined as the reference point, and of which a portion would vanish in experiment due to the HOM effect. In experiment, the non-delayed two-fold coincidence counts $\mathrm{CC}(0) = 756 \pm 10$ and $\mathrm{CC}_{i1,i2}(\Delta t \neq 0) = 730 \pm 2$ were measured and placed in the following relationship $\mathrm{V}_{exp} = [\mathrm{CC_{ref}} - \mathrm{CC}(0)]/\mathrm{CC_{ref}}$, giving the experimental value for the visibility, $\mathrm{V_{exp}} = 28.4\% \pm 3.1\%$ (See **Figure. 41**) which was in good agreement with the theoretical prediction.

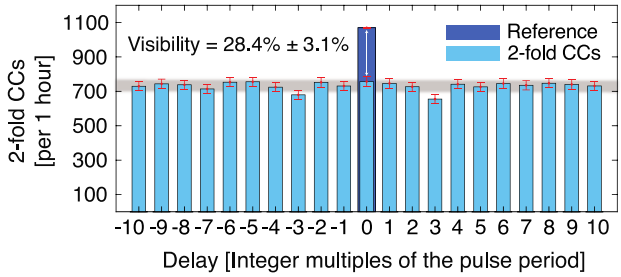

Figure. 41 Two-fold coincidence counts as function of delay in the spectral HOM experiment between two thermal fields. The error bars show standard deviation (squared root of coincidence counts) corresponding to one-hour integration time per measurement. The arrow shows the experimental value for visibility, V_{exp} = 28.4% ± 3.1% in HOM effect between two thermal fields.

For the HOM effect between two thermal fields, according to Eq. 5.12, the visibility varies dependent on the fields' relative mean photon numbers. One can see that the possible peak visibility, V_{peak} = 33.33%, occurs at $\bar{n}_{i1} = \bar{n}_{i2}$ and remains constant irrespective of the absolute values of $\bar{n}_{i1}$ and $\bar{n}_{i2}$.

Appendix VI

The BBM92 QKD protocol starts with Alice and Bob each receiving one qubit of the following frequency-bin-encoded entangled pair, represented in the Z and X basis as $|\Phi_Z\rangle = 1\sqrt{2}\,(|01\rangle_{Si,Id} + |10\rangle_{Si,Id})$ and $|\Phi_X\rangle = 1\sqrt{2}\,(|++\rangle_{Si,Id} - |--\rangle_{Si,Id})$, respectively, with Si and Id denoting Signal and Idler photons, respectively. The users perform independent projection measurements on their qubits based on a random selection among two mutually unbiased measurement basis Z and X. In the sifting stage, the users publicly announce their choices of measurement basis and discard their mismatched selections. In the parameter estimation step, the users reveal a random subset of their signals over the public channel to estimate the statistical error of their protocol. The remaining n_Z and n_X number of signals are denoted the raw key bits in the Z and X basis, respectively. To compensate for any potential security loss, error correction and privacy amplification steps are implemented and the final secret key string is extracted.

Bibliography

[1] S. Wehner, D. Elkouss, and R. Hanson, *Quantum Internet: A Vision for the Road Ahead*, Science (80-.). **362**, (2018).

[2] Y. Cao, Y. Zhao, Q. Wang, J. Zhang, S. X. Ng, and L. Hanzo, *The Evolution of Quantum Key Distribution Networks: On the Road to the Qinternet*, IEEE Commun. Surv. Tutorials **24**, 839 (2022).

[3] E. Polino, M. Valeri, N. Spagnolo, and F. Sciarrino, *Photonic Quantum Metrology*, AVS Quantum Sci. **2**, (2020).

[4] M. Caleffi, M. Amoretti, D. Ferrari, J. Illiano, A. Manzalini, and A. S. Cacciapuoti, *Distributed Quantum Computing: A Survey*, Comput. Networks **254**, 110672 (2024).

[5] D. J. Egger, C. Gambella, J. Marecek, S. McFaddin, M. Mevissen, R. Raymond, A. Simonetto, S. Woerner, and E. Yndurain, *Quantum Computing for Finance: State-of-the-Art and Future Prospects*, IEEE Trans. Quantum Eng. **1**, 1 (2020).

[6] J. Biamonte, P. Wittek, N. Pancotti, P. Rebentrost, N. Wiebe, and S. Lloyd, *Quantum Machine Learning*, Nature **549**, 195 (2017).

[7] S.-W. Lee, T. C. Ralph, and H. Jeong, *Fundamental Building Block for All-Optical Scalable Quantum Networks*, Phys. Rev. A **100**, 052303 (2019).

[8] S. Wei, B. Jing, X. Zhang, J. Liao, C. Yuan, B. Fan, C. Lyu, D. Zhou, Y. Wang, G. Deng, H. Song, D. Oblak, G. Guo, and Q. Zhou, *Towards Real-World Quantum Networks: A Review*, Laser Photon. Rev. **16**, (2022).

[9] M. Caleffi, *Optimal Routing for Quantum Networks*, IEEE Access **5**, 22299 (2017).

[10] K. Azuma, S. E. Economou, D. Elkouss, P. Hilaire, L. Jiang, H.-K. Lo, and I. Tzitrin, *Quantum Repeaters: From Quantum Networks to the Quantum Internet*, Rev. Mod. Phys. **95**, 045006 (2023).

[11] C. K. Hong, Z. Y. Ou, and L. Mandel, *Measurement of Subpicosecond Time Intervals between Two Photons by Interference*, Phys. Rev. Lett. **59**, 2044 (1987).

[12] E. Knill, R. Laflamme, and G. J. Milburn, *A Scheme for Efficient Quantum Computation with Linear Optics*, Nature **409**, 46 (2001).

[13] A. E. Ulanov, I. A. Fedorov, D. Sychev, P. Grangier, and A. I. Lvovsky, *Loss-Tolerant State Engineering for Quantum-Enhanced Metrology via the Reverse Hong–Ou–Mandel Effect*, Nat. Commun. **7**, 11925 (2016).

[14] Y. Bromberg, Y. Lahini, R. Morandotti, and Y. Silberberg, *Quantum and Classical Correlations in Waveguide Lattices*, Phys. Rev. Lett. **102**, 253904 (2009).

[15] M. K. Giri, B. Paul, and T. Mishra, *Flux-Induced Reentrant Dynamics in the Quantum Walk of Interacting Bosons*, Phys. Rev. A **108**, 063319 (2023).

[16] M. Tillmann, B. Dakić, R. Heilmann, S. Nolte, A. Szameit, and P. Walther, *Experimental Boson Sampling*, Nat. Photonics **7**, 540 (2013).

[17] P. Kok, W. J. Munro, K. Nemoto, T. C. Ralph, J. P. Dowling, and G. J. Milburn, *Linear Optical Quantum Computing with Photonic Qubits*, Rev. Mod. Phys. **79**, 135 (2007).

[18] T. B. Pittman, J. D. Franson, T. Ralph, and P. K. Lam, *Photonic Quantum Computing Using Forced Fermion-Like Behavior*, in (2011), pp. 241–244.

[19] J. L. O'Brien, G. J. Pryde, A. G. White, T. C. Ralph, and D. Branning, *Demonstration of an All-Optical Quantum Controlled-NOT Gate*, Nature **426**, 264 (2003).

[20] K. Mattle, H. Weinfurter, P. G. Kwiat, and A. Zeilinger, *Dense Coding in Experimental Quantum Communication*, Phys. Rev. Lett. **76**, 4656 (1996).

[21] S. Pirandola, J. Eisert, C. Weedbrook, A. Furusawa, and S. L. Braunstein, *Advances in Quantum Teleportation*, Nat. Photonics **9**, 641 (2015).

[22] X.-M. Hu, Y. Guo, B.-H. Liu, C.-F. Li, and G.-C. Guo, *Progress in Quantum Teleportation*, Nat. Rev. Phys. **5**, 339 (2023).

[23] F. Xu, X. Ma, Q. Zhang, H.-K. Lo, and J.-W. Pan, *Secure Quantum Key Distribution with Realistic Devices*, Rev. Mod. Phys. **92**, 025002 (2020).

[24] H.-K. Lo, M. Curty, and B. Qi, *Measurement-Device-Independent Quantum Key Distribution*, Phys. Rev. Lett. **108**, 130503 (2012).

[25] A. Einstein, B. Podolsky, and N. Rosen, *Can Quantum-Mechanical Description of Physical Reality Be Considered Complete?*, Phys. Rev. **47**, 777 (1935).

[26] E. Schrödinger, *Discussion of Probability Relations between Separated Systems*,

Math. Proc. Cambridge Philos. Soc. **31**, 555 (1935).

[27] E. Schrödinger, *Probability Relations between Separated Systems*, Math. Proc. Cambridge Philos. Soc. **32**, 446 (1936).

[28] A. K. Ekert, *Quantum Cryptography Based on Bell's Theorem*, Phys. Rev. Lett. **67**, 661 (1991).

[29] G. Ribordy, J. Brendel, J.-D. Gautier, N. Gisin, and H. Zbinden, *Long-Distance Entanglement-Based Quantum Key Distribution*, Phys. Rev. A **63**, 012309 (2000).

[30] R. Ursin, F. Tiefenbacher, T. Schmitt-Manderbach, H. Weier, T. Scheidl, M. Lindenthal, B. Blauensteiner, T. Jennewein, J. Perdigues, P. Trojek, B. Ömer, M. Fürst, M. Meyenburg, J. Rarity, Z. Sodnik, C. Barbieri, H. Weinfurter, and A. Zeilinger, *Entanglement-Based Quantum Communication over 144 Km*, Nat. Phys. **3**, 481 (2007).

[31] D. Bouwmeester, J.-W. Pan, K. Mattle, M. Eibl, H. Weinfurter, and A. Zeilinger, *Experimental Quantum Teleportation*, Nature **390**, 575 (1997).

[32] W. J. Munro, K. Azuma, K. Tamaki, and K. Nemoto, *Inside Quantum Repeaters*, IEEE J. Sel. Top. Quantum Electron. **21**, 78 (2015).

[33] R. Kaltenbaek, B. Blauensteiner, M. Żukowski, M. Aspelmeyer, and A. Zeilinger, *Experimental Interference of Independent Photons*, Phys. Rev. Lett. **96**, 240502 (2006).

[34] F. Bouchard, A. Sit, Y. Zhang, R. Fickler, F. M. Miatto, Y. Yao, F. Sciarrino, and E. Karimi, *Two-Photon Interference: The Hong–Ou–Mandel Effect*, Reports Prog. Phys. **84**, 012402 (2021).

[35] S. Wengerowsky, S. K. Joshi, F. Steinlechner, H. Hübel, and R. Ursin, *An Entanglement-Based Wavelength-Multiplexed Quantum Communication Network*, Nature **564**, 225 (2018).

[36] F. Appas, F. Baboux, M. I. Amanti, A. Lemaítre, F. Boitier, E. Diamanti, and S. Ducci, *Flexible Entanglement-Distribution Network with an AlGaAs Chip for Secure Communications*, Npj Quantum Inf. **7**, 118 (2021).

[37] M. Peranić, M. Clark, R. Wang, S. Bahrani, O. Alia, S. Wengerowsky, A. Radman, M. Lončarić, M. Stipčević, J. Rarity, R. Nejabati, and S. K. Joshi, *A Study of*

Polarization Compensation for Quantum Networks, EPJ Quantum Technol. **10**, 30 (2023).

[38] S. Wengerowsky, S. K. Joshi, F. Steinlechner, J. R. Zichi, B. Liu, T. Scheidl, S. M. Dobrovolskiy, R. van der Molen, J. W. N. Los, V. Zwiller, M. A. M. Versteegh, A. Mura, D. Calonico, M. Inguscio, A. Zeilinger, A. Xuereb, and R. Ursin, *Passively Stable Distribution of Polarisation Entanglement over 192 Km of Deployed Optical Fibre*, Npj Quantum Inf. **6**, 5 (2020).

[39] S. Chatterjee, K. Goswami, R. Chatterjee, and U. Sinha, *Polarization Bases Compensation towards Advantages in Satellite-Based QKD without Active Feedback*, Commun. Phys. **6**, 116 (2023).

[40] E. Fitzke, L. Bialowons, T. Dolejsky, M. Tippmann, O. Nikiforov, T. Walther, F. Wissel, and M. Gunkel, *Scalable Network for Simultaneous Pairwise Quantum Key Distribution via Entanglement-Based Time-Bin Coding*, PRX Quantum **3**, 020341 (2022).

[41] F. Bouchard, D. England, P. J. Bustard, K. Heshami, and B. Sussman, *Quantum Communication with Ultrafast Time-Bin Qubits*, PRX Quantum **3**, 010332 (2022).

[42] J.-H. Kim, J.-W. Chae, Y.-C. Jeong, and Y.-H. Kim, *Quantum Communication with Time-Bin Entanglement over a Wavelength-Multiplexed Fiber Network*, APL Photonics **7**, (2022).

[43] J. Wang, Q. Wang, J. Liu, and D. Lyu, *Quantum Orbital Angular Momentum in Fibers: A Review*, AVS Quantum Sci. **4**, (2022).

[44] Q.-K. Wang, F.-X. Wang, J. Liu, W. Chen, Z.-F. Han, A. Forbes, and J. Wang, *High-Dimensional Quantum Cryptography with Hybrid Orbital-Angular-Momentum States through 25 Km of Ring-Core Fiber: A Proof-of-Concept Demonstration*, Phys. Rev. Appl. **15**, 064034 (2021).

[45] D. Cozzolino, D. Bacco, B. Da Lio, K. Ingerslev, Y. Ding, K. Dalgaard, P. Kristensen, M. Galili, K. Rottwitt, S. Ramachandran, and L. K. Oxenløwe, *Orbital Angular Momentum States Enabling Fiber-Based High-Dimensional Quantum Communication*, Phys. Rev. Appl. **11**, 064058 (2019).

[46] M. Cabrejo-Ponce, A. L. M. Muniz, M. Huber, and F. Steinlechner, *High-Dimensional Entanglement for Quantum Communication in the Frequency*

Domain, Laser Photon. Rev. **17**, (2023).

[47] H.-H. Lu, N. A. Peters, A. M. Weiner, and J. M. Lukens, *Characterization of Quantum Frequency Processors*, IEEE J. Sel. Top. Quantum Electron. **29**, 1 (2023).

[48] H.-H. Lu, A. M. Weiner, P. Lougovski, and J. M. Lukens, *Quantum Information Processing With Frequency-Comb Qudits*, IEEE Photonics Technol. Lett. **31**, 1858 (2019).

[49] D. Cozzolino, B. Da Lio, D. Bacco, and L. K. Oxenløwe, *High-Dimensional Quantum Communication: Benefits, Progress, and Future Challenges*, Adv. Quantum Technol. **2**, (2019).

[50] R. Osellame, *A Larger Quantum Alphabet*, Nature **546**, 602 (2017).

[51] M. Kues, C. Reimer, P. Roztocki, L. R. Cortés, S. Sciara, B. Wetzel, Y. Zhang, A. Cino, S. T. Chu, B. E. Little, D. J. Moss, L. Caspani, J. Azaña, and R. Morandotti, *On-Chip Generation of High-Dimensional Entangled Quantum States and Their Coherent Control*, Nature **546**, 622 (2017).

[52] H. Mahmudlu, R. Johanning, A. van Rees, A. Khodadad Kashi, J. P. Epping, R. Haldar, K.-J. Boller, and M. Kues, *Fully On-Chip Photonic Turnkey Quantum Source for Entangled Qubit/Qudit State Generation*, Nat. Photonics **17**, 518 (2023).

[53] J. M. Lukens and P. Lougovski, *Frequency-Encoded Photonic Qubits for Scalable Quantum Information Processing*, Optica **4**, 8 (2017).

[54] L. Zhang, C. Cui, J. Yan, Y. Guo, J. Wang, and L. Fan, *On-Chip Parallel Processing of Quantum Frequency Comb*, Npj Quantum Inf. **9**, 57 (2023).

[55] J. D. Siverns, X. Li, and Q. Quraishi, *Ion–Photon Entanglement and Quantum Frequency Conversion with Trapped Ba^+ Ions*, Appl. Opt. **56**, B222 (2017).

[56] M. Mirhosseini, A. Sipahigil, M. Kalaee, and O. Painter, *Superconducting Qubit to Optical Photon Transduction*, Nature **588**, 599 (2020).

[57] Y. Wang, Z.-Y. Hao, Z.-H. Liu, K. Sun, J.-S. Xu, C.-F. Li, G.-C. Guo, A. Castellini, B. Bellomo, G. Compagno, and R. Lo Franco, *Remote Entanglement Distribution in a Quantum Network via Multinode Indistinguishability of Photons*, Phys. Rev. A **106**, 032609 (2022).

[58] A. Hochrainer, M. Lahiri, M. Erhard, M. Krenn, and A. Zeilinger, *Quantum*

Indistinguishability by Path Identity and with Undetected Photons, Rev. Mod. Phys. **94**, 025007 (2022).

[59] C. I. Osorio, N. Sangouard, and R. T. Thew, *On the Purity and Indistinguishability of Down-Converted Photons*, J. Phys. B At. Mol. Opt. Phys. **46**, 055501 (2013).

[60] T. A. Wright, C. Parry, O. R. Gibson, R. J. A. Francis-Jones, and P. J. Mosley, *Resource-Efficient Frequency Conversion for Quantum Networks via Sequential Four-Wave Mixing*, Opt. Lett. **45**, 4587 (2020).

[61] K. Zielnicki, K. Garay-Palmett, D. Cruz-Delgado, H. Cruz-Ramirez, M. F. O'Boyle, B. Fang, V. O. Lorenz, A. B. U'Ren, and P. G. Kwiat, *Joint Spectral Characterization of Photon-Pair Sources*, J. Mod. Opt. **65**, 1141 (2018).

[62] R. Kumar, J. R. Ong, M. Savanier, and S. Mookherjea, *Controlling the Spectrum of Photons Generated on a Silicon Nanophotonic Chip*, Nat. Commun. **5**, 5489 (2014).

[63] S. Euler, E. Fitzke, O. Nikiforov, D. Hofmann, T. Dolejsky, and T. Walther, *Spectral Characterization of SPDC-Based Single-Photon Sources for Quantum Key Distribution*, Eur. Phys. J. Spec. Top. **230**, 1073 (2021).

[64] T. Lutz, P. Kolenderski, and T. Jennewein, *Demonstration of Spectral Correlation Control in a Source of Polarization-Entangled Photon Pairs at Telecom Wavelength*, Opt. Lett. **39**, 1481 (2014).

[65] R. H. BROWN and R. Q. TWISS, *Correlation between Photons in Two Coherent Beams of Light*, Nature **177**, 27 (1956).

[66] R. HANBURY BROWN and R. Q. TWISS, *A Test of a New Type of Stellar Interferometer on Sirius*, Nature **178**, 1046 (1956).

[67] R. H. Brown and R. Q. Twiss, *LXXIV. A New Type of Interferometer for Use in Radio Astronomy*, London, Edinburgh, Dublin Philos. Mag. J. Sci. **45**, 663 (1954).

[68] K. D. Johnsen, P. Kolenderski, C. Scarcella, M. Thibault, A. Tosi, and T. Jennewein, *Time and Spectrum-Resolving Multiphoton Correlator for 300–900 Nm*, J. Appl. Phys. **116**, (2014).

[69] W. Wasilewski, P. Wasylczyk, P. Kolenderski, K. Banaszek, and C. Radzewicz, *Joint Spectrum of Photon Pairs Measured by Coincidence Fourier Spectroscopy*, Opt. Lett. **31**, 1130 (2006).

[70] A. Eckstein, G. Boucher, A. Lemaître, P. Filloux, I. Favero, G. Leo, J. E. Sipe, M. Liscidini, and S. Ducci, *High-Resolution Spectral Characterization of Two Photon States via Classical Measurements*, Laser Photon. Rev. **8**, L76 (2014).

[71] F. Kaneda, J. Oikawa, M. Yabuno, F. China, S. Miki, H. Terai, Y. Mitsumori, and K. Edamatsu, *Spectral Characterization of Photon-Pair Sources via Classical Sum-Frequency Generation*, Opt. Express **28**, 38993 (2020).

[72] I. Jizan, L. G. Helt, C. Xiong, M. J. Collins, D.-Y. Choi, C. Joon Chae, M. Liscidini, M. J. Steel, B. J. Eggleton, and A. S. Clark, *Bi-Photon Spectral Correlation Measurements from a Silicon Nanowire in the Quantum and Classical Regimes*, Sci. Rep. **5**, 12557 (2015).

[73] A. Mahjoubfar, D. V. Churkin, S. Barland, N. Broderick, S. K. Turitsyn, and B. Jalali, *Time Stretch and Its Applications*, Nat. Photonics **11**, 341 (2017).

[74] K. Goda and B. Jalali, *Dispersive Fourier Transformation for Fast Continuous Single-Shot Measurements*, Nat. Photonics **7**, 102 (2013).

[75] K. Goda, D. R. Solli, K. K. Tsia, and B. Jalali, *Theory of Amplified Dispersive Fourier Transformation*, Phys. Rev. A **80**, 043821 (2009).

[76] H.-H. Lu, O. D. Odele, D. E. Leaird, and A. M. Weiner, *Arbitrary Shaping of Biphoton Correlations Using Near-Field Frequency-to-Time Mapping*, Opt. Lett. **43**, 743 (2018).

[77] G. Brida, M. V. Chekhova, M. Genovese, M. Gramegna, and L. A. Krivitsky, *Dispersion Spreading of Biphotons in Optical Fibers and Two-Photon Interference*, Phys. Rev. Lett. **96**, 143601 (2006).

[78] S.-Y. Baek, O. Kwon, and Y.-H. Kim, *Nonlocal Dispersion Control of a Single-Photon Waveform*, Phys. Rev. A **78**, 013816 (2008).

[79] A. Valencia, M. V. Chekhova, A. Trifonov, and Y. Shih, *Entangled Two-Photon Wave Packet in a Dispersive Medium*, Phys. Rev. Lett. **88**, 183601 (2002).

[80] M. Avenhaus, A. Eckstein, P. J. Mosley, and C. Silberhorn, *Fiber-Assisted Single-Photon Spectrograph*, Opt. Lett. **34**, 2873 (2009).

[81] T. Kobayashi, R. Ikuta, S. Yasui, S. Miki, T. Yamashita, H. Terai, T. Yamamoto, M. Koashi, and N. Imoto, *Frequency-Domain Hong–Ou–Mandel Interference*, Nat.

Photonics **10**, 441 (2016).

[82] P. Imany, O. D. Odele, M. S. Alshaykh, H.-H. Lu, D. E. Leaird, and A. M. Weiner, *Frequency-Domain Hong–Ou–Mandel Interference with Linear Optics*, Opt. Lett. **43**, 2760 (2018).

[83] C. H. Bennett and G. Brassard, *Quantum Cryptography: Public Key Distribution and Coin Tossing*, Theor. Comput. Sci. **560**, 7 (2014).

[84] C. H. Bennett, G. Brassard, and N. D. Mermin, *Quantum Cryptography without Bell's Theorem*, Phys. Rev. Lett. **68**, 557 (1992).

[85] V. Scarani, H. Bechmann-Pasquinucci, N. J. Cerf, M. Dušek, N. Lütkenhaus, and M. Peev, *The Security of Practical Quantum Key Distribution*, Rev. Mod. Phys. **81**, 1301 (2009).

[86] Q. Zhang, F. Xu, Y.-A. Chen, C.-Z. Peng, and J.-W. Pan, *Large Scale Quantum Key Distribution: Challenges and Solutions [Invited]*, Opt. Express **26**, 24260 (2018).

[87] M. Bloch, S. W. McLaughlin, J.-M. Merolla, and F. Patois, *Frequency-Coded Quantum Key Distribution*, Opt. Lett. **32**, 301 (2007).

[88] N. T. Islam, C. Cahall, A. Aragoneses, A. Lezama, J. Kim, and D. J. Gauthier, *Robust and Stable Delay Interferometers with Application to d-Dimensional Time-Frequency Quantum Key Distribution*, Phys. Rev. Appl. **7**, 044010 (2017).

[89] L. Zhou, J. Lin, Y. Jing, and Z. Yuan, *Twin-Field Quantum Key Distribution without Optical Frequency Dissemination*, Nat. Commun. **14**, 928 (2023).

[90] I. Ali-Khan, C. J. Broadbent, and J. C. Howell, *Large-Alphabet Quantum Key Distribution Using Energy-Time Entangled Bipartite States*, Phys. Rev. Lett. **98**, 060503 (2007).

[91] J. Nunn, L. J. Wright, C. Söller, L. Zhang, I. A. Walmsley, and B. J. Smith, *Large-Alphabet Time-Frequency Entangled Quantum Key Distribution by Means of Time-to-Frequency Conversion*, Opt. Express **21**, 15959 (2013).

[92] J. Liu, Z. Lin, D. Liu, X. Feng, F. Liu, K. Cui, Y. Huang, and W. Zhang, *High-Dimensional Quantum Key Distribution Using Energy-Time Entanglement over 242 Km Partially Deployed Fiber*, Quantum Sci. Technol. **9**, 015003 (2024).

[93] R. Xue, X. Liu, H. Li, L. You, Y. Huang, and W. Zhang, *Measurement-Device-*

Independent Quantum Key Distribution of Frequency-Nondegenerate Photons, Phys. Rev. Appl. **17**, 024045 (2022).

[94] W. Tittel, J. Brendel, H. Zbinden, and N. Gisin, *Quantum Cryptography Using Entangled Photons in Energy-Time Bell States*, Phys. Rev. Lett. **84**, 4737 (2000).

[95] J.-Y. Hu, B. Yu, M.-Y. Jing, L.-T. Xiao, S.-T. Jia, G.-Q. Qin, and G.-L. Long, *Experimental Quantum Secure Direct Communication with Single Photons*, Light Sci. Appl. **5**, e16144 (2016).

[96] R. Loudon, *The Quantum Theory of Light* (Oxford University PressOxford, 2000).

[97] C. Couteau, *Spontaneous Parametric Down-Conversion*, Contemp. Phys. **59**, 291 (2018).

[98] Y. Niu, X. Yan, J. Chen, Y. Ma, Y. Zhou, H. Chen, Y. Wu, and Z. Bai, *Research Progress on Periodically Poled Lithium Niobate for Nonlinear Frequency Conversion*, Infrared Phys. Technol. **125**, 104243 (2022).

[99] M. Huber and J. I. de Vicente, *Structure of Multidimensional Entanglement in Multipartite Systems*, Phys. Rev. Lett. **110**, 030501 (2013).

[100] S. Signorini and L. Pavesi, *On-Chip Heralded Single Photon Sources*, AVS Quantum Sci. **2**, (2020).

[101] C. Drago and A. M. Brańczyk, *Hong–Ou–Mandel Interference: A Spectral–Temporal Analysis*, Can. J. Phys. **102**, 411 (2024).

[102] P. Kok, H. Lee, and J. P. Dowling, *Creation of Large-Photon-Number Path Entanglement Conditioned on Photodetection*, Phys. Rev. A **65**, 052104 (2002).

[103] R. J. Glauber, *The Quantum Theory of Optical Coherence*, Phys. Rev. **130**, 2529 (1963).

[104] R. Wiegner, J. von Zanthier, and G. S. Agarwal, *Quantum Interference and Non-Locality of Independent Photons from Disparate Sources*, J. Phys. B At. Mol. Opt. Phys. **44**, 055501 (2011).

[105] F. Paleari, A. Andreoni, G. Zambra, and M. Bondani, *Thermal Photon Statistics in Spontaneous Parametric Downconversion*, Opt. Express **12**, 2816 (2004).

[106] M. Schwartz, E. Schmidt, U. Rengstl, F. Hornung, S. Hepp, S. L. Portalupi, K. Llin, M. Jetter, M. Siegel, and P. Michler, *Fully On-Chip Single-Photon Hanbury-Brown*

and Twiss Experiment on a Monolithic Semiconductor–Superconductor Platform, Nano Lett. **18**, 6892 (2018).

[107] B. Silva, C. Sánchez Muñoz, D. Ballarini, A. González-Tudela, M. de Giorgi, G. Gigli, K. West, L. Pfeiffer, E. del Valle, D. Sanvitto, and F. P. Laussy, *The Colored Hanbury Brown–Twiss Effect*, Sci. Rep. **6**, 37980 (2016).

[108] M. Fox, *Quantum Optics* (Oxford University Press, n.d.).

[109] D. B. Horoshko, S. De Bièvre, G. Patera, and M. I. Kolobov, *Thermal-Difference States of Light: Quantum States of Heralded Photons*, Phys. Rev. A **100**, 053831 (2019).

[110] M. Bozzio, A. Cavaillès, E. Diamanti, A. Kent, and D. Pitalúa-García, *Multiphoton and Side-Channel Attacks in Mistrustful Quantum Cryptography*, PRX Quantum **2**, 030338 (2021).

[111] P. K. Verma, M. El Rifai, and K. W. C. Chan, *Multi-Photon Quantum Secure Communication* (Springer Singapore, Singapore, 2019).

[112] J. Capmany and C. R. Fernández-Pousa, *Quantum Model for Electro-Optical Phase Modulation*, J. Opt. Soc. Am. B **27**, A119 (2010).

[113] V. Torres-Company, D. E. Leaird, and A. M. Weiner, *Dispersion Requirements in Coherent Frequency-to-Time Mapping*, Opt. Express **19**, 24718 (2011).

[114] A. Abbas and L.-G. Wang, *Hanbury Brown and Twiss Effect in the Spatiotemporal Domain II: The Effect of Spatiotemporal Coupling*, OSA Contin. **4**, 2221 (2021).

[115] Y. Bromberg, Y. Lahini, E. Small, and Y. Silberberg, *Hanbury Brown and Twiss Interferometry with Interacting Photons*, Nat. Photonics **4**, 721 (2010).

[116] T. Jeltes, J. M. McNamara, W. Hogervorst, W. Vassen, V. Krachmalnicoff, M. Schellekens, A. Perrin, H. Chang, D. Boiron, A. Aspect, and C. I. Westbrook, *Comparison of the Hanbury Brown–Twiss Effect for Bosons and Fermions*, Nature **445**, 402 (2007).

[117] M. W. Puckett, K. Liu, N. Chauhan, Q. Zhao, N. Jin, H. Cheng, J. Wu, R. O. Behunin, P. T. Rakich, K. D. Nelson, and D. J. Blumenthal, *422 Million Intrinsic Quality Factor Planar Integrated All-Waveguide Resonator with Sub-MHz Linewidth*, Nat. Commun. **12**, 934 (2021).

[118] H.-H. Lu, J. M. Lukens, N. A. Peters, O. D. Odele, D. E. Leaird, A. M. Weiner, and P. Lougovski, *Electro-Optic Frequency Beam Splitters and Tritters for High-Fidelity Photonic Quantum Information Processing*, Phys. Rev. Lett. **120**, 030502 (2018).

[119] A. Xu, L. Duan, L. Wang, and Y. Zhang, *Characterization of Two-Photon Interference between a Weak Coherent State and a Heralded Single Photon State*, Opt. Express **31**, 5662 (2023).

[120] X.-H. Zhan, Z.-Q. Zhong, S. Wang, Z.-Q. Yin, W. Chen, D.-Y. He, G.-C. Guo, and Z.-F. Han, *Measurement-Device-Independent Quantum Key Distribution with Practical Spontaneous Parametric Down-Conversion Sources*, Phys. Rev. Appl. **20**, 034069 (2023).

[121] A. Christ and C. Silberhorn, *Limits on the Deterministic Creation of Pure Single-Photon States Using Parametric down-Conversion*, Phys. Rev. A **85**, 023829 (2012).

[122] Q. Wang, X.-Y. Zhou, and G.-C. Guo, *Realizing the Measure-Device-Independent Quantum-Key-Distribution with Passive Heralded-Single Photon Sources*, Sci. Rep. **6**, 35394 (2016).

[123] A. Mizutani, K. Tamaki, R. Ikuta, T. Yamamoto, and N. Imoto, *Measurement-Device-Independent Quantum Key Distribution for Scarani-Acin-Ribordy-Gisin 04 Protocol*, Sci. Rep. **4**, 5236 (2014).

[124] C. Wang, F.-X. Wang, H. Chen, S. Wang, W. Chen, Z.-Q. Yin, D.-Y. He, G.-C. Guo, and Z.-F. Han, *Realistic Device Imperfections Affect the Performance of Hong-Ou-Mandel Interference With Weak Coherent States*, J. Light. Technol. **35**, 4996 (2017).

[125] X. Li, L. Yang, L. Cui, Z. Y. Ou, and D. Yu, *Observation of Quantum Interference between a Single-Photon State and a Thermal State Generated in Optical Fibers*, Opt. Express **16**, 12505 (2008).

[126] H.-L. Yin, Y. Fu, Y. Mao, and Z.-B. Chen, *Security of Quantum Key Distribution with Multiphoton Components*, Sci. Rep. **6**, 29482 (2016).

[127] J. Liu, Y. Zhou, W. Wang, R. Liu, K. He, F. Li, and Z. Xu, *Spatial Second-Order Interference of Pseudothermal Light in a Hong-Ou-Mandel Interferometer*, Opt.

Express **21**, 19209 (2013).

[128] P. M. Alsing, R. J. Birrittella, C. C. Gerry, J. Mimih, and P. L. Knight, *Extending the Hong-Ou-Mandel Effect: The Power of Nonclassicality*, Phys. Rev. A **105**, 013712 (2022).

[129] G. S. Agarwal, *Quantum Optics* (Cambridge University Press, 2012).

[130] S. M. Barnett, G. Ferenczi, C. R. Gilson, and F. C. Speirits, *Statistics of Photon-Subtracted and Photon-Added States*, Phys. Rev. A **98**, 013809 (2018).

[131] Z. Y. Ou, J.-K. Rhee, and L. J. Wang, *Photon Bunching and Multiphoton Interference in Parametric Down-Conversion*, Phys. Rev. A **60**, 593 (1999).

[132] R. H. Hadfield, *Single-Photon Detectors for Optical Quantum Information Applications*, Nat. Photonics **3**, 696 (2009).

[133] S. Mishra, A. Biswas, S. Patil, P. Chandravanshi, V. Mongia, T. Sharma, A. Rani, S. Prabhakar, S. Ramachandran, and R. P. Singh, *BBM92 Quantum Key Distribution over a Free Space Dusty Channel of 200 Meters*, J. Opt. **24**, 074002 (2022).

[134] P. W. Shor and J. Preskill, *Simple Proof of Security of the BB84 Quantum Key Distribution Protocol*, Phys. Rev. Lett. **85**, 441 (2000).

[135] Z.-Q. Zhong, S. Wang, X.-H. Zhan, Z.-Q. Yin, W. Chen, G.-C. Guo, and Z.-F. Han, *Realistic and General Model for Quantum Key Distribution with Entangled-Photon Sources*, Phys. Rev. A **106**, 052606 (2022).

[136] X. Ma, C.-H. F. Fung, and H.-K. Lo, *Quantum Key Distribution with Entangled Photon Sources*, Phys. Rev. A **76**, 012307 (2007).

[137] M. Tomamichel, C. C. W. Lim, N. Gisin, and R. Renner, *Tight Finite-Key Analysis for Quantum Cryptography*, Nat. Commun. **3**, 634 (2012).

[138] D. Bunandar, L. C. G. Govia, H. Krovi, and D. Englund, *Numerical Finite-Key Analysis of Quantum Key Distribution*, Npj Quantum Inf. **6**, 104 (2020).

[139] J. Yin, Y.-H. Li, S.-K. Liao, M. Yang, Y. Cao, L. Zhang, J.-G. Ren, W.-Q. Cai, W.-Y. Liu, S.-L. Li, R. Shu, Y.-M. Huang, L. Deng, L. Li, Q. Zhang, N.-L. Liu, Y.-A. Chen, C.-Y. Lu, X.-B. Wang, F. Xu, J.-Y. Wang, C.-Z. Peng, A. K. Ekert, and J.-W. Pan, *Entanglement-Based Secure Quantum Cryptography over 1,120*

Kilometres, Nature **582**, 501 (2020).

[140] T. Scheidl, R. Ursin, A. Fedrizzi, S. Ramelow, X.-S. Ma, T. Herbst, R. Prevedel, L. Ratschbacher, J. Kofler, T. Jennewein, and A. Zeilinger, *Feasibility of 300 Km Quantum Key Distribution with Entangled States*, New J. Phys. **11**, 085002 (2009).

[141] X. Liu, J. Liu, R. Xue, H. Wang, H. Li, X. Feng, F. Liu, K. Cui, Z. Wang, L. You, Y. Huang, and W. Zhang, *40-User Fully Connected Entanglement-Based Quantum Key Distribution Network without Trusted Node*, PhotoniX **3**, 2 (2022).

[142] M. Alshowkan, B. P. Williams, P. G. Evans, N. S. V. Rao, E. M. Simmerman, H.-H. Lu, N. B. Lingaraju, A. M. Weiner, C. E. Marvinney, Y.-Y. Pai, B. J. Lawrie, N. A. Peters, and J. M. Lukens, *Reconfigurable Quantum Local Area Network Over Deployed Fiber*, PRX Quantum **2**, 040304 (2021).

[143] S. K. Joshi, D. Aktas, S. Wengerowsky, M. Lončarić, S. P. Neumann, B. Liu, T. Scheidl, G. C. Lorenzo, Ž. Samec, L. Kling, A. Qiu, M. Razavi, M. Stipčević, J. G. Rarity, and R. Ursin, *A Trusted Node–Free Eight-User Metropolitan Quantum Communication Network*, Sci. Adv. **6**, (2020).

[144] L. Cirigliano, V. Brosco, C. Castellano, C. Conti, and L. Pilozzi, *Optimal Quantum Key Distribution Networks: Capacitance versus Security*, Npj Quantum Inf. **10**, 44 (2024).

[145] J. C. Garcia-Escartin and P. Chamorro-Posada, *Swap Test and Hong-Ou-Mandel Effect Are Equivalent*, Phys. Rev. A **87**, 052330 (2013).

Publications

Research Output from Doctorate Thesis in peer-reviewed Journals

1. Khodadad Kashi, A., Kues, M., Frequency-bin-encoded Entanglement-based Quantum Key Distribution in a Reconfigurable Frequency-multiplexed Network. Light Sci Appl **14**, 49 (2025)

2. A. Khodadad Kashi, L. Caspani, and M. Kues, Spectral Hong-Ou-Mandel Effect between a Heralded Single-Photon State and a Thermal Field: Multiphoton Contamination and the Nonclassicality Threshold, Phys. Rev. Lett. **131**, 233601 (2023)

3. A. Khodadad Kashi, L. Sader, R. Haldar, B. Wetzel, and M. Kues, Frequency-to-Time Mapping Technique for Direct Spectral Characterization of Biphoton States from Pulsed Spontaneous Parametric Processes, Front. Photonics **3**, (2022)

4. A. Khodadad Kashi and M. Kues, Spectral Hong–Ou–Mandel Interference between Independently Generated Single Photons for Scalable Frequency-Domain Quantum Processing, Laser Photon. Rev. **15**, (2021)

Other Journal Contributions

5. H. Mahmudlu, R. Johanning, A. van Rees, **A. Khodadad Kashi**, J. P. Epping, R. Haldar, K.-J. Boller, and M. Kues, Fully On-Chip Photonic Turnkey Quantum Source for Entangled Qubit/Qudit State Generation, Nat. Photonics **17**, 518 (2023)

6. T. Godin, L. Sader, **A. Khodadad Kashi**, P.-H. Hanzard, A. Hideur, D. J. Moss, R. Morandotti, G. Genty, J. M. Dudley, A. Pasquazi, M. Kues, and B. Wetzel, Recent Advances on Time-Stretch Dispersive Fourier Transform and Its Applications, Adv. Phys. X **7**, (2022)

7. H. Arab, S. MohammadNejad, **A. KhodadadKashi**, and S. Ahadzadeh, Recent Advances in Nanowire Quantum Dot (NWQD) Single-Photon Emitters, Quantum Inf. Process. **19**, 44 (2020)

8. S. Mohammad Nejad and **A. Khodadad Kashi**, Realization of Quantum SWAP Gate Using Photonic Integrated Passive and Electro-Optically Active Components, Fiber Integr. Opt. **38**, 117 (2019)

9. S. Mohammad Nejad, **A. Khodadad Kashi**, and H. Arab, Single- and Two-Qubit Universal Quantum Gates in Photonic Ti:LiNbO3 Circuits, Optik (Stuttg). **182**, 907 (2019)

10. S. Mohammad Nejad and **A. KhodadadKashi**, CNOT-Based Quantum Swapping of Polarization and Modal Encoded Qubits in Photonic Ti:LiNbO3 Channel Waveguides, Opt. Quantum Electron. **51**, 301 (2019)

Conference Contributions

1. A. Khodadad Kashi, L. Caspani, and M. Kues, *Hong-Ou-Mandel Effect between a Thermal Field and a Heralded Single-photon State: Improved visibility by Multiphoton Components*, in Conference on Lasers and Electro-Optics/Europe (CLEO/Europe 2023) and European Quantum Electronics Conference (EQEC 2023), Technical Digest Series (Optica Publishing Group, 2023), paper ea_p_22.

2. A. Khodadad Kashi, L. Caspani, and M. Kues, Multi-Photon-Contributed Enhanced Visibility of Spectral Two-Photon Quantum Interference between Thermal-Gradient States of Light, in Quantum Computing, Communication, and Simulation III, edited by P. R. Hemmer and A. L. Migdall (SPIE, 2023), p. 79.

3. A. Khodadad Kashi and M. Kues, Spectral Two-Photon Quantum Interference via Electro-Optic Modulation Between Light States Of Different Photon Statistics, EPJ Web Conf. **267**, 02042 (2022).

4. A. Khodadad Kashi and M. Kues, Scalability of Photonic Frequency Domain Processing Revealed via Spectral Hong-Ou-Mandel Effect Between Independent Single Photons, in Quantum 2.0 Conference and Exhibition, Technical Digest Series (Optica Publishing Group, 2022), paper QTu3B.7.

5. A. Khodadad Kashi, B. Wetzel, and M. Kues, *Spectral Characterization of Parametric* Biphoton States Enabled by Frequency-to-Time Mapping Technique, in 2022 Conference on Lasers and Electro-Optics Pacific Rim (CLEO-PR) (IEEE, 2022), pp. 1–2.

6. A. Khodadad Kashi, L. Caspani, and M. Kues, Improved Visibility of Spectral Two-Photon Quantum Interference Introduced by Multiphoton Components, in Frontiers in Optics + Laser Science 2022 (FIO, LS) (Optica Publishing Group, Washington, D.C., 2022), p. FM3B.4.

7. A. Khodadad Kashi and M. Kues, Photon-Number-Dependent Visibility in Two-Photon Spectral Quantum Interference Between a Thermal Field and Heralded-State, in 2022 Conference on Lasers and Electro-Optics Pacific Rim (CLEO-PR) (IEEE, 2022), pp. 1–2.

8. A. Khodadad Kashi, B. Wetzel, and M. Kues, Frequency-to-Time Mapping-Assisted Spectral Characterization of Parametric Biphoton States, in Conference on Lasers and Electro-Optics (Optica Publishing Group, Washington, D.C., 2022), p. FW1A.5.

9. R. Haldar, R. Johanning, **A. Khodadad Kashi**, H. Mahmudlu, P. Rübeling, S. Bose, T. Bækkegaard, A. van Rees, J. P. Epping, N. T. Zinner, K.-J. Boller, and M. Kues, *Controlled Generation of Photonic Non-Classical Frequency Combs for Quantum Information Processing*, in *Quantum Computing, Communication, and Simulation IV*, edited by P. R. Hemmer and A. L. Migdall (SPIE, 2024), p. 58.

10. R. Haldar, H. Mahmudlu, R. Johanning, A. van Rees, **A. K. Kashi**, J. P. Epping, K.-J. Boller, and M. Kues, Laser-Integrated Entirely On-Chip Turnkey Quantum Photonic Sources, in 2024 16th International Conference on COMmunication Systems & NETworkS (COMSNETS) (IEEE, 2024), pp. 1024–1027.

11. L. Sader, Y. Boussafa, V.-T. Hoang, S. Bose, **A. Khodadad Kashi**, R. Haldar, B. P. Chaves, A. Bougaud, M. Fabert, V. Kermène, A. Tonello, V. Couderc, M. Kues, and B. Wetzel, *Smart Photonics: Characterization and Control of Modulation Instability Processes in Nonlinear Fiber Optics*, in *Nonlinear Optics and Its Applications 2024*, edited by A. C. Peacock, G. Tissoni, J. M. Dudley, and B. Stiller (SPIE, 2024), p. 4.

12. Hatam Mahmudlu, Raktim Haldar, Robert Johanning, **Anahita Khodadad Kashi**, Albert van Rees, Jörn P. Epping, Klaus-J. Boller, Michael Kues, *Fully on-chip photonic turnkey quantum light source of two- and high-dimensional entangled photons*, Proc. SPIE PC12424, Integrated Optics: Devices, Materials, and Technologies XXVII, PC124240E (17 March 2023).

13. Haldar, R., Mahmudlu, H., Johanning, R., **Khodadad Kashi, A.**, van Rees, A., Epping, J. P., Boller, K.-J., & Kues, M. (2023). *Fully On-chip Laser-integrated Entangled Photon Pair Source*. Paper presented at 24th European Conference on Integrated Optics, ECIO 2023, Enschede, Netherlands.

14. L. Sader, S. Bose, **A. Khodadad Kashi**, Y. Boussafa, R. Dauliat, P. Roy, M. Fabert, A. Tonello, V. Couderc, M. Kues, and B. Wetzel, *Ultrasensitive Dispersive Fourier Transform Characterization of Nonlinear Instabilities*, in Conference on Lasers and

Electro-Optics/Europe (CLEO/Europe 2023) and European Quantum Electronics Conference (EQEC 2023), Technical Digest Series (Optica Publishing Group, 2023), paper cd_9_1.

15. H. Mahmudlu, R. Haldar, R. Johanning, **A. Khodadad Kashi**, A. van Rees, J. P. Epping, K.-J. Boller, and M. Kues, Fully On-Chip Laser-Integrated Quantum Source of Entangled Photon States, in 2023 Conference on Lasers and Electro-Optics Europe & European Quantum Electronics Conference (CLEO/Europe-EQEC) (IEEE, 2023), pp. 1–1.

16. L. Sader, S. Bose, **A. Khodadad Kashi**, Y. Boussafa, R. Haldar, R. Dauliat, P. Roy, M. Fabert, A. Tonello, V. Couderc, M. Kues, and B. Wetzel, *Single-Photon Level Dispersive Fourier Transform: Ultrasensitive Characterization of Noise-Driven Nonlinear Dynamics*, ACS Photonics **10**, 3915 (2023).

17. R. Haldar, R. Johanning, P. Rübeling, **A. K. Kashi**, T. Bækkegaard, S. Bose, N. T. Zinner, and M. Kues, Unidirectional Bosonic Quantum Walk and Entanglement Redistribution from High-Dimensional Quantum States with Tunable Entropies, in Quantum Computing, Communication, and Simulation III, edited by P. R. Hemmer and A. L. Migdall (SPIE, 2023), p. 30.

18. L. Sader, S. Bose, **A. Khodadad Kashi**, Y. Boussafa, R. Dauliat, P. Roy, M. Fabert, A. Tonello, V. Couderc, M. Kues, and B. Wetzel, Ultrasensitive Dispersive Fourier Transform Technique for Nonlinear Instability Characterization, in Frontiers in Optics + Laser Science 2022 (FIO, LS), Technical Digest Series (Optica Publishing Group, 2022), paper FTu1B.3.

19. R. Haldar, H. Mahmudlu, R. Johanning, **A. Khodadad Kashi**, A. van Rees, J. Epping, K. Boller, and M. Kues, Fully On-chip Electrically-pumped Laser-integrated Two and High-dimensional Entangled Photon Pair Source, in Frontiers in Optics + Laser Science 2022 (FIO, LS), Technical Digest Series (Optica Publishing Group, 2022), paper FTh3E.6.

20. L. Sader, S. Bose, **A. K. Kashi**, R. Dauliat, P. Roy, M. Fabert, A. Tonello, V. Couderc, M. Kues, and B. Wetzel, "Ultra-sensitive characterization of nonlinear instabilities via single photon dispersive Fourier-transform," in Conference on Lasers and Electro-Optics, Technical Digest Series (Optica Publishing Group, 2022), paper JW3B.166.

21. R. Haldar, P. Rübeling, **A. Khodadad Kashi**, and M. Kues, High-Dimensional Bi-Photon Quantum Frequency Combs with Tunable State Entropies, in OSA Advanced Photonics Congress 2021 (Optica Publishing Group, Washington, D.C., 2021), p. ITh2A.5.

Patents

1.PCT – P6230FP00, Anahita Khodadad Kashi, Michael Kues, Thomas Bækkegaard, Nikolaj Zinner, Quantum Generative Adversarial Networks with Quantum Frequency Comb Photonics, 2019 – 2020

Curriculum Vitae

2019 – present	Research Assistant at Institute of Photonics (IOP), Leibniz University, Hannover (Supervisor: Prof. Dr. Michael Kues)
2015 – 2019	M.Sc. in Electrical Engineering (Micro & Nano-electronics), Iran University of Science & Technology (IUST), Supervised by Prof. Dr. Shahram Mohammad Nejad

M.Sc. Dissertation Title: Design and simulation of photonic quantum gates using Lithium Niobate waveguides, based on separation and entanglement factors of mode, frequency, and polarization.

M.Sc. Dissertation Abstract: The theoretical photonic circuit design of CNOT and SWAP quantum gates using Titanium-diffused LiNbO3 channel waveguides is reported. The mentioned quantum gates play an integral role in quantum computing, networkability of quantum circuits, as well as for the implementation of quantum algorithms. Photonic integrated circuits provide a suitable platform for scalable and stable realization of quantum gates and by far, the least probability of decoherence and entanglement collapse has been reported in on-chip approaches. In this research, we take advantage of the diversity of applications that LiNbO3 offers, and a few on-chip monolithically integrated passive and electro-optically active components, together contributing to the realization of quantum CNOT and SWAP gates. In our approach, all the steps including the generation of entangled photon pairs, transmission and manipulation of the quantum states have been accommodated on-chip, and the fully-integrated feature of our approach is considered as a figure of merit by comparison to previously reported schemes.

Main modules: Quantum electronics, Nano electronics, Nano devices and integration, Optical Electronics, Theory and Manufacturing Technology of Semiconductor Devices

2010 – 2015	B.Sc. in Electrical Engineering, Shahid Beheshti University
	Dissertation Project: Design and implementation of a temperature sensing module using ATMega-32 Microcontroller